FAR-FIELD AND NEAR-FIELD OPTICAL PROPERTIES OF PLANAR PLASMONIC OLIGOMERS

MOHSEN RAHMANI

NATIONAL UNIVERSITY OF SINGAPORE

2012

FAR-FIELD AND NEAR-FIELD OPTICAL PROPERTIES OF PLANAR PLASMONIC OLIGOMERS

MOHSEN RAHMANI

A THESIS SUBMITTED FOR THE DEGREE OF
DOCTOR OF PHILOSOPHY
DEPARTMENT OF ELECTRICAL AND COMPUTER ENGINEERING
NATIONAL UNIVERSITY OF SINGAPORE
2012

This PhD thesis is dedicated to our newborn “Sofia” who has brought happiness to our life.

DECLARATION

I hereby declare that this thesis is my original work and it has been written by me in its entirety. I have duly acknowledged all the sources of information which have been used in the thesis. This thesis has also not been submitted for any degree in any university previously.

(Mohsen Rahmani)

Acknowledgements

I would like to express my heartiest appreciation and gratitude to my supervisors, Prof. Thomas Yun Fook Liew and Prof. Minghui Hong for their invaluable guidance and great support throughout my PhD course. I would like to thank them for giving me the numerous opportunities to learn and grow as a PhD student. Particularly, I am truly grateful to Prof. Hong for his kind assistance towards the difficulties that I have faced in my personal life as well as his infinite passion in research work, which inspires me to work hard. Meanwhile, much appreciation goes to Prof. Boris Lukiyanchuk for his helps, advices and useful discussions in my researches.

It is my pleasure to appreciate all my lab members, Caihong, Zhiqiang, Tang Min, Hong Hai, Chin Seong, Doris, Xu Le, Nguyen Thi Van Thanh, Liu Yan, Li Xiong, Han Ningren, Ng Binghao and specially my dear friend Zaichun as well as my friends in DSI and IMRE, Amir (T), Mojtaba, Taiebeh, Behruz, Mehdi, Mojtaba (R), Sepehr, Sepideh, Hamed (A), Mahnaz, Amir (M), Hamed (K) and specially Meisam. I deeply appreciate the time shared with you and I wish you the best luck in your careers. I also thank Prof. Stefan A. Maier, Prof. Harald Giessen, Prof. Peter Nordlander, Prof. Andrey Miroshnichenko, Dr. Dang Yuan Lei and Dr. Vincenozo Giannini for useful discussions and comments. I would like to express gratitude for the financial support from the A*STAR Singapore International Graduate Award (SINGA) program and DSI for their numerous support.

Last but the most importantly, I would like to give my great thanks to my parents and my lovely wife Yana. Thank you for your love all the while which gives me the strength to carry on.

Table of Contents

Acknowledgments i
Table of Contents ii
Abstract iv
List of Figures vi
List of Tables xi
List of Symbols xii
List of Publications xiii

CHAPTER 1. Introduction **1**
1.1. Background and literature review 4
1.1.1. Fano resonance definition 6
1.1.2. Fano resonance in plasmonic systems 14
1.1.3. Fano resonance in plasmonic oligomers 18
1.2. Research motivation 21
1.3. Organization of thesis 23

CHAPTER 2. Experiment **26**
2.1. Fabrication 27
2.1.1. Substrate cleaning 28
2.1.2. Metallic film deposition 28
2.1.3. Resist coating 29
2.1.4. Exposure and develop 30
2.1.5. Pattern transfer 33
2.2. Characterization 35
2.2.1. Scanning electron microscopy 35
2.2.2. Atomic force microscopy 37
2.2.3. Micro UV-Visible spectroscopy 38
2.2.4. Fourier transform infra-red spectroscopy 39
2.3. Simulation 40
2.4. Summary 40

CHAPTER 3. Far-field optical properties of oligomers: Generation of pronounced Fano resonance **42**
3.1. Destructive interference among dipole modes 44
3.2. Mass-spring mechanical model 49
3.3. Influence of components` geometry on Fano Resonance 51
3.4. Subgroups decomposition 53
3.5. Geometrical hybridization 56
3.6. Monolith oligomeric structures 58
3.6.1 90° Rotor-shaped structure 59
3.6.2 Hybrid pentamers with central rotor-shaped element 60
3.7. Symmetry breaking 62

3.8. Summary 68

CHAPTER 4. Far-field optical properties of quadrumers **70**
4.1. Analogy to molecular configurations 71
4.2. Mass-spring analogy 78
4.3. Geometrical influence 80
4.4. Summary 88

CHAPTER 5. Near-field optical properties of oligomers: Energy localization **90**
5.1. Near-field localization 92
5.2. Influence of geometry on the near-field energy 94
5.3. Influence of defects on the near-field energy 98
5.4. Near-field energy enhancement by rotor-shaped structures 99
5.5. Summary 102

CHAPTER 6. Conclusions and future work **103**
6.1. Conclusions 104
6.2. Future works 105

References and links **107**

Abstract

Recently, a large number of experimental and theoretical works has revealed a variety of plasmonics nanostructures with the capabilities of Fano Resonance (FR) generation. FR exhibition in most nanostructures needs an excited high-order mode with a very narrow linewidth and its interference with a dipole mode which has a broad spectrum response. The excitation of such high-order modes is typically established by challenging complex structures or geometrical symmetry breaking at certain polarization direction of incident light. Newly introduced planar plasmonic oligomers, consisting of packed metallic nanoelements, tackle these challenges. Such structures can exhibit FR independently of polarization direction based on the anti-parallel dipole modes rather than an overlap between dipole and high-order modes. Nonamers and heptamers are well studied oligomers exhibiting FR as the result of anti-parallel hybridization among the dipole mode arising from the central nanoparticle and net dipole mode arising from the ring-like satellite elements with opposite phase characteristics.

In this thesis a way to increase the value of ratio among anti-parallel dipole modes is investigated by reduction of the number of surrounding satellite elements to enhance the contrast of FR. Pentamers and quadrumers are novel oligomers which can realize this goal. Meanwhile, it is shown that hybridization of plasmons arising from individual elements of such oligomers can be modeled in good agreement with mechanical mass-spring analogues. It provides better understanding of interaction among plasmons arising from individual elements. Furthermore, detailed study on the spectral shape of resonances guided us to propose a recipe to flexibly control the Fano profile signature. The effects of elements` size, gap among them and symmetry breaking on FR in such structures are also studied in details.

Subsequently, it is shown that while the far-field optical properties of oligomers are polarization independent, the near-field energy can be flexibly re-distributed inside the arbitrary inter-particle gaps by changing the polarization orientation. This tuneability is obtained at a normal incidence of a single light source rather than by co-illumination with two light sources at different incident angles or with respective phase shifts. Meanwhile, it is shown that as compared to the regular oligomers consisting of circular elements, hybrid oligomers with rotor-shaped central elements are better candidates to enhance the exhibited near-field energy among the gaps significantly. Such structures allow achieving more precise localization of the near-field energy.

One should note here that all results provided in this thesis are fundamental research works to generate and optimize FR in plasmonic oligomers as well as localizations, enhancement and tuning of near-field energy in such structures. These findings suggest high potential applications in optical switching, slow-lighting, nonlinear spectroscopy and bio-chemical sensing.

List of Figures

Figure 1. 1 Illustration of two coupled interacting oscillators.

Figure 1. 2 (a) The resonant behavior of the amplitude of the first oscillator in the coupled system. (b) The phase behavior of the first oscillator amplitude around the resonances.

Figure 1. 3 (a) The amplitude of the second oscillator as a function of the frequency. (b) The phase behavior of the second oscillator.

Figure 1. 4 Extinction spectra of a gold monomer, a gold hexamer, and gold hepatmers with different inter-particle gap separations.

Figure 2. 1 Illustration of fabrication steps.

Figure 2. 2 Schematic drawing of an electron beam evaporator.

Figure 2. 3 Schematic drawing of an EBL system.

Figure 2. 4 Schematic drawing of an ion beam process system.

Figure 2. 5 Schematic drawing of a scanning electron microscopy system.

Figure 2. 6 (a) Simplified schematic of a AFM system and (b) Diagram of relationship between force and tip distance from the surface for different AFM modes.

Figure 3. 1 (a) Sketch of pentamer arrays. SEM images of periodic array patterns of (b) monomers, (c) ring-like quadrumers and (d) pentamers. Scale bar is 100 nm.

Figure 3. 2 (a) Simulated and (b) experimental transmission spectra of monomers, quadrumers and pentamers at x-polarized normal incidence.

Figure 3. 3 Calculated charge distributions for the ring-like quadrumer (a) before the resonance at 600 nm and (b) after the resonance 700 nm and (c) Charge distribution of the pentamers structure at a wavelength of 665 nm.

Figure 3. 4 (a) Five coupled interacting oscillators representing the pentamer optical responses, (b) simplified three coupled oscillators and (c) simulated plasmons absorption spectra by FDTD (dot line) and calculated power absorption in the oscillator model (solid line).

Figure 3. 5 Simulated transmission spectra of 6 various types of pentamers at x-polarized normal incidence.

Figure 3. 6 (a) SEM image of a periodic array of pentamers consisting of Au disks. The scale bar is 100 nm. (b) Simulated extinction spectra of an individual pentamer (black curve) and the two subgroups (blue and red curves). (c) Sketch of decomposing a pentamer into Groups I and II. (d) Electric field intensity distribution in the pentamer at peaks 1 and 2 and in the two subgroups at their respective scattering peaks 3 and 4. (e) Measured extinction spectrum of the pentamer array at normal incidence. The inset shows a 3D AFM image of the pentamers and the incident polarization.

Figure 3. 7 Tuning of resonance linewidth and spectral contrast of plasmon resonances in different pentamers. (a) SEM images of hybrid pentamers consisting of differently-shaped elements. The scale bar in each image is 100 nm. (b) Simulated extinction spectra for the pentamers (black curve) and their two subgroups (blue and red curves). (c) Measured extinction spectra for the same pentamers at normal incidence, along with 3D AFM images of the nanostructures.

Figure 3. 8 (a) SEM images of 90° symmetric rotor-shaped nanostructures, (b) simulated and (c) experimental extinction spectra of the corresponding structures in (a) at indicated polarization excitation with respect to x-axis. Scale bar is 100 nm.

Figure 3. 9 (a) SEM images of designed hybrid pentamers and quadrumers, (b) simulated and (c) experimental extinction spectra of the corresponding structures in (a) at indicated polarization excitation with respect to x-axis. Scale bar is 100 nm.

Figure 3. 10 SEM images of periodic array nanopatterns of (a) the Type I symmetric pentamer, the (b) Type II and (c) Type III asymmetric pentamers. The offset of the central disk for the Type II and Type III asymmetric pentamers are 6 nm and 12 nm, respectively leading to a corresponding gap of 9 nm and 3 nm gaps. (d), (e) and (f) simulated and experimental reflection spectra of the corresponding pentamers in (a), (b) and (c). Diameter of each disk is 125 nm.

Figure 3. 11 Calculated charge distribution of the Type III pentamer at a wavelength of (a) 650 nm and (b) 580 nm. (c) Calculated forward and backward far-field scattering for the Type I, II and III pentamers, respectively.

Figure 3. 12 Simulated FDTD (red line) and oscillator model calculated (black line) extinction spectra for pentamer Type III.

Figure 4. 1 (a) (Upper row) Illustrations of the molecular geometries of an H atom and the trigonal planar molecule configuration. (bottom row) Their plasmonic analogues, a gold monomer and a gold quadrumer. SEM images of periodic array patterns of (b) monomers and (c) quadrumer. Scale bar is 100 nm. (d) AFM image of quadrumers.

Figure 4. 2 (a) Simulated and (b) measured reflection spectra of the monomers and quadrumers at x-polarized normal incidence. Calculated charge distribution of the quadrumer at a wavelength of (c) 640 nm and (d) 780 nm by FDTD simulation.

Figure 4. 3 (a) Three coupled interacting oscillators representing the quadrumer optical responses and corresponding calculated power absorption, and (b) simulated extinction spectra of the quadrumer at x-polarized normal incidence by FDTD.

Figure 4. 4 Simulated transmission spectra of 6 various types of pentamers at x-polarized normal incidence.

Figure 4. 5 (a) SEM image of a periodic array of quadrumers consisting of Au disks. The scale bar is 100 nm. (b) Simulated extinction spectra of an individual quadrumer (black curve) and the two subgroups (blue and red curves). (c) Sketch of decomposing a quadrumer into Groups I and II. (d) Electric field intensity distribution in the pentamer at peaks 1 and 2 and in the two subgroups at their respective scattering peaks 3 and 4. (e) Measured extinction spectrum of the pentamer array at normal incidence. The inset shows a 3D AFM image of the pentamers and the incident polarization.

Figure 4. 6 Tuning of resonance linewidth and spectral contrast of plasmon resonances in different quadrumers. (a) SEM images of hybrid quadrumers consisting of differently-shaped elements. The scale bar in each image is 100 nm. (b) Simulated extinction spectra for the pentamers (black curve) and their two subgroups (blue and red curves). (c) Measured extinction spectra for the same pentamers at normal incidence, along with 3D AFM images of the nanostructures.

Figure 4. 7 (a) SEM images of 120° symmetric rotor-shaped nanostructures, (b) simulated and (c) experimental extinction spectra of the corresponding structures in (a) at indicated polarization excitation with respect to x-axis. Scale bar is 100 nm.

Figure 4. 8 (a) SEM images of designed hybrid quadrumers, (b) simulated and (c) experimental extinction spectra of the corresponding structures in (a) at indicated polarization excitation with respect to x-axis. Scale bar is 100 nm.

Figure 5. 1 Calculated field distributions at x-polarized normal incidence at a wavelength of 880 nm and at (a) x-polarized (b) y-polarized and (c) 45-degree polarized light incidence.

Figure 5. 2 Calculated field distribution at x-polarized normal incidence at a wavelength of 780 nm at (a) 30-degree polarized, (b) 60-degree polarized and (c) non-polarized, to normal light incidence.

Figure 5. 3 (a) Linear and (b) logarithm scales of the calculated electric field distribution within the 6 various pentamers at x-polarized normal incidence and a wavelength of the second deep in the corresponding transmission spectra of Fig. 3.5.

Figure 5. 4 (a) Linear and (b) logarithm scales of the calculated electric field distribution within the 4 various quadrumers at x-polarized normal incidence and a wavelength of the second deep in the corresponding transmission spectra of Fig. 4.4.

Figure 5. 5 Calculated near-field energy distribution within the Type III pentamer at x-polarized normal incidence and a wavelength of 700 nm: (a) x-polarization, (b) y-polarization and (c) 45-degree polarization, with respect to x axis.

Figure 5. 6 Calculated field distribution at indicated polarization excitation for (a) rotor shaped structure, (b) regular pentamer and (c) hybrid pentamer at a wavelength of 1010 nm and structure II at a wavelength of 1025 nm.

Figure 5. 7 Calculated field distribution at indicated polarization excitation for (a) rotor shaped structure, (b) regular pentamer and (c) hybrid pentamer at a wavelength of 1010 nm and structure II at a wavelength of 1025 nm.

List of Tables

Table 3. 1 Dimensions of 6 various types of pentamers.

Table 4. 1 Dimensions of 4 various types of quadrumers.

List of Symbols

t	Time (s)
$x(t)$	Oscillator displacement from the equilibrium positions (m)
$\dot{x}(t)$	First derivative of x with respect to time ($\frac{m}{s}$)
$\ddot{x}(t)$	Second derivative of x with respect to time ($\frac{m}{s^2}$)
γ	Frictional parameter (energy dissipation) of oscillators (W)
ω	Frequency of the external harmonic force (eV)
Ω	Coherent coupling frequency between interconnected oscillators (eV)
φ	Phase (Radian)
θ	Phase shift (Radian)

List of Publications

Journal papers

1. **M. Rahmani**, B. Lukiyanchuk, B. Ng, A. K. G. Tavakkoli, T. Y. F. Liew, and M. H. Hong, "Generation of pronounced Fano Resonances and tuning of subwavelength spatial light distribution in plasmonic pentamers," **Optics Express** 19, 4949-4956 **(2011).**

2. **M. Rahmani**, B. Lukiyanchuk, T.T.V. Nguyen, T. Tahmasebi, Y. Lin, T. Y. F. Liew and M.H. Hong, " Influence of symmetry breaking in pentamers on Fano resonance and near-field energy localization," **Optical Materials Express** 1, 1409-1415 **(2011).**

3. **M. Rahmani**, T. Tahmasebi, Y. Lin, B. Lukiyanchuk, T. Y. F. Liew, and M. H. Hong, "Influence of plasmon destructive interferences on optical properties of gold planar quadrumers," **Nanotechnology** 22, 245204 **(2011).**

4. **M. Rahmani**, T. Tahmasebi, B. Lukiyanchuk, T. Y. F. Liew, and M.H. Hong, "Polarization-controlled spatial localization of near-field energy in planar symmetric coupled oligomers," **Applied Physics A** 107, 23-30 **(2011).**

5. **M. Rahmani**, D. Y. Lei, V. Giannini, B. Lukiyanchuk, M. Ranjbar, T. Y. F. Liew, M. H. Hong, and S. A. Maier, "Subgroup Decomposition of Plasmonic Resonances in Hybrid Oligomers: Modeling the Resonance Lineshape," **Nano Letters** 12, 2101-2106 **(2012).**

6. **M. Rahmani**, B. Lukiyanchuk, and M.H. Hong, "Fano resonance in novel plasmonic nanostructures," **Laser & Photonics Reviews**, DOI: 10.1002/lpor.201200021 **(2012).**

7. Z. Chen, **M. Rahmani**, G. Yandong, C. T. Chong and M. H. Hong, "Realization of Variable Three Dimensional Terahertz Metamaterial Tubes for Passive Resonance Tunability," **Advanced Materials** 24, OP143-OP147 **(2012).**

8. H. Aouani, M. Navarro-Cia, **M. Rahmani**, T. P. H. Sidiropoulos, M. Hong, R. F. Oulton, and Stefan A. Maier, "Multiresonant broadband optical antennas as efficient tunable nanosources of second harmonic light," **Nano Letters** 12, 4997–5002 **(2012).**

9. J. Yang, **M. Rahmani**, J. H. Teng, and M.H. Hong, "Magnetic-electric interference in metal-dielectric-metal oligomers: generation of magneto-electric Fano Resonance," **Optical Materials Express** 2, 1407-1415 **(2012).**

10. H. Aouani, H. Sipova, **M. Rahmani**, M. Navarro-Cia, K. Hegnerova, J. Homola, M. Hong, and Stefan A. Maier, "Ultra-Sensitive Broadband Probing of Molecular Vibrational Modes with Multifrequency Optical Antennas", **ACS Nano**, Published online, **DOI:** 10.1021/nn304860t **(2012).**

Conference papers

1. **M. Rahmani,** T. Tahmasebi, B. Lukiyanchuk, T. Y. F. Liew, and M.H. Hong, "Polarization-controlled spatial localization of near-field energy in planar symmetric coupled oligomers", **Poster Presentation, ICMAT 2011-Singapore, Singapore**, 26 June-1 July.

2. **M. Rahmani**, B. Lukiyanchuk, T. Y. F. Liew, and M.H. Hong, "Design and tuning of Fano-shape resonances in planar symmetric coupled oligomers", **Invited Talk, PIERS 2012-Kuala Lumpur, Malaysia**, 26-30 March**.**

3. **M. Rahmani**, B. Lukiyanchuk, T. Y. F. Liew, and M.H. Hong, "Planar isotropic rotor-shaped nanostructures: an alternative to develop oligomers", **Oral Talk, CLEO 2012- San Jose, USA**, 6-11 May.

4. **M. Rahmani**, B. Lukiyanchuk, and M. H. Hong, "Hybrid oligomers: design and tuning the Fano resonance by decoding the contributing bright modes", **Invited talk** (/session chair,) **IEEE-INEC 2013-Singapore,** 2-4 January.

Chapter 1.

Introduction

Since Gilileo Galilei recognized the resonance effect in his study of musical strings in 1602, many types of resonances, such as mechanical, acoustic and electromagnetic, have been explored as the universal characteristics of various classical and quantum systems. The spectral dependence of these resonances is generally described by the Lorentzian formula with dynamical variables arising from a simple linear differential equation [1, 2]. For many years, the Lorentzian formula was regarded as the fundamental lineshape of a resonance. This spectral feature is frequently modified by the presence of several independent resonances of different physical origins, where the lineshape is simply the sum of the intensities of the individual resonances which contribute to it.

In 1961, Ugo Fano theoretically described distinctly asymmetric shape in the absorption resonance of noble gases, which was experimentally observed in 1935 by him [3]. This new type of resonance, which was explained via quantum mechanical system, now bears the name of Fano. The microscopic origin of the Fano Resonance (FR) arises from the constructive and destructive interferences of a narrow discrete resonance with a broad spectral line or continuum [1, 3-7]. Until the end of 20th century, this phenomenon has been studied basically for quantum systems. However the basic effect of interference in classical system of coupling oscillators is well known for a long time and even has been used in mechanical systems for dynamic damping [8]. Recently Fano interferences have been applied successfully to explain a large number of phenomena in various systems. These phenomena include the quantum transport in quantum dots, wires and tunnel junctions [9-11], energy-dependent line profile of absorption in molecular systems [12, 13], photon-exciton interactions in bilayer graphene nanostructures [14, 15] and asymmetric distribution of the density of states in Anderson impurity systems [16] as well as several optical systems,

such as strong coupling between Mie and Bragg scattering in photonic crystals [17, 18], plasmonic systems [19-31] and terahertz metamaterials [32-44].

Among all these systems, the field of plasmonics has become one of the most active platforms in FR generation and applications due to its ease for generating the coherent effects [19-31], in last few years. It is well known that metallic nanostructures can sustain surface plasmons which are the coherent oscillations of the conduction electrons at the interface between metal and dielectric materials [21]. Since the relevant interaction parameters can be tuned by changing the geometry and composition of nanostructures, plasmonic systems have proven to be an ideal choice to generate FRs with sharp dispersion. In such systems, FR occurs via the spectral overlap of broad superradiant and sharp subradiant resonance modes, which are typically characteristics of dipolar and high-order modes, respectively. Comprehensive descriptions of fundamental Fano theory and its progress through various designs of plasmonic nanostructures can be found in recent reviews [1-7].

Plasmonic planar oligomers as newly introduced plasmonic nanostructures consisting of packed aggregated nanoscale metallic components, have also been investigated to exhibit FR in the visible and near infra-red spectral ranges. These structures are of significant interest due to their fundamental importance as a model system to understand the nature of electromagnetic coupling [45-63]. Hybridization of plasmons arising from finite number of individual elements of oligomers is found to excite multiple plasmon resonances with large induced electromagnetic field enhancement. Unlike most of the other plasmonic nanostructures in which a high-order mode and its overlap with a dipole mode is a requirement to FR appearance [1-7], the sharp FR in the oligomers is generated only by

dipole modes with different plasmon oscillation phases arising from various elements [45-61, 64-66]. It can address the challenges of high order modes excitation and make the oligomers unique devices for bio-sensing and other potential applications [2]. On the other hand, while far-field optical properties of oligomers are polarization independent, the near-field energy can be flexibly redistributed inside the arbitrary inter-particle gaps by changing the polarization orientation as a versatile tool. This ability may also be used for optical switching and nonlinear spectroscopy.

In this thesis, attention will be given to the optical properties of novel oligomers, such as pentamers and quadrumers [47, 48, 60-62, 66]. Subsequently, advantages of such oligomers as compared to the other oligomers with more outer elements are explained in details. Pentamers and quadrumers consist of one central element surrounded by four and three satellite elements, respectively. Geometry of such oligomers provides opportunity to obtain more pronounced FR in contrast to the other oligomers due to the modulation in the ratio of anti-parallel dipole modes arising from individual elements. Furthermore, the provided results can reveal the ability of tuning and modeling the profile of FR, which can enable high potential applications in optical sensing and modulations. Meanwhile, it will be shown that these novel oligomers provide a promising platform to generate and localize near-field energy known as hot-spots in nanoscale gaps among the components.

1.1. Background and literature review

Surface plasmon resonances (SPRs) have become one of the most interesting and actively researched areas, enabling numerous fundamental studies and applications in a variety of scientific disciplines [19-31]. A plasmon oscillation can be explained as the collective motion

of conduction band electrons in a metal, which is driven by the electric field component of light. SPRs not only give rise to the alteration of the incident radiation pattern but also strike several effects such as the subwavelength localization of electromagnetic energy, the formation of high intensity hot spots at the subwavelength gaps in nanostructures or the directional scattering of light out of the structure.

Meanwhile, coupling between neighboring nanostructures, especially when arranged in a periodic lattice, may lead to unique emerging properties and the assembly of plasmonic nanostructures [5-7]. Such phenomena find wide range of applications in ultra-sensitive detection schemes, waveguides and lenses. It also leads to advancement in the fields of light harvesting and metamaterials [5-7]. SPRs can couple to the electromagnetic fields emitted by molecules, atoms, or quantum dots placed in the vicinity of the nanostructures, leading in turn to a strong modification of the radiative and nonradiative properties. These applications typically are based on the precise monitoring of changes in energy, amplitude and figure of merit of resonances. But determination of such factors appears to suffer from broadband plasmons resonance characteristics. It brings the practical applications to the bottleneck.

Recently, the ease to generate coherent effects in plasmonic systems has attracted increasing interest in applying the concept of FR in such systems [1-7]. Recent advancements in nanofabrication and nano-optical characterization, as well as improvements in full-field computational electromagnetics, have also provided rich opportunities to achieve this goal, by providing robust results for practitioners to tackle assessment models of SPRs by sharper plasmonic FRs. In this section, first the general definition of FR is studied in detail. Subsequently, the realization of FRs in plasmonic system will be described and finally a method of generating FR via plasmonic oligomers will be described.

1.1.1. Fano resonance definition

It is known that the Fano interference is a universal phenomenon due to the manifestation of configuration interference which does not depend on the matter [1]. One of the best ways to explain the physical nature of Fano resonances is to study the classical resonances in the harmonic oscillator system [47, 48, 60, 67, 68]. It can have a manifestation as a coupled behavior of two effective oscillators associated with propagating and evanescent waves. For this purpose, first we briefly recall the behavior of the single mechanical oscillator in a medium under an external harmonic force [69]. It is well known that if a particle moves under a harmonic force, differential equation that describes the motion is:

$$\ddot{x}_1(t) + \gamma\ \dot{x}(t) + \omega_0{}^2 x(t) = A\cos\omega t\,, \tag{1.1}$$

where ω_0 is the frequency of the oscillator, γ is a frictional parameter, and ω is a frequency of the external harmonic force. In order to solve Eq. (1.1), the sum of the complementary x_c and the particular x_p solutions are defined. The complementary solution explains the motion of a damping oscillator:

$$x_c(t) = e^{-\gamma\ t/2}[q_1 e^{i\omega' t} + q_2 e^{-i\omega' t}]\,, \tag{1.2}$$

where $\omega' = \sqrt{\omega_0^2 - \gamma^2/4}$, and q_1 and q_2 are complex numbers.

To find a simple way of a particular solution of Eq. (1.1) is to use the complex representation. Therefore, Eq. (1.1) can be rewritten for a particular solution x_p as:

$$\ddot{x}_p + \gamma\dot{x}_p + \omega_0{}^2 x_p = \frac{1}{2}A(e^{i\omega t} + e^{-i\omega t})\,, \tag{1.3}$$

The solution can be written as $x_p = x^+ + x^-$, where x^+ and x^- are solutions for the positive and the negative frequencies, respectively. Therefore, the particular solution can be

written as $x_p(t) = 2\,\mathrm{Re}(x^+(t))$, where x^+ may be considered as a solution of the equation

$$\ddot{x}^+ + \gamma\dot{x}^+ + \omega_0{}^2 x^+ = ae^{i\omega t}, \tag{1.4}$$

while $a = A/2$. Subsequently the solution of Eq. (1.4) can be explained in a form as $x^+(t) = ce^{i\omega t}$ and the amplitude $c(\omega)$ can be written as:

$$c(\omega) = \frac{a}{\omega_0^2 - \omega^2 + i\gamma\omega}, \tag{1.5}$$

which possess the modulus $|c(\omega)|$ and the phase $\varphi(\omega) : c(\omega) = |c(\omega)|e^{-i\varphi(\omega)}$, where

$$|c(\omega)| = \frac{a}{\sqrt{(\omega_0^2 - \omega^2)^2 + \omega^2\gamma^2}}, \quad \varphi(\omega) = \tan^{-1}\left(\frac{\omega\gamma}{\omega_0^2 - \omega^2}\right). \tag{1.6}$$

In the case of steady-state effects, the complementary solution can be neglected. In this case the solution can be written as

$$x(t) \approx |c(\omega)|\cos\left[\omega t - \varphi(\omega)\right]. \tag{1.7}$$

One can be assumed that the inequality $\gamma << \omega_0$ holds for the oscillator parameters. In this case a resonance in $|c(\omega)|$ occurs as the frequency ω of the external harmonic force approaches to the natural frequency ω_0 of the oscillator. At this resonance the amplitude of the oscillator can be written as $|c(\omega)| \approx a/\omega_0\gamma >> |c(0)|$.

Meanwhile, from Eq. (1.6) it can be found that the phase of the oscillator changes by π when the frequency ω goes through the resonance. It reveals that there is a delay between the action of the driving force and the response of the oscillator.

When ω increases, the phase increases from $\varphi = 0$ at $\omega = 0$ to $\varphi = \pi/2$ at $\omega = \omega_0$ (at resonance) and to π as $\omega \to \infty$.

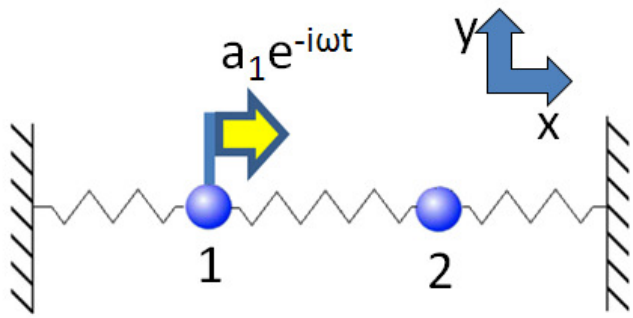

Figure 1.1 Illustration of two coupled interacting oscillators.

It indicates that if the displacement and the external force are in phase before the resonance, they are out of phase after the resonance. One can extend this system to a pair of oscillator coupled by a spring (see Fig. 1.1). Again we may neglect complementary solution since the concentration is in the behavior of the amplitudes after the transient motion decays. The equations of motion can be written as :

$$\ddot{x}_1 + \gamma_1 \dot{x}_1 + \omega_1^2 x_1 + \upsilon_{12} x_2 = a_1 e^{i\omega t},$$

$$\ddot{x}_2 + \gamma_2 \dot{x}_2 + \omega_2^2 x_2 + \upsilon_{12} x_1 = 0 \ , \qquad (1.8)$$

where υ_{12} is defined as the coupling of the oscillators. Firstly, it is assumed that $a_1 = 0$. In this case if the coupling also assumed neglected $(\upsilon_{12} = 0)$, the two free oscillators swing independently with the giving natural frequencies. Meanwhile, the coupled oscillators have two normal modes [69] :

1. Two oscillators swing back and forth together;

2. Two oscillators move in opposite directions.

In order to understand the meaning of eigen-modes, it can be assumed that there are no frictions of the oscillators, $(\gamma_1 = \gamma_2 = 0)$. Then, the eigen-modes of the coupled oscillators can be obtained from

$$(\omega_1^2 - \omega^2)(\omega_2^2 - \omega^2) - \upsilon_{12}^2 = 0 . \tag{1.9}$$

Once the coupling parameter gets weak $(\omega_2^2 - \omega_1^2 >> \upsilon_{12})$, the modes of coupled system can be written as:

$$\tilde{\omega}_1^2 = \omega_1^2 - \frac{\upsilon_{12}^2}{\omega_{12}^2 - \omega_1^2}, \tilde{\omega}_2^2 = \omega_2^2 - \frac{\upsilon_{12}^2}{\omega_{12}^2 - \omega_1^2}, \tag{1-10}$$

These modes are slightly shifted from the modes of independent oscillators in the real axis. Next the general problem of the excited oscillators given in Eq. (1.8) is considered with friction. Therefore the steady-state solutions for the displacement of the oscillators are also harmonic such that:

$$x_1 = c_1 e^{i\omega t}, \; x_2 = c_2 e^{i\omega t} . \tag{1. 11}$$

Thus the amplitudes can be written as:

$$\mathrm{c}_1 = \frac{\omega_2^2 - \omega^2 + i\gamma_2\omega}{(\omega_1^2 - \omega^2 + i\gamma_1\omega)(\omega_2^2 - \omega^2 + i\gamma_2\omega) - \upsilon_{12}^2} a_1 , \tag{1.12}$$

$$\mathrm{c}_2 = -\frac{\upsilon_{12}}{(\omega_1^2 - \omega^2 + i\gamma_1\omega)(\omega_2^2 - \omega^2 + i\gamma_2\omega) - \upsilon_{12}^2} a_1 . \tag{1.13}$$

And the phases of the oscillators can be defined through

$$c_1(\omega) = |c_1(\omega)| e^{-i\varphi_1(\omega)}, \qquad c_2(\omega) = |c_2(\omega)| e^{-i\varphi_2(\omega)} . \tag{1.14}$$

It should be noted that the phase difference between two oscillators is given by

$$\varphi_2 - \varphi_1 = \pi - \theta ,$$

where the extra phase shift θ is addressed by the numerator of Eq.(1.12) as

$$\theta = \tan^{-1}\left(\frac{\gamma_2 \omega}{\omega_2^2 - \omega^2}\right). \tag{1.15}$$

In the case that frictional parameter of the second oscillator is equal to the zero $(\gamma_2 = \theta)$, the coupled system has an effective friction for normal models. It means that the amplitudes of the oscillator are limited. The amplitude of the first oscillator as a function of the frequency of an external force is shown in Fig. 1.2 (a), where $\gamma_1 = 0.025$ and $\upsilon_{12} = 0.1$.

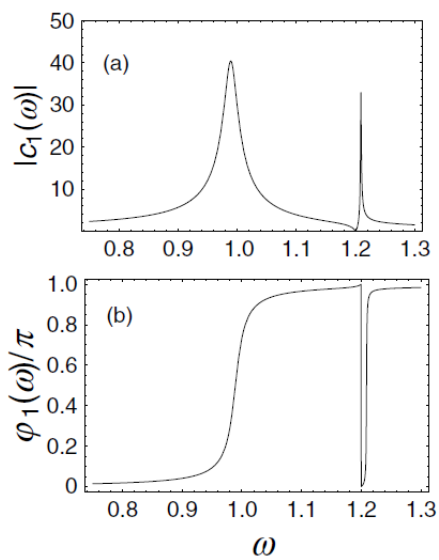

Figure 1.2 (a) The resonant behavior of the amplitude of the first oscillator in the coupled system; where the frequency is in units of the natural frequency ω_1. The amplitude has two peaks (symmetric and asymmetric line-shape) near the eigen-frequencies $\omega = \mathrm{Re}[\tilde{\omega}_1] = 1.0$ and $\omega = \mathrm{Re}[\tilde{\omega}_2] = 1.21$ and it vanishes at the zero-frequency, $\omega = \omega_{zero} = 1.2$ (The modulus of the amplitude is in units of a/ω_0^2). (b) The phase behavior of the first oscillator amplitude around the resonances. (Adapted from Ref. [69])

Two resonant peaks can be seen in the chosen frequency windows: one symmetric at $\omega \approx 1$ and the other asymmetric at $\omega \approx 1.21$. The position of the resonant peaks corresponds to the real parts of the frequencies $\tilde{\omega}_1$ and $\tilde{\omega}_2$, which are determined from the vanishing condition of the denominator of Eqs. (1.12) and (1.13). The imaginary part of the frequency specifies the width of the resonance, so as the single oscillator case.

Since the zero-frequency at $\omega_{zero} = \omega_2 = 1.2$ is right near the peak position the second resonant peak as asymmetric becomes excited. It can be obtained from equation (1.12) that the amplitude of the first oscillator c_1 becomes zero at $\omega = \omega_2$ when $\gamma_2 = 0$. subsequently, the line shape of the second resonance becomes distorted. It should be noted that the amplitude of the second oscillator c_2 tends to a_1 / υ_{12} in Eq. (1.13) at the zero-frequency.

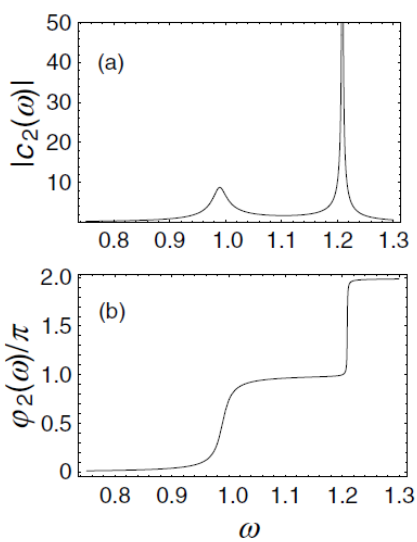

Figure 1.3 (a) The amplitude of the second oscillator as a function of the frequency; where the frequency is in units of ω_1. Two symmetric, resonant peaks appear at the eigen-modes of the coupled oscillators. (The modulus of amplitude is in units of a / ω_0^2). (b) The phase behavior of the second oscillator; where a sequential phase change by π is seen as the driving frequency passes through the resonances. (Adapted from Ref. [69])

Closely examining Figs. 1.2 and 1.3 helps to understand the physical meaning of the amplitude-zero in the first oscillator which is obvious at $\omega = \omega_{zero} = 1.2$ in Fig. 1.3. Due to the coupling between the first and second oscillators, the phases of both oscillators are changed when the driving frequency passes through the resonance. Then both the first and second oscillators are being driven by the frequency of the external force that is less then

resonant frequencies ($\omega < \mathrm{Re}[\tilde{\omega}_1] = \omega_1$, $\mathrm{Re}[\tilde{\omega}_2] = 1.21\omega_1$). When the first oscillator is driven near the resonance ($\omega \leq \mathrm{Re}[\tilde{\omega}_1]$), the amplitude grows to a maximum in Fig. 1.2 (a). Meanwhile, the displacement x_1 of the first oscillator gets the phase $\pi/2$ right across the resonance as seen in Fig. 1.2 (b). Once the frequency passes through the first resonance, but before it meets the zero-frequency ω_{zero}, the first oscillator settles into steady-state motion and the displacement x_1 is eventually π out of phase with respect to the external force. Once the frequency passes through anti-resonance at $\omega = \omega_{zero}$, the phase of the oscillator drops by π abruptly.

When the frequency sweeps through the second resonance, the oscillator gains the phase factor by π. The behavior of the resonance and of the phase the second oscillator as a function of the frequency is straight forward and the results are shown in Fig. 1.3. Two resonant peaks appear and they manifest the symmetric line shapes in Fig. 1.3 (a). In Fig. 1.3 (b), the phase gain of the second oscillator by π can be seen at each time when the frequency passes through the resonance. With concentration on behavior of the coupled amplitude at the zero-frequency, it can be found that the first oscillator is out of phase with the second oscillator as ω goes through ω_{zero}. Meanwhile at this particular frequency, the motion of the first oscillator is quenched effectively by the second oscillator. It shows that the position of amplitude-zero differs from the previous value of ω_2 and is shifted in the real energy axis due to the interaction among the oscillators. It represents the physical meaning of the amplitude-zero in these systems. Therefore, to obtain a simple explanation for the transmission amplitude near a zero-pole region, one can write the transmission amplitude t_{11} in the desired form

$$t_{11}(E) \sim \frac{E - E_0}{E - E_R + i\Gamma} \ , \tag{1.16}$$

where E_R and Γ are the peak position and the width of the resonance, and E_{zero} is the zero-energy of the resonance. After performing a perturbation approximation, the real part of the resonance pole can be written as $E_R = E_{zero} + \delta$, where $\delta = \hbar^2 \nu_{12}^2 \nu_{11} \nu_{22} / m(k_1^2 + \nu_{11}^2)$ and the width $\Gamma = \hbar^2 \nu_{12}^2 k_1 \nu_{22} / m(k_1^2 + \nu_{11}^2)$. Moreover, difference between E_{max} and E_R in the weak coupling limit can be neglected and the expression for the transmission Eq. (1.16) can be cast into the canonical Fano form of equation as below:

$$T(E) = \frac{1}{1+q^2} \frac{(\varepsilon + q)2_0}{1+\varepsilon^2} \quad , \tag{1.17}$$

where q is the coupling parameter ($q = \nu_{11} / k_1$), $\varepsilon = \frac{(E - E_R)}{\Gamma}$ reduced energy and E_R and Γ the peak position and the width of the resonance. The parameter q measures quantitatively the asymmetry degree of resonance line in Fano interference between the evanescent bound states and propagating continuum states. If the coupling parameter q becomes very strong (q>>1), then the Fano profile reduces to a symmetric or Lorentzian lineshape.

Subsequently, generation and application of FR in optical systems have become one of the active research areas, due to high potential applications in sensors, lasers, switches, and nonlinear and slow-light devices [1, 4]. As one of the first attempts to produce FR in classical optics, it has been observed in the internal reflection spectra of prism-coupled square micropillars [70] and in the interactions of narrow Bragg resonances with broad Mie or Fabry–Pérot bands in photonic crystals [17, 18]. However investigation of Fano-type far-field

spectra has been probably started by monitoring light passing behavior through subwavelength apertures in perforated polaritonic membranes, metallic films (extraordinary optical transmission), random photonic structures, etc. In parallel to these developments, generation of FR by plasmonic nanostructure systems also enhanced capabilities of practitioners to monitor the changes in resonances` characteristics due to the sharpness of such resonances. In section 1.1.2 mechanism of the FR in plasmonic materials and metamaterials will be discussed.

1.1.2. Fano Resonance in plasmonic systems

When the conduction electrons in a metal are driven by the incident electric field in collective oscillations, near surface collective electronic oscillations known as surface plasmons come to existence [71, 72]. The plasmons excited by incident light are equivalent to the quasi-discrete levels, which can be modeled with mechanical coupled oscillators as shown in section 1.1.1 [1, 4, 69, 73]. Therefore, the localized maximums and minimums in the optical responses, such as scattering and extinction corresponding to the constructive and destructive interferences among different eigen-modes [1] can attribute to exhibition of FR in plasmonic materials and metamaterials [11].

In plasmonic systems, the dispersion of FR is arising from interference between broad and narrow plasmonic modes. It has been explained that broad spectral line in nanostructures can be excited directly by incident light. But the best method to create a narrow spectral line in the vicinity of this broad resonance is still a subject of debate due to its challenges. Thus far extensive research works on FR have been established to create such narrow spectral lines by indirect excitation of dark modes in plasmonic nanostructures.

Symmetry breaking is one of the most straight forward ways to achieve FR in plasmonic systems [74-110]. It has been shown that symmetry breaking in simple structures, such as metallic nanodisks with a missing wedge shaped slice, possessed capability to excite a FR [111, 112]. Zhang et al. have proved that the Fano-line shape in such structures is a result of the coupling between a hybridized plasmon resonance of the disk and a narrower quadrupolar mode supported by the edge of the missing wedge slice. Another example of symmetry breaking is to deposit a spherical or cubic nanoparticle on an adjacent semi-infinite dielectric [113, 114]. It has been demonstrated that the unique geometry of a perfect cube can also lead to the strong interaction and hybridization of the primitive modes of a nanocube through the underlying substrate. Subsequently, FR in this case can be explained by the substrate-mediated interaction of a dark quadrupolar cube mode with a bright dipolar cube mode [113, 114]. These studies confirm that breaking and tuning the geometry of nanostructures can contribute to the generating narrow band dark mode and its spectral overlap with broad bright modes.

It has been shown that complex and hybrid structures [115-166] can fulfill the FR requirement for bright and dark modes hybridization as well. For instance, a simple combination of a cross shape structure and a nanobar (XI cavity) can provide a clear evidence that once the energy of a dark mode approaches the energy of the bright mode, the FR can be observed as a resonance with asymmetric line shape [167]. In such XI cavities, the coherent near-field coupling takes place between broad dipole and sharp quadrupole modes being excited in the cross, and excited dipole resonance in the bar [167]. An alternative way to generate FR is by forming nanometric apertures in metallic “thin” films [168-174]. Artar et al. [173] presented a method to exhibit multiple spectral optical

properties by fabricating the apertures on multilayer “thin” films. Their proposed structure consists of two complementary metamaterial layers being separated by a small dielectric gap. This gap enables strong near-field interaction in between. Each planar layer possesses bright and dark modes to couple each other through the structural asymmetry, enabling multispectral FR behaviors. In fact, the apertures in multilayer thing films realized so called multispectral plasmon induced transparency.

One more plausible candidate to generate FR is chemically fabricated Fanoshells [68, 175-180]. Fanoshells typically consist of a metallic core surrounded by a dielectric spacer and subsequently another metallic shell [68, 181], while the central core is usually displaced with respect to the metallic core. In these structures, FRs are induced by interaction between dipolar modes of the inner core, and multipolar plasmon modes of the outer shell. Fanoshells possess optical properties similar to so-called nanoeggs, which consist of a dielectric core surrounded by a metallic shell of nonuniform thickness [182]. In another approach, Muhlig et al. [178] combined self-organization and colloidal nanochemistry methods to fabricate clusters consisting of dielectric core spheres which are smaller than the wavelength of the incident irradiation and are decorated by a large number of metallic nanospheres. Such a core-shell system exhibits a dispersive effective permeability, i.e. artificial magnetism [179]. Meanwhile theoretical studies on ultrafast optical dynamics of excitons in nanoshell J-aggregate complexes show their potentials to enhance and tune nonlinear optical properties [177].

Apart from standard electron beam lithography (EBL) [71, 72, 183], some other methods have been reported recently for nanofabrication of structures for FR generating. Farrell et al. [184] have shown that FR generating may benefit from a combined nanoimprint

lithographic and block copolymer self-assembled structures. They used a highly regular dewetting process of a symmetric diblock copolymer that whereby the hierarchal formation of microdroplets and concentric nanorings form. In another approach, it was shown that nanobubbles and nanodroplets can be confined either spontaneously at the suspension/substrate interface, or in the system allowing the assembly of nanoparticles into nanoring-like structures with a flexible control of both the size and size distribution [185]. Furthermore, Vogel et al. [186] reported a successful colloidal lithographic method to construct stacked nanocrescent dimer structures with a separation distance of approximately 10 nm. They used non-closed packed colloidal monolayers as masks and obtained separated nanocrescent dimers. Template-confined dewetting [187], template-guided self-assembly [59], synthesis by seed-directed deposition [188], surfactant-assisted shape-controlled synthesis [189], DNA scaffolding [53] and assembly of gold nanoparticles in spherically confined micro-phase separation structures of block copolymers [190] are some recent novel fabrication methods which were used to fabricate nanostructures exhibiting FR. Laser microlens array lithography, which can realize arbitrary micrometer patterns over a large area at a high speed, is also a promising method to be used in Fano resonance research [191-193]. Angle-controlled colloidal nanolithography as a fast and low-cost fabrication technique [194] is also one of the novel high potential fabrication methods which will be explained in details later in section of oligomers.

One common factor among most of the addressed studies is that the dispersion of FR arises due to interference between broad and narrow spectral lines. It has been explained that the broad spectral line which is typically the result of dipolar modes, can be excited directly by incident light. But creation of high order narrow spectral line in the vicinity of this

broad resonance is still challenging. Plasmonic oligomers consisting of packed metallic nanoelements with certain configurations [45-66] have been proposed as one of solutions to address this issue. In oligomers, FR exhibition does not rely on the high-order modes. In such structures anti-parallel dipole modes arising from the individual elements are responsible for generation of high contrast FRs. Meanwhile the higher sensitivity and polarization-independent optical response of these coupled structures have attracted interest in recent years. A literature review about oligomers can be found in section 1.1.3.

1.1.3. Fano Resonance in plasmonic oligomers

Oligomers are novel nanostructures in which the sharp FR excitation is based on the coupling of the anti-parallel dipole modes [45-66]. This trend is contrary to symmetry broken or complex nanostructures in which FR is the result of the coupling between dipolar and multipolar modes. Oligomers consist of aggregated nanoelements with sufficiently small inter-particle separation. The combination of the plasmon modes of each constituent nanoparticle leads to the formation of collective plasmon modes in the entire structure. Such strongly coupled particles show much higher sensitivities to structural and environmental changes as compared to uncoupled particles. It is demonstrated that in many cases that group theory can be used to identify the microscopic nature of the plasmon resonances [46, 48, 49, 52, 55], e. g. to elucidate the effect of different element configurations on the optical properties of symmetric silver nanosphere aggregations [52].

Initially, optical properties of planar symmetric heptamers, consisting of the central nanoelement and six outer nanoelements arranged in a ring-like fashion, were studied [45, 46, 54]. As can be seen in Fig. 1.4, the resulting FR is due to the hybridization of the plasmons in the central nanoparticle and the ring-like hexamer. Therefore by removing the

central particle one can switch on and off the FR without symmetry breaking. Furthermore, it was shown that the inter-particle separation plays a crucial role in the formation of the collective modes as it determines the coupling strength between the constituents of the heptamer [46]. Small inter-particle gaps result in a strong FR for the compact heptamer.

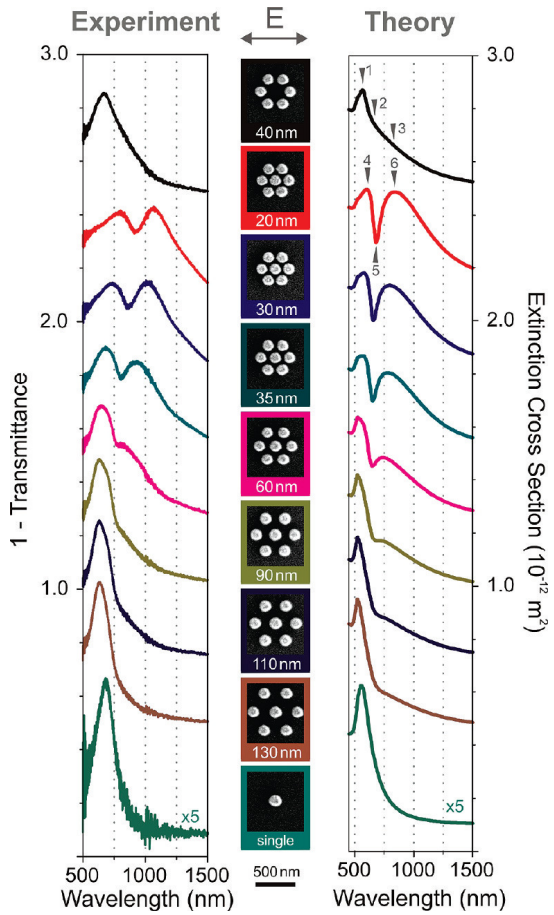

Figure 1. 4 Extinction spectra of a gold monomer, a gold hexamer, and gold hepatmers with different inter-particle gap separations. Spectra are shifted upward for clarity. (left column) The experimental extinction spectra (1-transmittance). (middle column) SEM images of the corresponding samples with indicated inter-particle gap distances. The scale bar dimension is 500 nm. (right column) Simulated extinction cross-section spectra using the multiple multipole method. (Reprinted with permission from Ref. [46], ©2010, American Chemical Society.)

Detailed study of the effect of heptamer component sizes, geometries and inter-particle gaps can be found in Refs. [45, 46]. Meanwhile, it has been shown that gradually varying the size of one satellite nanoparticle gives rise to the drastic reduction of the structural symmetry. The undisturbed heptamer belongs to the symmetry group D_{6h} (C_{6v} if

the substrate is considered), whereas the defective heptamer is of $D_{1h} = C_{2v}$ symmetry ($C_{1v} = C_{1h} = C_s$ if considering the substrate). Although the optical properties of defective heptamers are not isotropic anymore, such structures still have one symmetry axis, which is along the center and the defect particles.

Recently, Lassiter et al. studied another oligomer consisting of a central disk and eight satellite disks known as nonamer. They performed wavelength selected cathodoluminescence (CL) spectroscopy and imaging on such oligomers [195] and demonstrated a recipe for deconstruction of Fano line-shape. They moved across the FR from shorter to longer wavelengths and show that the contribution of the particles in the outer ring diminishes while the contribution from the central particle increases dramatically. CL spectroscopy reveals that under electron beam excitation, there are actually two independent resonances associated with either the center particle or the outer ring and crossover between two CL resonances is located at the same spectral position as the FR dip in the dark field case [195].

In this thesis, far-field and near-field optical properties of designed and fabricated novel oligomers so called pentamers and quadrumers [47, 48, 60-62, 66] are studied in details. These oligomers consist of a central element and four and three satellite surrounding elements, respectively. Apart from exhibition of high contrast FRs, pentamers and quadrumers possess some unique advantages such as potentials to design Fano profile and to provide capabilities for arbitrary light localizations will be discussed in this thesis.

1.2. Research motivation

It was explained that symmetry broken and complex metallic nanostructures have been proposed as good candidates for FR generation but there are a few key challenges in the roadmap for the practical FR applications via such structures to be addressed:

(1) Plasmonic nanostructures which rely on high order dark modes for FR generation are not perfect framework for practical applications. High-order multipolar modes cannot directly couple to the incident light and should be excited by dipole modes [91]. Difficulties in the indirect excitation of the high-order bring FR generating to the bottle neck.

(2) Generally FRs in plasmonic structures appear at certain polarization directions which require a precise control on the path and polarization of incident light in developed FR based devices. Therefore, it would be valuable to design a plasmonic system in which FR can be obtained independently of polarization.

(3) A flexible control over the Fano profile characterized by its linewidth and spectral contrast is highly helpful to realize practical applications. But, there is a lack of a general method to flexibly control the Fano profile, which might determine the overall performance of FR-based devices.

Recently introduced planar oligomers have shown a good platform to address all the issues mentioned above. The reason for the FR emergence in such structures is the destructive interference among the anti-parallel dipolar modes [45-62, 64-66] rather than the challenging excitation of high-order modes [1, 4]. Hence in the planar oligomers, the pronounced FR is more readily to be achieved than asymmetric and complex structures [47,

48]. Meanwhile, symmetric oligomers have one more potential to exhibit FR independently of polarization. In such structures due to the planar symmetric geometries, the excitation polarization does not affect the optical response and it only leads to the rotation of charge distribution pattern in all nanoelements simultaneously.

Based on the number of aggregating elements, oligomers can be divided into a few types such as nonamers [195], heptamers [45, 46, 54], hexamers [49], pentamers [47, 60] and quadrumers [48, 66]. Such structures, which consist of one central element and finite number of surrounding satellite elements, have been widely studied and developed simultaneously in last few years. In this thesis, the attention is given to the pentamers and quadrumers [47, 48, 60-62, 66]. By reducing the number of surrounding elements of nonamers [195] and heptamers [45, 46, 54], we introduced pentamers and quadrumers with modulated ratio between the opposing phase oscillating plasmons. This ratio is increased from 1/8 and 1/6 in the nonamers [195] and heptamers [45, 46, 54] , respectively, to 1/3 in the quadrumers [48, 66] and 2/3 in the pentamers [47, 60]. The influences of element size, gap and symmetry breaking on quantity and quality of FR are also studied and will be presented in this thesis. More importantly in pentamers and quadrumers, we show that one can tune and design the overall Fano shape by decoding excitation subgroups and altering the particle shape of these subgroups, selectively. This novel understanding of the optical response of plasmonic nanoclusters captures some physical aspects beyond the well-known interference mechanism, which would bring about the new scope of FR applications such as slow-light devices and bio-chemical sensing [1, 3-7].

Meanwhile, as compared to the regular oligomers such as nonamers and heptamers, fewer number of surrounding satellite components and their further distances with respect

to each other in pentamers and quadrumers provides more interesting characteristic. In the symmetric pentamers and quadrumers, the near-field energy distribution at inter-particle gaps can be flexibly tuned by changing excitation polarization, while the far-field optical responses, such as FR, are still polarization-independent. This energy localization can be established at a normal incident light of a single source rather than co-illumination by two light sources accompanied by different incident angles or phase shift [87, 196]. It can overcome the spatial restrictions of conventional optics with unique potential applications in nanolithography [197], nonlinear spectroscopy [196] and optical switching [1, 3-7].

1.3. Organization of thesis

This thesis is directed towards to the design, fabrication, simulation and experimental characterization of various types of planar plasmonic quadrumers and pentamers. The scope of this thesis is to generate and optimize FR and localized near-field energy by changing elements` size and geometry, inter-particle gap as well as symmetry breaking in the oligomers.

Chapter 2 indicates the experimental techniques to simulate, fabricate and characterize the plasmonic oligomers. The structures were made by electron beam lithography (EBL) which facilitates a high accuracy and high quality nanofabrication process. Simulations were established by Lumerical FDTD software in which calculations are based on Finite-difference time-domain method. The characterization was carried out by Micro-UV-Visible and Fourier transform infra-red spectroscopy systems.

Chapter 3 presents detailed study on far-field optical properties of oligomers. A novel recipe is introduced to obtain a higher ratio of anti-parallel dipole modes in oligomers. It is

known that nonameric and heptameric geometry leads to an anti-parallel dipole fashion with ratios of 1/8 and 1/6, respectively. In this chapter it is shown that reducing the number of surrounding satellite elements attributes to an increase in the value of this ratio. Moreover, it is found that symmetry breaking in oligomers can give rise to the appearance of an additional subradiant mode that leads to the appearance of the second FR in the same spectrum. It confirms the ability of oligomers to exhibit multi FRs. Finally in this chapter, a method to achieve flexible control over the Fano profile characterized by its linewidth and spectral contrast is presented. We synthesized a deeper study on whole spectral signature of FR and showed that the spectral shape of resonances in plasmonic pentamers can be decoded into two individual contributions from their subgroups. Such subgroups are the real eigen-states whose interference gives rise to the resonance lineshape. This finding helps to design and tune the final profile of FR by selectively altering the particle shape of either subgroup.

In chapter 4 the effect of further reduction in the number of surrounding elements is studied. It is shown that the geometrical configuration of co-planar oligomers allows studying the complex electronic states in co-planar molecules. This argument is proved via a mechanical mass-spring model as an additional analogue as well. Furthermore, the effects of the elements size, gap and geometry of oligomer components on the spectral signature of FR are also investigated.

In Chapter 5, the attention is given to the near-field optical properties of oligomers. It has been shown that all oligomers have the capability to enhance these near-field energies among the gaps up to hundred-folds. These localized electromagnetic intensities are called as hot-spots. Such hot-spots in nonamers and heptamers can take place among all gaps

including the gaps among outer elements and central one as well as the gaps among neighboring outer elements. Therefore, a precise control on the localization of these hot-spots is not realistic. Unlike such oligomers, it is found that near-field energy in pentamers and quadrumers take place only among the surrounding disks and the central one. This characteristic provides the capability to localize and tune the hot-spots among the subdiffraction length scale gaps via polarization orientation as an efficient tool. Subsequently, in this chapter comprehensive extensional study on the effect of nanodisk sizes and the gap among them on the near-field optical properties is presented. Moreover, it is found that unique near-field energy distribution in the asymmetric pentamers can be well tuned to be localized at one, two or three out of the four subwavelength gaps of the pentamer selectively by only changing the polarization orientation of a single light source. Finally, hot-spots characteristics in a novel type of hybrid oligomers consisting of the rotor-shaped central elements are investigated. It is shown that these hybrid oligomers can enhance the near-field energy intensity and localization, significantly while the net optical properties of the system are still kept isotropic.

Chapter 6 gives an overall summary of the research contributions and proposes the future work on plasmonic oligomers.

Chapter 2.

Experiment

In this chapter, detail experimental procedures which were employed for the fabrication, characterization and simulation in this thesis are discussed. The fabrication processes include electron beam evaporation, spin-coating of electro-resist, electron beam lithography, and etching by ion milling. The characterizations are carried out by scanning electron microscope (SEM), atomic force microscopy (AFM), micro UV-Visible and Fourier transform infra-red (FTIR) spectroscopy. The simulations are calculated out with Lumerical software based on finite difference time domain (FDTD) method.

2.1. Fabrication

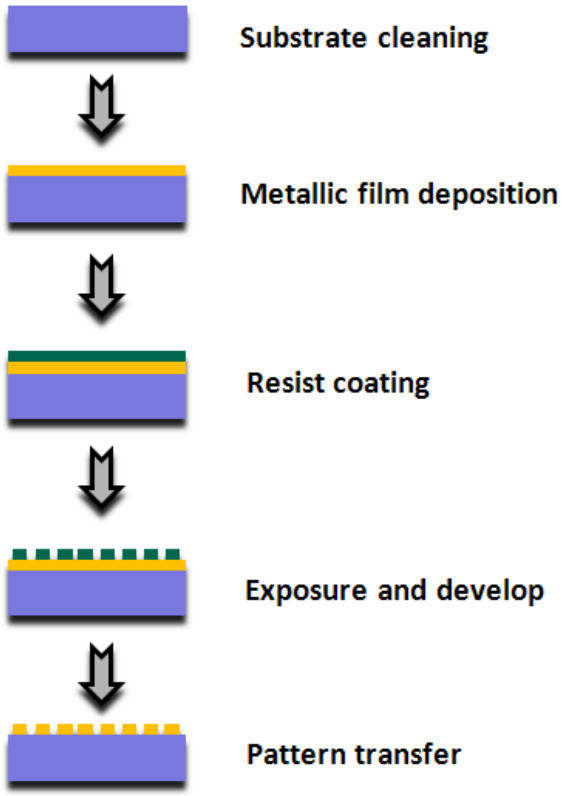

Figure 2.1 Illustration of fabrication steps.

The samples for this research work were fabricated through multi-step processes. Apart from different substrates, such as quartz and silicon which were used, the rest materials and

processes applied on the samples were similar. Since etching approach was used to fabricate the structures, the conductivity and material of the substrates do not play important roles in the fabrication, however later in characterization section it will be explained that the substrate is highly important to measure the optical properties of metallic nanostructures. Figure 2.1 shows the steps of fabrication. These steps are explained in next subsections.

2.1.1. Substrate cleaning

Two kinds of substrates were used in this work. They are (1) n-type silicon wafers with the resistivity less than 1 $\Omega \cdot cm^{-1}$ at a thickness of 500 µm and (2) quartz at a thickness of 400 µm. Si substrates were used to measure the reflection spectra of nanostructures fabricated on them and quartz substrates were used for transmission measurement. To get rid of the possible contamination on samples, the substrates were cleaned by immersing them into the ultrasonic bath with Isopropyl Alcohol (IPA), Aceton, and De-ionized water (DI water) in sequence for 10 minutes each.

2.1.2. Metallic film deposition

Electron beam evaporation system (EB03 BOC Edwards) was used in this work to fabricate the samples. In an electron beam (E-beam) evaporation system, as shown in Fig. 2.2, the deposition chamber is evacuated to a pressure of 10^{-6} Torr [198, 199]. The material to be evaporated is in the form of ingots. E-beams can be generated by thermionic emission, field electron emission or the anodic arc method. The generated electron beam is accelerated to a high kinetic energy and focused towards the ingots. When the accelerating voltage is between 20 ~ 25 kV and the beam current is a few Amperes, 85% of the kinetic energy of the

electrons is converted into thermal energy as the beam bombards the surfaces of the ingots. The surface temperature of the ingots increases, resulting in the formation of a liquid melt. Although some of incident electron energy is lost to excite X-rays and secondary electron emission, the material vapor evaporates from the melted ingot material in a vacuum.

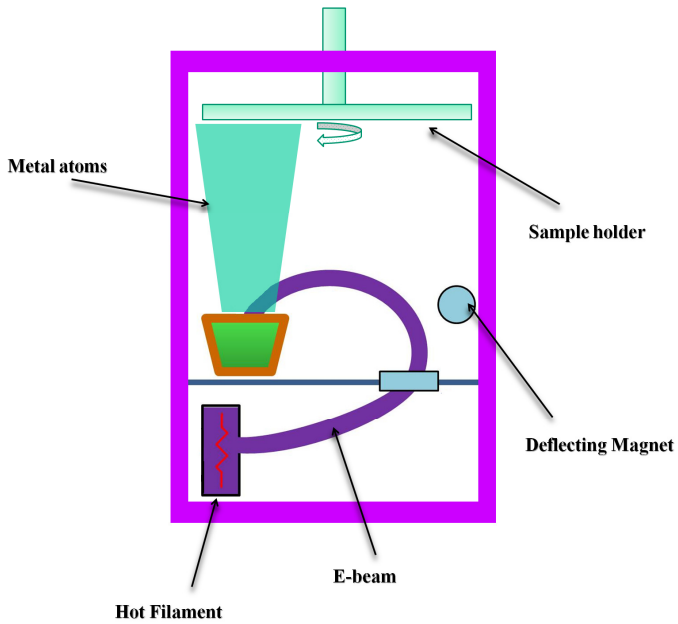

Figure 2.2 Schematic drawing of an electron beam evaporator.

The ingot is enclosed in a copper or carbon crucible, which is cooled by water circulation. The level of the molten liquid pool on the surface of the ingot is kept constant by the vertical displacement of the ingot. In this thesis, Ti and Au are the metallic materials used. Ti is used as adhesion layer between Au and substrates.

2.1.3. Resist coating

The negative electro-resist used in this work is hydrogen silsesquioxane (HSQ). The resist is coated onto the samples by a spin coater after thin metallic film deposition. A few droplets of the resist are dropped on the surface of the substrate until it covers 80% of the surface

area of the whole substrate. The spin coating is a two-step process. The first step is a 5 seconds spinning at a speed of 3000 rpm to ensure the deposited resist spreading out uniformly over the whole surface of the substrate, while the second step is a 60 seconds spin coating at a speed of 6000 rpm. The second step dominates the final thickness of the spin-coated photoresist on the substrate. For the HSQ resist in this study, the thickness of ~ 50 nm was characterized by an ellipsometer. This was then followed by a soft-bake process by a hotplate. The temperature was set at 200 °C and the baking duration was set as 2 minutes. The purpose of the soft-bake is to evaporate excess solvent within the resist, so as to improve the adhesion of the resist to the sample. It should be noted that, due to the surface tension, resist is always not uniformly distributed at the sample edge. However, in the subsequent exposure experiment, the sample edge with the non-uniform resist is out of the exposure area and hence the influence of the thickness non-uniformity is tackled.

2.1.4. Exposure and develop

For fabrications in this research work standard Electron Beam Lithography (EBL) is used. EBL is a lithographic process that uses a focused beam of electrons. It is used to form the circuit patterns which are needed for materials` deposition on (or removal from) the substrate. As compared to the optical lithography which uses light for the same purpose, EBL offers a higher patterning resolution than optical lithography. It is due to the shorter wavelength possessed by the 10-20 keV electrons that it employs. Wavelengths as short as 0.2-0.5 angstroms can be exhibited by the electrons in the energy range that they are being used by EBL. For this research, the voltage of 100 kV and current of 20 pA were applied by an Elonix 100KV EBL system [72].

It should be noted that the resolution of an electron lithography system may be limited by other factors, such as electron scattering in the resist and by various aberrations in its electron optics. Meanwhile unlike the optical lithography, which uses photo-masks to project the patterns, an EBL system does not need any photo-mask owing to the availability of technology that allows a small-diameter focused beam of electrons to be scanned over a surface. But as a disadvantage, an EBL system simply draws the pattern over the resist using the electron beam as its drawing pen. Thus, EBL systems produce the resist pattern in a 'serial' manner, making it slow compared to the optical systems.

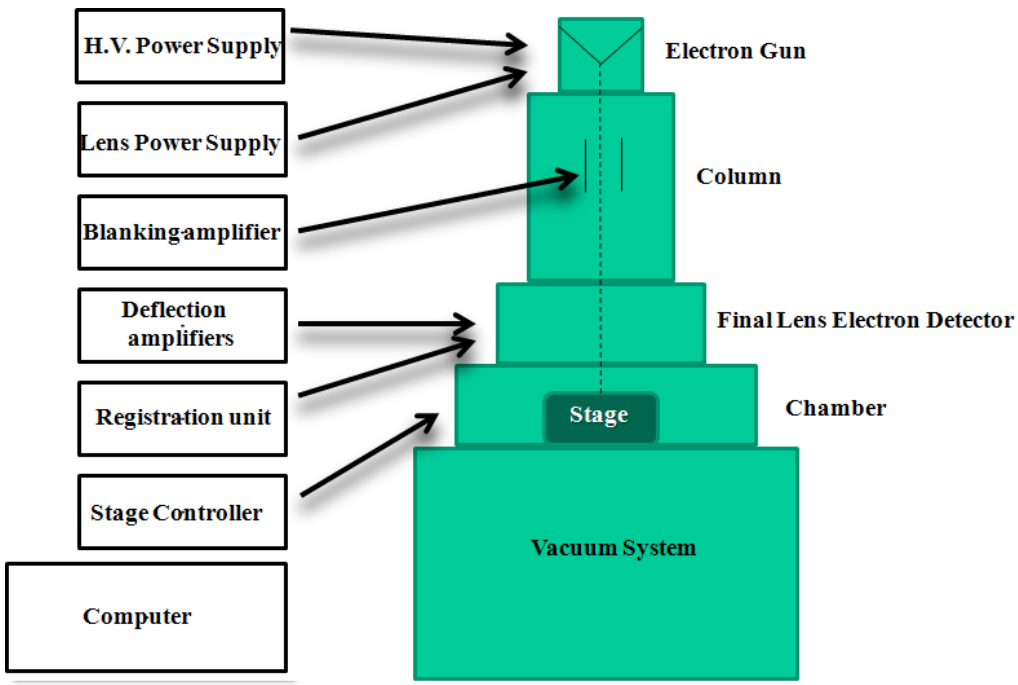

Figure 2.3 Schematic drawing of an EBL system.

As shown in Fig. 2.3, a typical EBL system consists of the following parts:

a) An electron gun (electron source) that supplies the electrons;

b) An electron column which shapes and focuses the electron beam;

c) A mechanical stage that positions the wafer under the electron beam;

d) A substrate handling system that automatically feeds samples to the system and unloads them after processing;

e) A computer system that controls the equipment.

Just like the optical lithography, electron lithography also uses positive and negative resists, which in this case are referred to as electron beam resists (or e-beam resists). E-beam resists are e-beam sensitive materials that are used to cover the wafer according to the defined patterns. HSQ resist which was used in this work was a negative resists. It means that the electron-exposed areas become less soluble, forming a negative image. When electrons strike a material, they penetrate the material and lose energy from atomic collisions. These collisions known as scattering can cause the striking electrons. The scattering of electrons may be backward but it is often forward through small angles with respect to the original path. During the electron beam lithography, scattering occurs as the electron beam interacts with the resist and substrate. This electron scattering has two effects:

i) It broadens the diameter of the incident electron beam as it penetrates the resist and substrate;

ii) It gives the resist unintended extra-doses of electron exposure as back-scattered electrons from the substrate bounce back to the resist.

Thus, scattering effects during e-beam lithography result in wider images than what can be ideally produced from the e-beam diameter, degrading the resolution of the EBL system. In fact, closely-spaced adjacent lines can add electron exposure to each other.

Resist swelling occurs as the developer penetrates the resist material. The resulting increase in volume can distort the pattern, to the point that some adjacent lines that are

not supposed to touch, become in contact with each other. The developer used in this research was Tetramethylammonium hydroxide (TMAH) 25% solved in water. The optimized time of develop is 30 seconds. Then the samples were washed for 15 seconds in water. Resist contraction after the resist has undergone swelling can also occur during rinsing. However, this contraction is often not enough to bring the resist back to its intended form, so the distortion brought about by the swelling remains even after rinsing. Next section explains how this image can be transferred to the metallic film.

2.1.5. Pattern transfer

The exposed and developed patterns need to be transferred into the metallic film. In fact the desired circuit design is protected by the resist and the entire substrate exposed to an etching process. The unprotected material can be etched away. Two most common methods involve the removal of excess material in order to reveal a specific pattern [200].

The first method of etching is wet (chemical) process in which the substrate is submerged in an etching solution. But in this method, the sides of the lines as well as the top surface are exposed to the etching solution. It often results in the sides of the lines being removed (undercut) by the etching solution. Meanwhile, it is impossible to control the rate of undercut. An alternative approach is a dry ion etching method such as Ion beam milling process as shown in Fig. 2.4. In this method, submicron ion particles are accelerated and bombard the surface of the target work while it is mounted on a rotating table inside a vacuum chamber. The resist protects the underlying material during the etching process and everything else exposed to the ion beam etches during the process cycle, even the resist. The key point is that the resist's etch rate is lower than that of the material being etched.

Therefore, a precise optimization prior to the process is required to determine the exact time of process of metallization. Different thicknesses of resist can be used, depending on the thickness and type of metal and the amount of material to be removed.

To ensure uniform removal of waste materials in straight side walls for all features with zero undercutting, target rotation during Argon ions striking are required. It leads to a perfectly repeatable circuit time after time. This precision repeatability is the key strength of the wide collimated ion beam milling process. Other methods such as the chemical process or laser processing, simply do not deliver the same level of precision as compared to an ion beam. The diagram below shows a simplified view of the function of the ion beam miller.

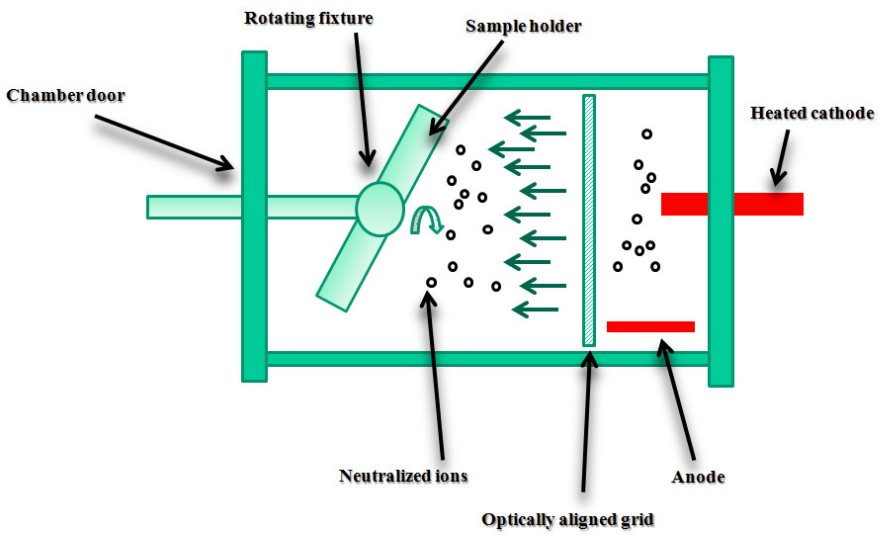

Figure 2.4 Schematic drawing of an ion beam process system.

Argon ions contained within plasma is formed via an electrical discharge which is accelerated by a pair of optically aligned grids. The highly collimated beam is focused on a tilted work plate that rotates during the milling operation. A neutralization filament prevents the build-up of positive charges on the work plate. Importantly, the work plate should be

cooled and rotate during the process so as to ensure uniformity of the ion beam bombardments. Meanwhile the work plate can be angled to address specific requirements.

2.2. Characterization

The established characterization in this thesis, consists of two important parts:

a) Imaging:

   2D and 3D images, provided in this thesis are established by scanning electon and atomic force microscopies. This part of characterization is essential to determine the exact dimension of nanostructure components as well as the gaps among them. Obtained information is highly useful for numerical calculations.

b) Spectroscopy:

   As it was explained before, surface plasmons can be excited by incident photons. Once the structures are fabricated, one should be proved experimentally is to measure the wavelength and intensity of the plasmon-related absorption and emission peaks which are essential for practical applications. It is typically established through spectroscopy which is the measurement of radiation intensity as a function of wavelength. Extinction (1- Transmission) and reflection spectra in this thesis are measured by UV-Visible micro-spectroscopy and Fourier transform infra-red spectroscopy (FTIR).

In this section, these devices are briefly explained.

2.2.1. Scanning electron microscopy

Electrons from a thermionic or field-emission cathode are accelerated through a voltage difference between cathode and anode (from 0.1 to 30 keV) [201]. The smallest beam size at

the virtual source at a diameter of 10 ~ 50 µm from thermionic emission, and a diameter of 10 ~ 100 nm for field emission guns, is demagnetized by a two or three stage electron lens system so that an electron probe of diameter 1 ~ 10 nm is formed at the specimen surface. Fig. 2.5 shows a SEM system configuration.

Primary electrons, striking the sample surface, generate secondary electrons (SE), backscattered electrons (BSE) and Auger electrons (AE). SE and BSE are usually collected, amplified and detected with a scintillator-photomultiplier detector. Scanning electron microscopy (SEM) and Auger spectrometers use similar primary electron columns. In fact, SEM capabilities are usually incorporated into an Auger instrument. Separated detectors are required for secondary and backscattered electrons. To produce images, these electron signals are measured as a function of primary beam position while the beam is scanned in a raster pattern over the sample surface.

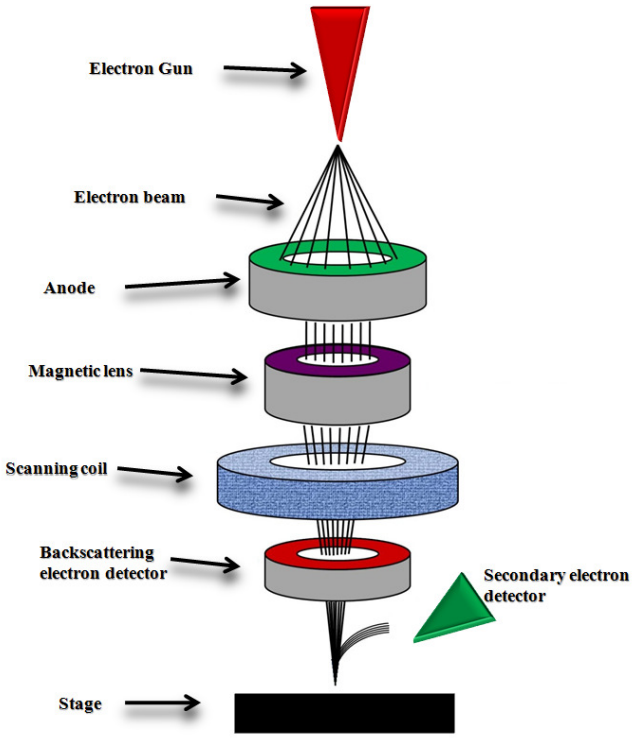

Figure 2.5 Schematic drawing of a scanning electron microscopy system.

Interaction of the primary beam with the sample surface creates an excitation volume, in which electrons are scattered through elastic and inelastic scattering. Electrons in the elastic collisions lose a small fraction of their original energy, but undergo large-angle deflection, which are known as BSE (backscattered electrons). While inelastically scattered electrons lose much of their original energy and those with energy less than 50 eV are known as SE (secondary electrons). SE provides information on surface topography, and is also used in voltage contrast imaging. BSE, on the other hand, provides information on topography and material as the intensity of the BSE signal is strongly related to the atomic number of the specimen, while AE provides information on the chemical composition of thin film and it is usually used in surface analyses. SEM resolution depends on the smallest electron probe spot achievable, while the signal-to-noise ratio is determined by the electron probe current, which decreases with probe spot size. Therefore, electron optics in SEM is designed to achieve the smallest electron spot with the maximum current. The SEM analyses in this work were performed using a Philips XL30 field emission SEM. An accelerating voltage of 30 keV at a working distance of 8 mm was used for conducting samples.

2.2.2. Atomic force microscopy

Atomic force microscopy (AFM) is high-resolution scanning probe microscopy, with resolution on the order of nanometer [202]. In this research work, AFM was used to obtain 3D images on nanostructures. AFMs generally use a laser beam deflection system, where a laser is reflected from the back of the reflective AFM lever and onto a position-sensitive detector (see Fig. 2.6 (a)). AFM tips and cantilevers are micro fabricated from Si or Si_3N_4. Typical tip radius is from a few to 10s of nm. The force is not measured directly, but

calculated by measuring the deflection of the lever, and knowing the stiffness of the cantilever. Hook's law gives F = -kz, where F is the force, k the stiffness of the lever, and z the distance the lever is being bent (see Fig. 2.6 (b)).

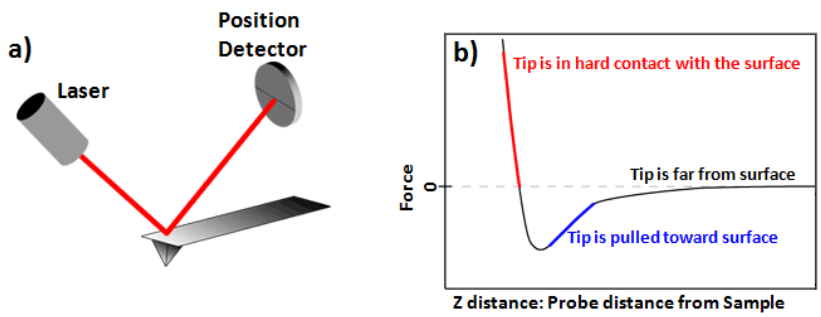

Figure 2. 1 (a) Simplified schematic of a AFM system and (b) diagram of relationship between force and tip distance from the surface for different AFM modes.

There are different modes of measurement, such as contact mode, lateral force microscopy, noncontact mode, tapping mode, force modulation and phase imaging. The images in this thesis are prepared with tapping mode. In this mode, a stiff cantilever is oscillated very close to the sample. One part of the oscillation extends into the repulsive regime, so the tip intermittently touches or taps the surface. The advantage of tapping the surface is improved lateral resolution on soft samples.

2.2.3. Micro UV-Visible spectroscopy

Ultraviolet–visible spectroscopy or ultraviolet-visible spectrophotometry (UV-Vis or UV/Vis) refers to absorption, reflection and transmission spectroscopy in the ultraviolet, visible and near infra-red spectral regions. The basic parts of a spectrophotometer are a light source, a holder for the sample, a diffraction grating in a monochromator or a prism to separate the different wavelengths of light, and a detector.

It should be noted that generally in a UV-Vis spectrometer only one wavelength at a time passes through the sample. For the research work presented in this thesis, a CRAIC QDI 2010 based on a Leica DMR microscope was used which is a UV-Vis spectrometer equipped with a microscope which allows one to acquire spectra of extremely small sample areas [203].

2.2.4. Fourier transform infra-red (FTIR) spectroscopy

Fourier transform infra-red (FTIR) spectroscopy is an alternative method to take spectra which is a measurement technique that allows to record transmission and reflection spectra. Incident light is guided through an interferometer and then the sample. A moving mirror inside the apparatus alters the distribution of light that passes through the interferometer. It allows to measure small areas, such as 50 by 50 um which is used for most of structures in this thesis. The recorded signal represents light output as a function of mirror position. A data-processing technique called Fourier transform turns this raw data into the desired result as a function of infra-red wavelength or wavenumber.

As compared to UV-Vis spectroscopy, FTIR is a more practical method. One reason that FTIR is favoured is that the information at all frequencies is collected simultaneously, improving both speed and signal-to-noise ratio. Another advantage is that a dispersive measurement requires detecting much lower light levels than FTIR measurement. There are other advantages, as well as some disadvantages, but virtually all modern infra-red spectrometers are FTIR instruments. For this research work, FTIR (Bruker Hyperion 2000) is used.

2.3. Simulation

The simulation of this research work are done with Lumerical FDTD software which is a 3D Maxwell solver, capable of analyzing the interaction of UV, visible, and IR radiation with complicated structures employing wavelength scale features. Finite-difference time-domain (FDTD) is one of the fundamental computational electrodynamics modeling techniques which it is a time-domain method. The FDTD method belongs to the general class of grid-based differential time-domain numerical modeling methods. The time-dependent Maxwell's are discretized using central-difference approximations to the space and time partial derivatives. The resulting finite-difference equations are solved in either software or hardware in a leapfrog manner: the electric field vector components in a volume of space are solved at a given instant in time; then the magnetic field vector components in the same spatial volume are solved at the next instant in time; and the process is repeated over and over until the desired transient or steady-state electromagnetic field behavior is fully evolved.

2.4. Summary

For this research work, arrays of oligomers are fabricated by electron beam lithography on silicon and quartz substrates to investigate reflection and transmission responses. A 3-nm thick Ti film was firstly deposited by e-beam evaporation on the substrates to increase the Au adhesion followed by 60 nm Au film. Subsequently hydrogen silsesquioxane (HSQ) as a negative electro-resist (thickness: 50 nm) was spin coated. The samples were baked at ~ 200°C for 120 seconds. After exposure and develop, the nanostructures on the electro-resist were transferred down to the Au films by ion milling. To characterize the fabricated samples,

either UV-Vis-NIR micro spectrophotometer or a FTIR is used. Normal incident lights with x- and y- linear polarizations are applied to excite the structures. Simulated curves are obtained by a three-dimensional finite-difference time domain technique (FDTD) using a perfectly matched layer (PML) around the structures. The dielectric functions used for the simulation was obtained from the experimental data of Johnson and Christy [204].

Chapter 3.

Far-field optical properties of oligomers: Generation of pronounced Fano resonance

In Chapter 1, it was explained that recent advancements in nanofabrication and computational electromagnetics have paved the road to study the collective oscillation of the conduction electrons in the nanoparticle, known as surface plasmons [205]. A particularly important subfield of plasmonics is the study of coupling among noble metal nanostructures. Plasmon oscillation can be localized on a single nanoparticle or may involve many coupled nanoparticles. Many novel optical properties of plasmonic nanostructures and metamaterials are a result of the combinations among plasmons localized on different individual components of the nanostructures [90, 206]. These combinations in complex structures can give rise to collective optical properties, such as Fano Resonances (FR) which are unattainable in regular nanoparticles.

It is well known that plasmon behaviors are highly sensitive to many factors, such as variation in structural geometries and composition, dielectric environment and polarization excitation. It provides wide potentials to tune the SPRs. Therefore, plasmonic systems have proven to be an ideal choice to generate FRs with sharp distinctly asymmetric spectra. As it was mentioned, many studies have been recently undertaken to investigate the effect of the perturbations, such as symmetry breaking [74-110] and fabrication of complex and hybrid plasmonic structures [115-161] to obtain FR in the optical spectra. Among studied nanostructures, plasmonic oligomers are of significant interest due to their fundamental importance as a model system to understand the nature of electromagnetic waves. The mechanism of FR generation in plasmonic oligomers was described in chapter 1 in details.

In this chapter, it is shown that as compared to the nonamers [195] and heptamers [45, 46, 54], the reduction in the number of surrounding disks can modulate the ratio between two anti-parallel dipole modes. It results in the generation of a more pronounced

FR as compared to the other planar symmetric oligomers. Meanwhile, in this chapter interaction among the plasmons arising from the pentamers` nanodisks is modeled via a mass-spring coupled oscillator analogy. It can assist the understanding of the hybridization of the plasmons in nanostructures.

Furthermore, it is shown that the spectral shape of resonances in plasmonic pentamers can be decoded into two individual contributions from its subgroups. This observation enables us to tune and design the overall resonance lineshape by selectively altering the particle shape of either subgroup without a need to change the particle size [45], inter-particle distance [46] or the number of elements of the oligomers [50]. Based on this finding, we demonstrate large spectral shifts (either red or blue) and significant changes in spectral signature of resonance via varying the particle geometry of subgroups, which are particularly important for plasmonic nanosensors.

Finally in this chapter, the effect of geometrical symmetry breaking on the optical properties of the pentamers is investigated [47, 60]. The contribution of the central nanodisk of a pentamer to the FR behavior is revealed by successively physically offsetting its central nanodisk. It is established with the high controlled offset of the position of the central nanodisk, leading to only 3 nm gap with the nearest neighboring disk. It is shown that it leads to the appearance of an additional FR, which is important to show the capability of oligomers to exhibit multi-FRs.

3.1. Destructive interference among dipole modes

As it was explained in Chapter 1, oligomers [45-66] were novel nanostructures in which the sharp FR excitation is based on the coupling of the anti-parallel dipole modes rather than

excitation of high order modes via symmetry breaking or complex nanostructuring. Firstly, the experimental optical properties of planar symmetric heptamers, consisting of one central and six surrounding ring-like nanoelements, were studied [45, 46, 54]. It has been demonstrated that the interference between anti-parallel dipole modes, which leads to a FR exhibition in heptamers, is governed by the presence of the central element [45, 46]. The resulting FR is attributed to the hybridization of the plasmonic dipoles in the central nanoparticle and the ring-like hexamer. In the superradiant mode, all seven clusters oscillate in phase, leading to significant spectral broadening due to strong radiative damping. The subradiant mode is characterized by an out-of-phase oscillation of the plasmonic dipole moment of the inner particle versus the net outer ring-like particles. They can ideally cancel each other completely for which the subradiant mode vanishes. Therefore by removing the central particle, one can switch on and off the FR without resorting to the symmetry breaking. Furthermore, the inter-particle separation plays a crucial role in the formation of the collective modes as it determines the coupling strength between the constituents of the heptamer [46]. Small inter-particle gaps result in a strong FR for the compact heptamer. The similar feature was investigated in nonamers as well, where the plasmons arising from central element oscillate out of phase as compared to the plasmons arising from eight surrounding elements [195].

We found that the reduction of the number of surrounding elements from 8 and 6 in nonamers and heptamers, respectively, to 4 in pentamers, modulates the arrangement of anti-parallel dipole modes. It is found that when the number of the outer disks is reduced, the ratio value between two collective opposite modes increases. It is a result of changing

the ratio between the opposing phase oscillating plasmons from 1/8 and 1/6 in nonamers and heptamers, respectively to 2/3 in the pentamers.

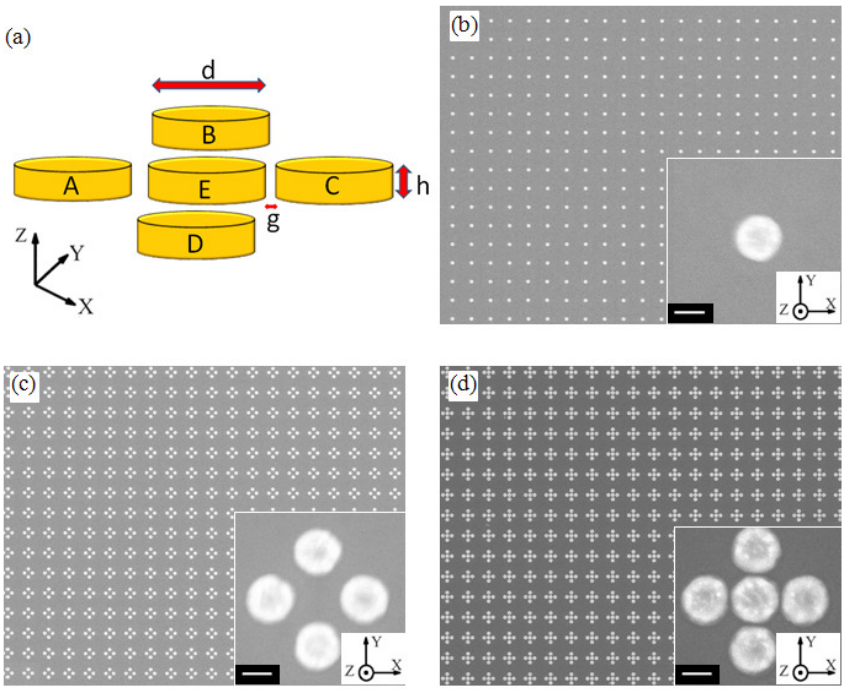

Figure 3.1 (a) Sketch of pentamer arrays. SEM images of periodic array patterns of (b) monomers, (c) ring-like quadrumers and (d) pentamers. Scale bar is 100 nm.

Designed and fabricated pentamer is illustrated in Fig. 3.1 (a). The monomer and ring-like quadrumer are the constituent components of the pentamer. Monomer and quadrumer arrays of the same sizes as those in the pentamer array were fabricated for comparison and analyses. Figures 3.1 (b) ~ (d) show the SEM images of three periodic patterns of monomers, quadrumers and pentamers. The diameter and height of disks are 142 nm and 60 nm, respectively and the gap between disks in pentamers is 18 nm. Since the arising plasmons are extremely sensitive to the shapes of structures, significant efforts have been made to fabricate well shaped nanodisks with low size variation.

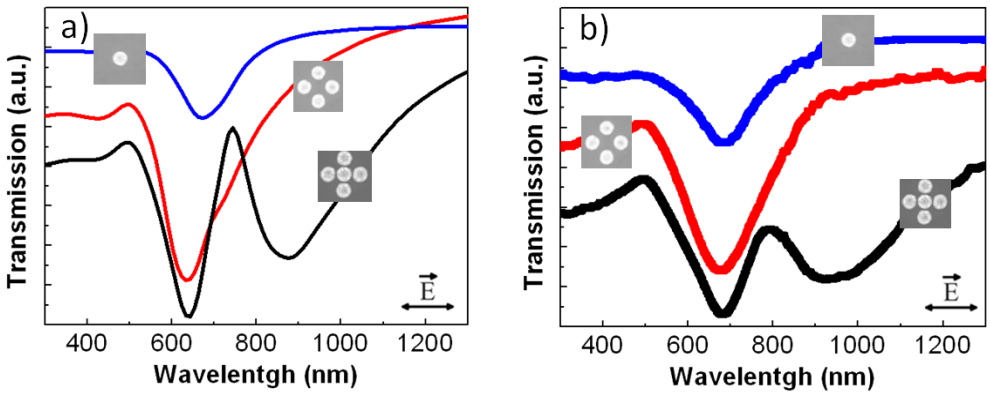

Figure 3.2 (a) Simulated and (b) experimental transmission spectra of monomers, quadrumers and pentamers at x-polarized normal incidence.

In order to gain physical insight into the coupling between nanodisks` plasmons, the optical responses of plasmonic monomers, ring-like quadrumers and pentamers were simulated as shown in Fig. 3.2 (a). The measured transmission spectra (via Micro UV-Visible spectroscopy) of the structures fabricated on the quartz substrates are also displayed in Fig. 3.2 (b). As can be seen, measured and simulated spectra are in good agreement. The transmission spectra of the Au monomers and ring-like quadrumers plotted in Figs. 3.2 (a) and (b) reveal the excitation of dipolar mode with a symmetric profile. Meanwhile, the transmission dip of the quadrumer spectrum is deeper than that of the monomer spectrum due to the existence of more nanodisks on the substrate. From the transmission spectra, it can also be observed that the ring-like quadrumer structure behaves similarly to the isolated monomer due to the well-separated configuration of the nanodisks. But a unique spectral feature appears when a central nanodisk is introduced into the center of the ring-like quadrumer to form pentamer structure. In this case, the dipolar plasmon, arising from the central disk, hybridizes with the ring-like quadrumer dipolar plasmons, allowing the formation of a subradiant collective mode in addition to the superradiant collective mode [110] resulting in the appearance of FR signature in transmission spectra.

Importantly, it is found that unlike the nonamers and heptamers, anti-parallel dipole mode in the pentamers is not arising from the central element versus ring-like surrounding elements. It is found that antiphase oscillation between the plasmons is arising from three middle disks versus the plasmons of two other disks at the bottom and top. The clear evidences for this argument can be seen in charge distribution plots corresponding to ring-like quadrumers and entire pentamer. The orientation of charge distributions in the quadrumer before and after the resonance around the wavelengths of 600 nm and 700 nm are shown in Figs. 3.3 (a) and (b). These charge distributions display that the plasmons in disks A, B, C, and D oscillate in phase, leading to the excitation of a broad superradiant mode centered around 665 nm, where the direction of oscillation gets reversed.

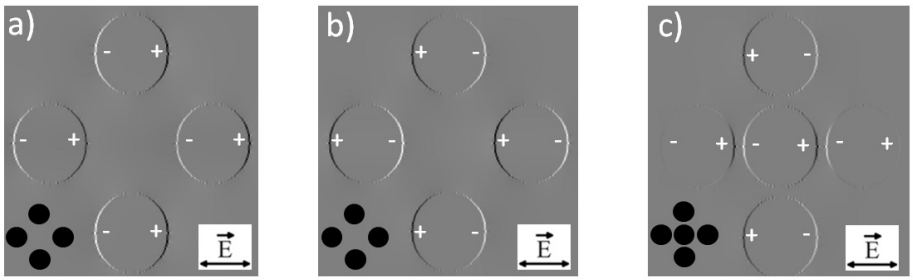

Figure 3.3 Calculated charge distributions for the ring-like quadrumer (a) before the resonance at 600 nm and (b) after the resonance 700 nm and (c) Charge distribution of the pentamers structure at a wavelength of 760 nm.

The charge distribution pattern in a single pentamer at a wavelength of 760 nm is plotted in Fig. 3.3 (c). It shows the configuration of anti-parallel modes where disks A, E, and C (see illustration in Fig 3.1) oscillate in the opposite phase with respect to disks B and D. The effect of the anti-parallel dipolar modes in the pentamers leads to the formation of the subradiant mode. It can be observed in the transmission spectra in an asymmetric line-shape known as FR around 760 nm in Fig. 3.2 (a). The existence of FR in the pentamers demonstrates that the condition of destructive interference between the subradiant mode

and the superradiant mode is sufficiently fulfilled. It is a proof that in the pentamers the superradiant mode becomes excited when the plasmons of all the nanodisks or particles oscillate in phase. While the signature of the subradiant mode becomes apparent when the opposite anti-parallel dipolar moments appear [45, 46] leading to a reduction in net dipole moment and hence a diminished coupling to incident light**.**

3.2. Mass-spring mechanical model

Optical responses of the pentamers can be modeled by a mass-spring analogue [47, 60] which consists of five coupled interacting oscillators illustrated in Fig. 3.4 (a). Here, two hypotheses are argued. Firstly, the springs among the outer disks in the oscillator system are neglected since the outer disks in the pentamers do not have significant interactions between each other. This can be inferred from the transmission spectra of the quadrumers in Fig. 3.2 where a dipole resonance identical to the monomer is seen. Secondly, the interacting system of the five coupled oscillators can be simplified to a three coupled interacting oscillators system, because the coupling among disks A and C with respect to disk E are similar, as well as disks B and D with respect to disk E. Figure 3.4 (b) displays the simplified system in which mass 1 represents, disk E, mass 2 represents disks A and C, and mass 3 represents disks B and D. This model is an extension of the classical two oscillators system which was used to study the nature of FR [69] and three oscillator system similar to the analogous of Fano-shell structures [68]. In Fano-shell model, all three oscillators are connected to each other because of direct effect of dipole, quadrupole and dark modes on each other under optical excitation. But in the model presented in this work, the spring between oscillators 2 and 3 can be neglected since the interaction of ring-like disks in

pentamers can be neglected since plasmons arising from each surrounding disk just approach the central disk`s plasmons individually during optical excitation [47].

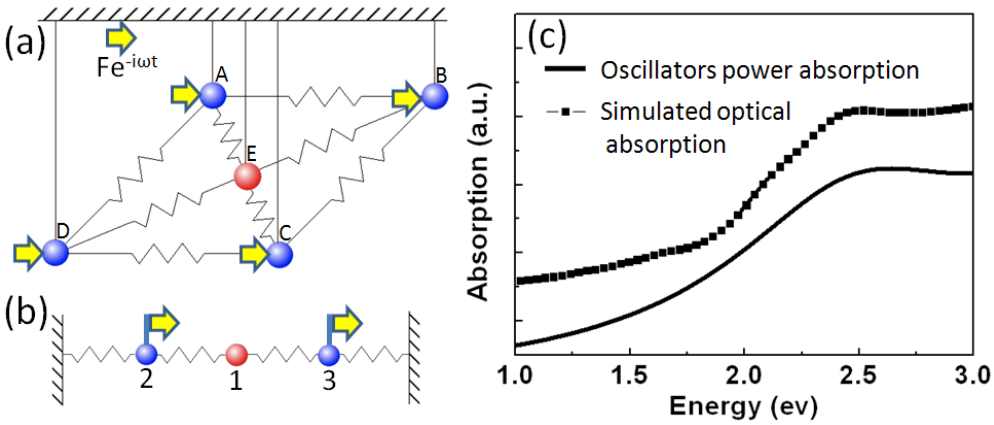

Figure 3.4 (a) Five coupled interacting oscillators representing the pentamer optical responses, (b) simplified three coupled oscillators and (c) simulated plasmons absorption spectra by FDTD (dot line) and calculated power absorption in the oscillator model (solid line).

The mass values in this model are assumed as $m_1=m_2=m_3=1$ and all springs are the same. As explained before, the subradiant mode is a result of adding the central disk. Therefore the outer oscillators are taken to be driven by a harmonic force **F**(t)= **F**$e^{-i\omega t}$ as the bright mode exhibitors. Subsequently, in the simplified system the oscillators 2 and 3 are taken to be driven by a harmonic force. Unlike mechanical model belonging to Fano-shell structures [68] in which the dipole bright mode is assumed as the responsible for exciting the quadrupolar mode and subsequently subradiant dark mode and only one oscillator is driven by harmonic force. For coupled oscillators model in this work, the motion equations of oscillators |1>, |2> and |3> are solved in terms of displacements x_1, x_2 and x_3 from the equilibrium positions:

$$\ddot{x}_1(t)+\gamma_1\dot{x}_1(t)+\omega_1{}^2x_1(t)-\Omega^2x_2(t)-\Omega^2x_3(t)=0, \qquad (3.\ 1)$$

$$\ddot{x}_2(t)+\gamma_2\dot{x}_2(t)+\omega_2{}^2x_2(t)-\Omega^2x_1(t)=Fe^{-i\omega t}, \qquad (3.\ 2)$$

$$\ddot{x}_3(t)+\gamma_3\dot{x}_3(t)+\omega_3{}^2x_3(t)-\Omega^2x_1(t)=Fe^{-i\omega t}. \qquad (3.\ 3)$$

where ω_1, ω_2 and ω_3 are oscillation frequencies, corresponding to the oscillators 1, 2, and 3, respectively, and Ω coherent coupling frequencies between interconnected oscillators which represents the coupling between anti-parallel modes in the optical system. γ_1, γ_2 and γ_3 are the friction coefficients which are used to account for the energy dissipation of |1>, |2> and |3>, respectively. These friction coefficients represent the dissipated energy among nanodisks during energy transformation at optical excitation. By tuning the coupling between bright mode and dark mode (Ω^2=1.69) and other parameters (ω_1=2.5 eV, ω_2=3.1 eV, ω_3=5 eV, γ_1=1, γ_2=42E-2, γ_3=20E-2 and F=10), the absorption power of the oscillator system reproduces the optical absorption of the pentamer. Figure 3.4(c) shows the comparison between absorbed powers of the oscillator system calculated by equations (1) to (3) with the FDTD simulated plasmon response of the pentamer. As it was seen in Fig. 3.2 (a), in pentamers the transmission spectra possess almost a reverse trend. Consequently the absorption spectrum does not experience a pronounced peak as can be seen in Fig 4(c). However it keeps increasing with the rise of the energy. The trend which is almost reproduced by absorption response of the classical oscillators model.

3.3. Influence of components` geometries on FR

In this section, the influence of nanodisk dimensions and the gap among them on the optical properties of pentamers are studied [61]. For this purpose, the sizes of all components in each set are taken as a constant. Table 1 lists out the dimensions and sizes of 6 different sets of pentamers based on the illustrated pentamer unit cell.

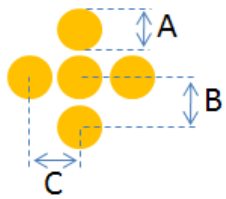

	I	II	III	IV	V	VI
A	130	130	130	110	110	110
B	180	160	140	180	160	140
C	180	160	140	180	160	140

Table1. Dimensions (nm) of 6 various types of pentamers.

In the proposed pentamers Types I, II and III, disks size is kept constant while the gaps among disks are changed. Similarly pentamers Type IV, V and VI possess similar disk size but different gaps. Since the change in size and gap affects the optical properties, transmission spectra of each set is simulated and shown in Fig. 3.5 (a). It helps to determine the wavelength in which the destructive interference vanishes and the structure resumes to exhibit plasmons constructively.

Figure 3.5 reveals that the gap size among the disks plays a more important role than the disk size in terms of amplitude and full width at half maximum of Fano-like shape spectra. As can be seen, the pentamers Types I and V with 50 nm gap among disks and different disks dimensions, exhibit almost similar asymmetric Fano-shape spectra. The similar trend can be seen in the pentamers Types II and VI, in which though the disk sizes are different, their optical properties are similar. The gap among the disks in these two pentamers is 30 nm. These calculated transmission spectra of pentamers reveal this conclusion that the gap size makes more sense as compared to disk dimensions. A comparison among transmission spectra among pentamers Type I, II, and III, supports this conclusion clearly with highly different spectra while disks diameters are constant at 130 nm but the gaps are varying. The same trend can be observed in comparison among pentamers Type IV, V and VI.

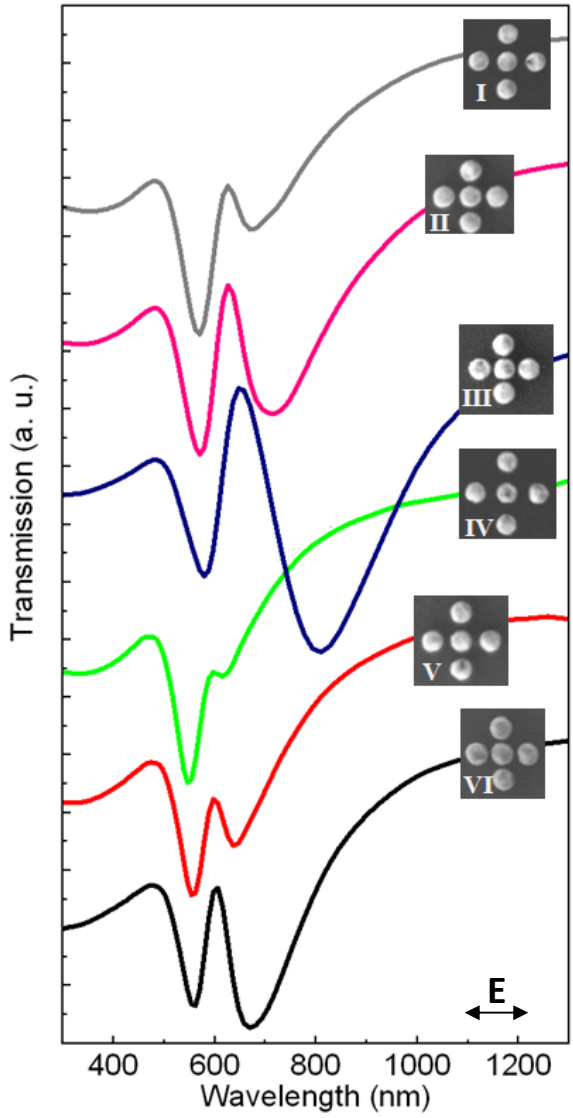

Figure 3.5 Simulated transmission spectra of 6 various types of pentamers at x-polarized normal incidence.

3.4. Subgroups decomposition

It is well known that applications of FR in lasing, switching, nonlinear and slow-light devices, particularly in biosensing, highly based on the sharpness dispersion of FR [1, 3-7]. However, it lacks a general method to control flexibly the Fano profile featured by its linewidth and spectral contrast, which in fact largely determine the overall performance of Fano-

resonance-based devices, such as the detection limit of a biosensor employing this type of resonance. On the other hand, the strong hybridization feature at the Fano extinction dip in oligomers prevents an intuitively understanding and designing of the overall profile. In order to explain the difference observed between the spectra obtained with electron-beam or with plane wave excitation, a significant step forward was recently done by Halas and coworkers [195]. They discovered that a deconstruction of the nanocluster is possible; such a deconstruction was given by the superposition of a subradiant and a superradiant state of the system [195].

In this section, we describe a general recipe that allows one to tailor easily but significantly the overall spectral profile in plasmonic oligomers. We show that the spectral shape of resonances in plasmonic pentamers can be decomposed into two individual contributions from their subgroups. Remarkably, in the particularly considered systems, such subgroups are not due to the superposition of a subradiant and a superradiant state as described in Ref. [195], but they are the real eigen-states of the subgroups which interference gives rise to the resonance lineshape.

Figure 3.6 shows detail optical properties consideration of an array of pentamers consisting of 140 nm diameter circular-shaped disks with 20 nm inter-particle distances. Figures 3.6 (a) and (b) show the simulated (black line) and the measured extinction (via FTIR) spectra in good agreement. Both spectra are dominated by a remarkable extinction dip, which is classified as a FR, akin to previous investigations of pentamers in this chapter. Such a FR occurs due to the destructive interference between a superradiant mode arising from the dipole moments of all the components oriented parallel to each other and a subradiant mode where the dipole orientations are anti-parallel.

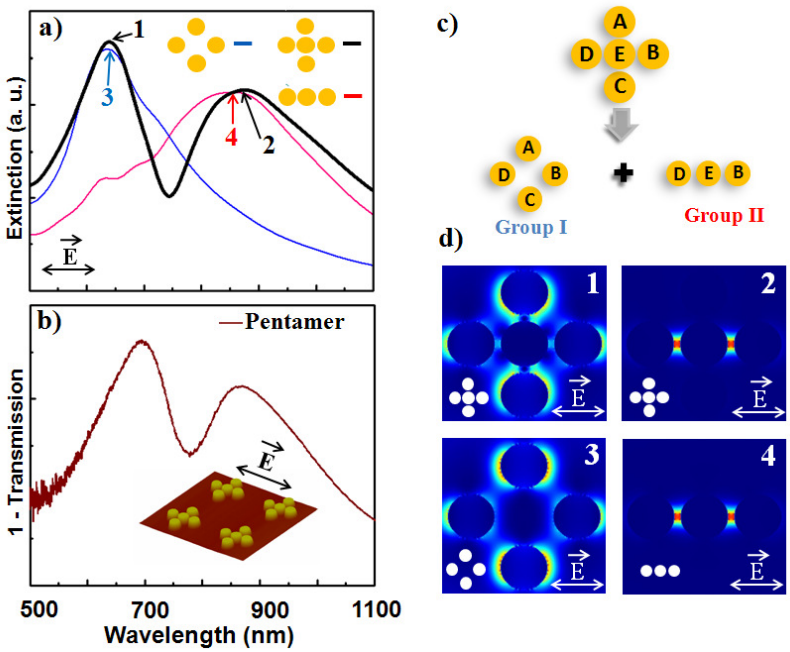

Figure 3.6 (a) Simulated extinction spectra of an individual pentamer (black curve) and the two subgroups (blue and red curves). (b) Measured extinction (1-Transmission) spectrum of the pentamer array at normal incidence. The inset shows a 3D AFM image of the pentamers and the incident polarization. (c) Sketch of decomposing a pentamer into Groups I and II. (d) Electric field intensity distribution in the pentamer at peaks 1 and 2 and in the two subgroups at their respective scattering peaks 3 and 4. (Adapted with permission from Ref. [66], ©2012, American Chemical Society.)

Importantly in this section, we take a different perspective to understand the overall spectral characteristics of pentamers. Instead of exploring the formation mechanism of the extinction dip, we focus our attention on the origin of the two peaks. A useful clue is that the two dominant peaks in Fig. 3.6 (b) seem to be well described by two separate resonances given by two subgroups (see Fig. 3.6 (c)). This intuition is further confirmed by calculating the electric-field intensity distribution in the quadrumer at the two peak wavelengths. The left panel of Fig. 3.6 (d) clearly demonstrates that at the first peak position, four outer disks are efficiently excited, inducing strong field enhancements around each particle while the central disk is relatively dark. Such a selective excitation of different particles can be also seen at the second peak position where the three middle disks become dominant, leaving the other two disks at the top and bottom completely dark. Based on these observations, we

propose that the complex optical excitation in the whole pentamer structure can be decomposed into two separate contributions from its subgroups, group I consisting of the outer four disks and group II of the middle three disks (see Fig. 3.6 (c)).

Following this idea we calculate the extinction of the two subgroups separately (blue and red lines in Fig. 3.6 (a)) and we compare them with the extinction of the full nanostructure (black line in Fig. 3.6 (a)). Note that the curves in Fig. 3.6 (a) are in the same units. Indeed, the extinction spectra from the two subgroups overlap well with the two peaks of the pentamer extinction spectrum in terms of both the position and amplitude (see Fig. 3.6 (a)), demonstrating that the overall spectral response of the pentamer is due to the interaction of the separate excitations of the subgroups at different wavelength ranges. Curiously, results in Fig. 3.6 (a) suggest that the interaction of the two subgroups is such that each subgroup is not active at the same range of frequencies; while the first part of the spectrum is dominated by the group I and the second part by the group II (see Fig. 3.6 (a)). In other words, the total spectrum of the pentamer is the convolution of the two separate subspectra. Note also that, at the peak frequencies the electric near-field distribution of each subgroup is similar to that obtained for the complete nanocluster (see Fig. 3.6 (d)), confirming the decomposition assumption.

3.5. Geometrical hybridization

Understanding the nature of the spectral response in nanoclusters in the previous section is a key point for intuitive design of the resonance lineshape. For instance, we will see in the following, some examples on how to use the oligomer decomposition idea for spectral modification. Having the pentamer decomposition of Fig. 3.6 (c), we can change the central

particle shape and in this way we modify only the optical property of group II, i.e. only the second resonance (red curve Fig. 3.6 (a)) but leaving the first one unmodified (blue curve Fig. 3.6 (a)). Also we can change for example only the external nanoparticles, modifying both groups in this way. Those situations are shown in Fig. 3.7. It can be seen that by changing the shape of the nanoparticle but keeping the particle size and inter-particle distance as constants, a flexible remodeling of the overall spectral shape can be obtained, manifested by a systematic variation in the relative height of the two peaks as well as the resonance linewidth of the spectral dip. More specifically, replacing the center circularly-shaped disk of the pentamer shown in Fig. 3.6 by a square- or triangle-shape nanodisk, allows for significant tuning of the peak-dip contrast and the resonance full-width-at-half-maximum (FWHM) (see the first two cases in Fig. 3.7), which are two crucial parameters to realize high-resolution plasmonic biosensors.

More pronounced modification of the spectral profile can be obtained by changing the particle shape of the outer four disks in the pentamer (see the last three cases in Fig. 3.7) because the spectral response of both subgroups is altered in this way. Meanwhile, it is also possible to modify the particle size and inter-particle distance of the subgroups, and hence open two extra degrees of freedom in the spectral design, which are particularly important to shift the peak or dip positions. It is worthwhile to note that different degrees of interference obtained for the quadrumers and pentamers seems to be linked to the different degrees of the nanocluster symmetry. This can be another valuable parameter important for modelling the spectrum.

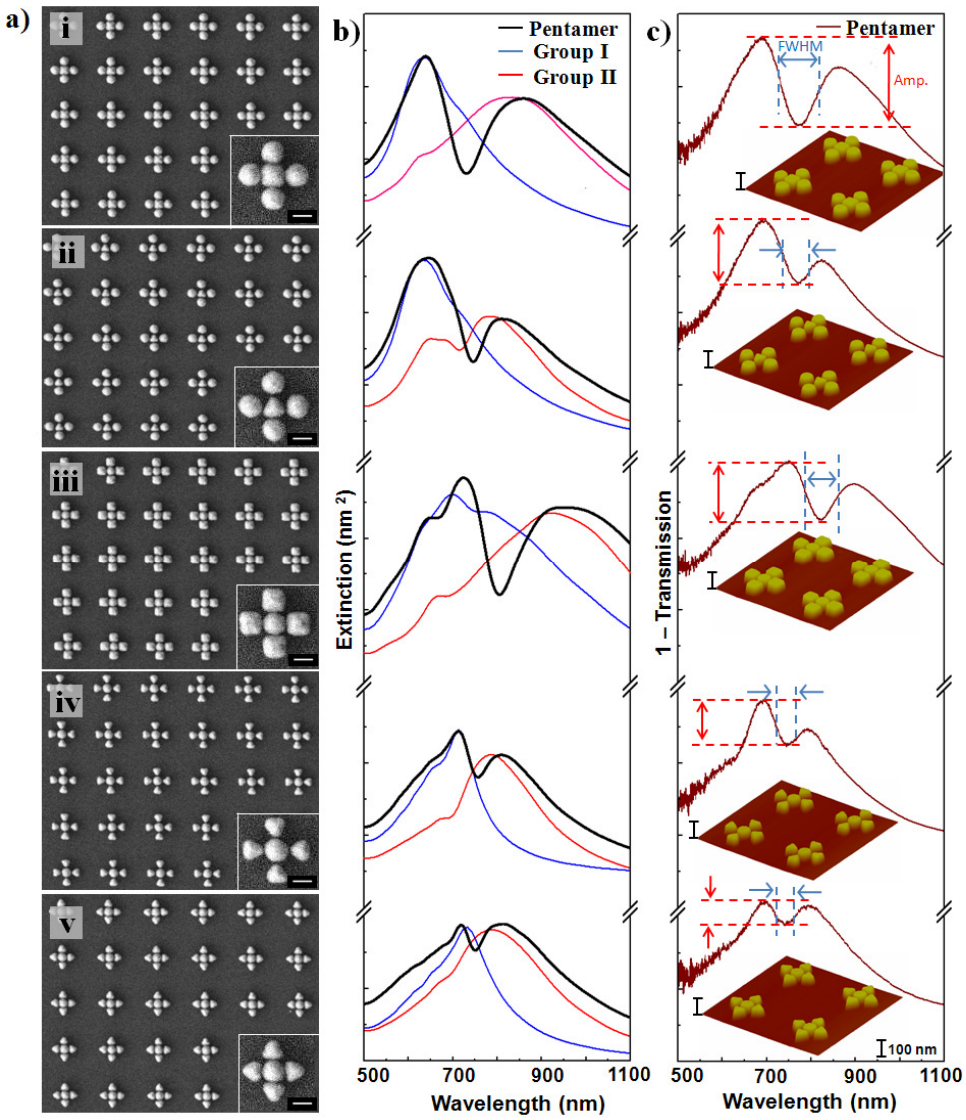

Figure 3.7 Tuning of resonance linewidth and spectral contrast of plasmon resonances in different pentamers. (a) SEM images of hybrid pentamers consisting of differently-shaped elements. The scale bar in each image is 100 nm. (b) Simulated extinction spectra for the pentamers (black curve) and their two subgroups (blue and red curves). (c) Measured extinction spectra for the same pentamers at normal incidence, along with 3D AFM images of the nanostructures. (Adapted with permission from Ref. [66], ©2012, American Chemical Society.)

3.6. Monolith oligomeric structures

It been shown in oligomers is that symmetric oligomers such as nonamers [195], heptamers [45, 46, 54], pentamers [47, 60] and quadrumers [48, 66] etc. are polarization independent structures. In other words far-field optical properties of such structures are isotropic. In this

section, the influence of gap filling in oligomers, particularly in pentamers is studied. It is shown that once the gap among the components is completely filled, resulted monolith 90° rotor-shaped structure still exhibits polarization-independent far-field properties. However, the signature of FR entirely disappears.

Subsequently, the central element of the regular oligomers is replaced by rotor-shaped structures and a new type of hybrid oligomers is introduced. In fact this hybrid structure is a result of the combination of the regular oligomers consisting of all circular components and rotor shaped structures while both these structures are separately isotropic. Therefore the resulting hybrid oligomers are proved to exhibit far-field optical properties independently of polarization excitation as well. These far-field properties are studied in detail in this section. Meanwhile, such structures result in significant enhancement in near-field optical properties of oligomers which is out of scope of this chapter. Near-field properties of oligomers and subsequently hybrid oligomers will be studied in detail in Chapter 5.

3.6.1. 90° rotor-shaped structures

In this section, it is shown that the symmetry properties of monolith rotor-shaped nanostructures have an impact on the propagation of surface plasmon polaritons (SPPs) being excited in such nanostructures [62]. It was investigated that in the certain orientations of 90° symmetric rotor-shaped nanostructures have a wave-guiding effect on propagating SPPs. As a result, the optical properties of such nanostructures are polarization-independent (isotropic).

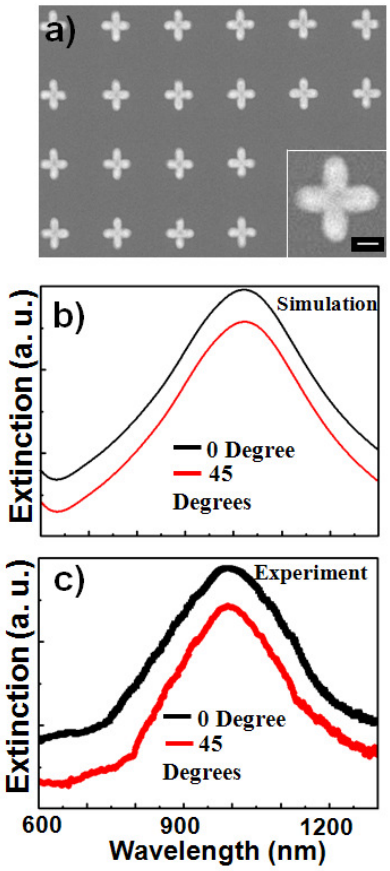

Figure 3.8 (a) SEM images of 90° symmetric rotor-shaped nanostructures, (b) simulated and (c) experimental extinction spectra of the corresponding structures in (a) at indicated polarization excitation with respect to x-axis. Scale bar is 100 nm.

The designed and fabricated arrays of 90° symmetric rotor-shaped nanostructures and corresponding simulation and experimental Extinction (1 – Transmission) spectra are shown in Fig. 3.8. The diameter and height of each individual nanorotor are 350 nm and 60 nm, respectively. The polarization independent far-field optical properties can be seen clearly in the both simulated and experimental results in Figs. 3.8 (a) and (b). This rotor-shaped structure as an individual nanostructure exhibits just a SPR and not a FR.

3.6.2 Hybrid pentamers with central rotor-shaped element

It has been shown that pronounced tunable FR which can be obtained independently of polarization is an important outcome of pentamers. Meanwhile in section 3.6.1 it was

observed that when the gaps among the pentamers` components are filled, although the signature of FR disappears, the far-field optical properties are still polarization independent. The influence of the replacement of the central circular elements of pentamers by rotor-shaped nanostructures with properly reduced sizes is considered in this section. It is shown that the resulting hybrid oligomers can also exhibit an isotropic FR. Figures 3.9 (a) shows the designed and fabricated arrays of the hybrid pentamers.

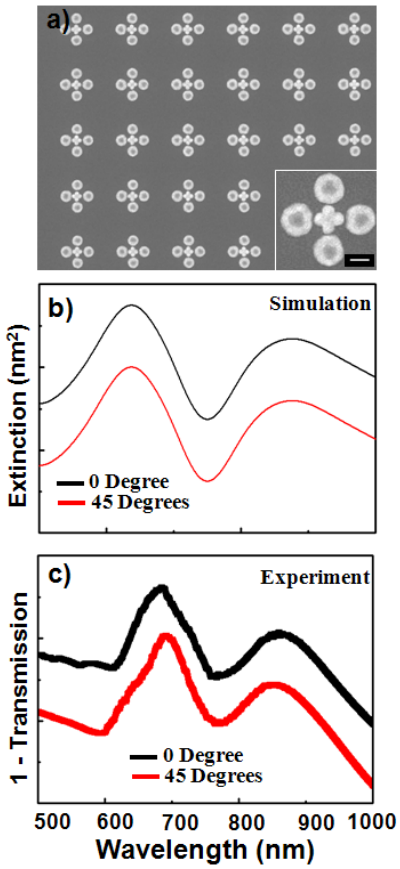

Figure 3.9 (a) SEM images of designed hybrid pentamers and quadrumers, (b) simulated and (c) experimental extinction spectra of the corresponding structures in (a) at indicated polarization excitation with respect to x-axis. Scale bar is 100 nm

In order to have proper comparison with regular oligomers consisting of all circular components, the sizes of surrounding satellite disks are still kept at 140 nm. The central rotor-shaped structure is reduced to have a 20 nm gap with all satellite elements. Figures 3.9 (a) and (b) show corresponding simulated and experimental extinction spectra (measured via

micro UV-visible spectroscopy), respectively. Good agreement can be seen between the simulated and experimental results. Extinction spectra are measured and calculated at 0 and 45 degrees with respect to x-axis. These spectra reveal that the combination of the isotropic rotor-shaped nanostructures and the isotropic oligomers also leads to the exhibition of the isotropic pronounced FRs at ~ 760 nm.

3.7. Symmetry breaking

In this section, the effect of symmetry breaking on the optical properties of the pentamers is investigated. Here the contribution of the central nanodisk of a pentamer to the FR behavior is revealed by physically offsetting its central nanodisk. It is established with the high controlled offset of the position of the central nanodisk, leading to only 3 nm gap with the nearest neighbor disk [60]. It is shown that it leads to the appearance of an additional FR as well as unique spatial energy distribution which can find potential applications in bio-chemical detection [45].

The designed and fabricated pentamers, accompanied by corresponding simulation and experimental reflection spectra, are shown in Figs. 3.10 (a) to (c). The diameter and height of each individual nanodisk are 125 nm and 50 nm, respectively. Type I pentamer shown in Fig. 3.10 (a) is the symmetric pentamer in which the central nanodisk possess equal gaps to all four surrounding disks. But Type II and Type III pentamers, shown respectively in Figs. 3.10 (b) and (c), are asymmetric pentamers with an offset of the central disk position at 6 nm and 12 nm, respectively. Therefore, the gaps between the central disk and other disks for the Type I pentamer are 15 nm. In the Type II and Type III pentamers, the offsets of the

central disk position results in a smaller gap between the central disk and the nearest neighbor disk at a gap size of 9 and 3 nm, respectively.

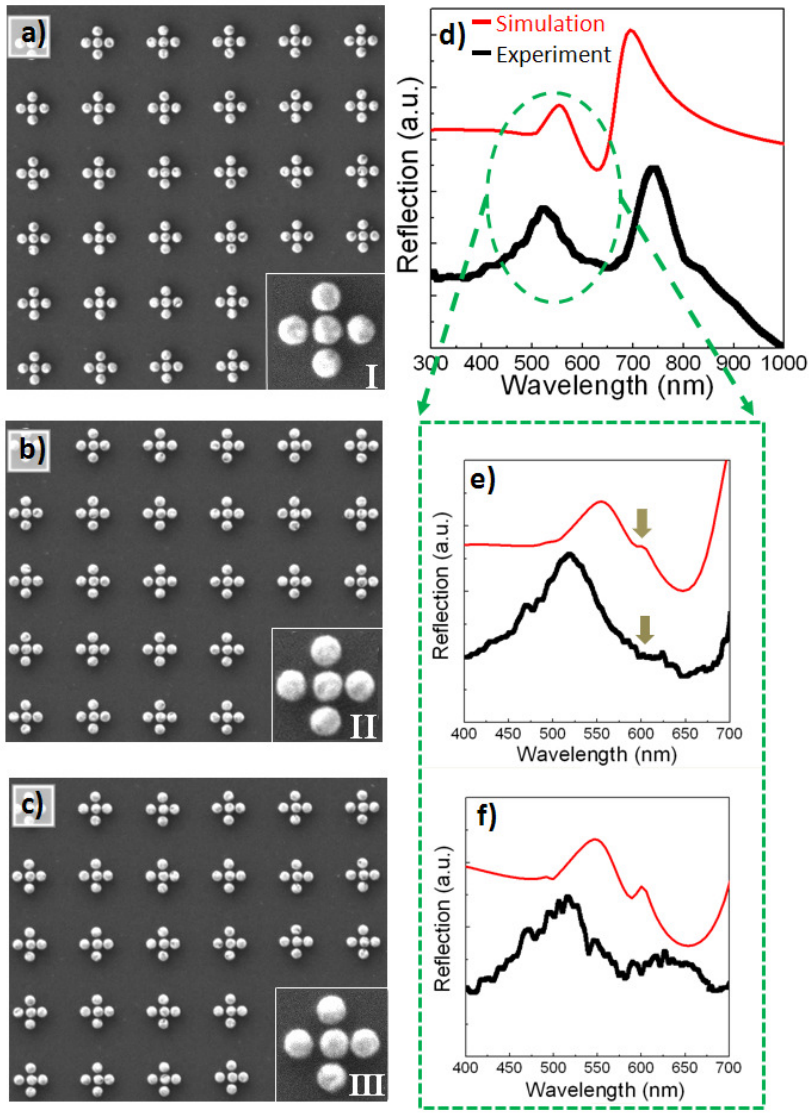

Figure 3.10 SEM images of periodic array nanopatterns of (a) the Type I symmetric pentamer, the (b) Type II and (c) Type III asymmetric pentamers. The offset of the central disk for the Type II and Type III asymmetric pentamers are 6 nm and 12 nm, respectively leading to a corresponding gap of 9 nm and 3 nm gaps. (d), (e) and (f) simulated and experimental reflection spectra of the corresponding pentamers in (a), (b) and (c). Diameter of each disk is 125 nm.

In Fig. 3.10 (d), the Fano-line shape in the reflection spectra of the Type I pentamer can be observed in good agreement between both the simulation and characterization. It was earlier shown that the symmetric pentamers reveal the superradiant mode in the

pentamers occurs when the plasmons of all the disks oscillate in phase, while the subradiant mode becomes apparent as the opposite anti-parallel dipolar moments appear. The Fano-line shape as the result of the existence of this anti-phase oscillation can be seen in the experimental reflection spectrum of the fabricated Type I pentamer at ~ 650 nm.

Interestingly the second FR in the same reflection spectrum appears when an offset is applied to the central nanodisk with respect to the other four surrounding nanodisks. Figures 3.10 (b) and (e) show the SEM images of the periodic Type II pentamers and corresponding measured and simulated reflection spectra. For the better observation of the second FR, the experimental and simulation results of the reflection spectra are shown in the wavelength range from 400 to 700 nm. A small change in the reflection spectra of the Type II pentamer can be observed in Fig. 3.10 (e) at a wavelength of ~ 600 nm, but the second FR is more obvious in the Type III pentamer, where a bigger offset of the central disk is applied. Figure 3.10 (c) shows the SEM image of the periodic pattern Type III pentamers and Fig. 3.10 (f) reveals the corresponding reflection spectra in which the second Fano-line shape appears at ~ 580 nm. These experimental results are obtained with micro UV-Visible Spectroscopy. Meanwhile, the purpose of this study is fundamental investigations to show the ability of pentamers for bi-FR exhibition. Further studies with the same direction have shown measurements with high qualities [50].

In order to study the characteristics of this second FR, the charge distributions and far-field scattering spectra are calculated. Figures 3.11 (a) and (b) show the charge distribution of the Type III pentamer at the wavelengths of 650 nm and 580 nm. 650 nm is the wavelength in which the condition of significant destructive interference between the subradiant and superradiant modes is sufficiently fulfilled and subsequently the first FR

occurs. The charge distribution shown in Fig. 3.11 (a) reveals that the Type III pentamer exhibits net anti-parallel collective dipole modes at ~ 650 nm, as long as the gap among disks exists. This plot shows the configuration of these anti-parallel modes of disks A, E and C oscillate in the opposite phase with respect to disks B and D. The ratio between the opposing phase oscillating plasmons is kept constant at 2/3 [60].

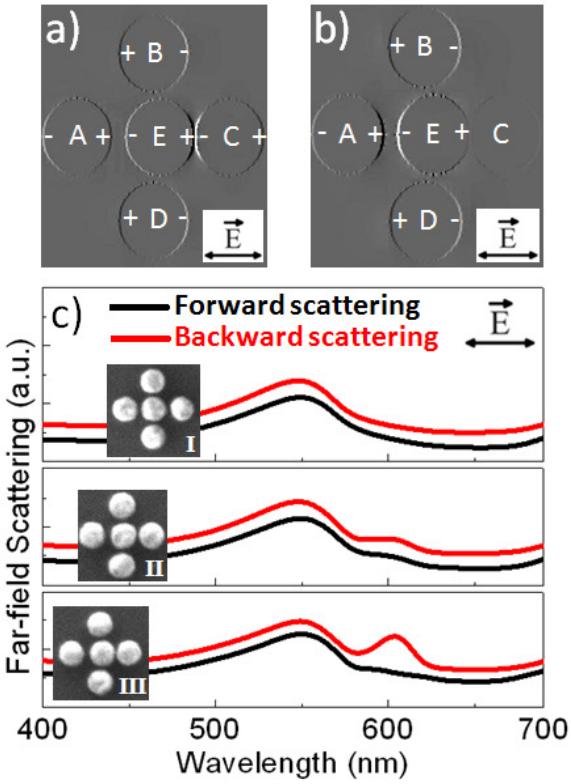

Figure 3.11 Calculated charge distribution of the Type III pentamer at the wavelengths of (a) 650 nm (b) 580 nm. (c) Calculated forward and backward far-field scattering for the Type I, II and III pentamers, respectively.

Figure 3.11 (b) shows the charge distribution of the Type III pentamer at the wavelength of 580 nm. As the plot reveals, the central disk E interacts with the disk A strongly while there is almost no interaction between the central disk E and the disk C, although the gap between disks C and E is much smaller than the gap between disks A and E. Meanwhile, disks B and D do not interact with disk E due to the further distance. Therefore,

the disk C does not exhibit any strong multipolar charge distribution with respect to the other disks. The charge intensity plotted in Fig. 3.11 (b) is comparable with recently investigated quadrumers [51] in which Fano-like interference was characterized by the narrow dip in the scattering spectrum due to the anti-parallel dipoles. In this case, the Fano minimum shows only the subradiant mode, which leads to resonant energy storage in this mode and suppression of the bright mode. It can be seen from Fig. 3.11 (b) that the net dipole moment of the pentamer unit cell is small because the dipoles of the disks A and E are oriented oppositely to the disks B and D. As a result, the scattered fields from the pentamer interfere destructively and the mode becomes subradiant. As shown previously in Fig. 3.9 (a), the superradiant mode in the pentamer totally disappears when the reflection spectrum experiences its dip [45-47] at ~ 650 nm. In other words, all disks in the pentamer should experience a net mixture of both subradiant and superradiant modes at 580 nm. But as a result of symmetry breaking in pentamers, the new dark subradiant mode happens among this mixture of subradiant and superradiant modes, leading to the appearance of the second FR.

It is well known that the subradiant mode exhibits extremely high sensitivity to the incident light, where small variations in its wavelength can change far-field forward and backward scattering spectra differently [207, 208]. Figure 3.11 (c) shows the calculated far-field backward and forward scattering profiles for the Types I, II and III pentamers, respectively. It can be explained by using Mie solution [209]. The spectra were calculated at precisely 0 and 180 degrees with respect to the wave vector which is perpendicular to the substrate. After applying the offset of the central disk position, the backward far-field scattering is amplified while the forward far-field scattering does not experience a big difference. This trend can be observed clearly in the far-field scattering spectrum from 580

nm to 650 nm. In this range, the destructive interference between the forward and the backward scattering occurs because of the high angular sensitivity of the scattered light as the result of the existence of an asymmetrical condition. The effect of the offset induces a small change in the forward and backward scattering spectra at the wavelength of 580 nm for the Type II pentamer and subsequently more obvious for the Type III pentamer. It demonstrates that the existence of this new dark subradiant mode gives rise to the second Fano interference at ~ 580 nm. Keeping in mind that symmetry breaking in pentamers leads to the emergence of the second FR only with x-polarized light and the optical properties of asymmetric pentamers are polarization-dependent unlike the symmetric pentamers which are polarization-independent.

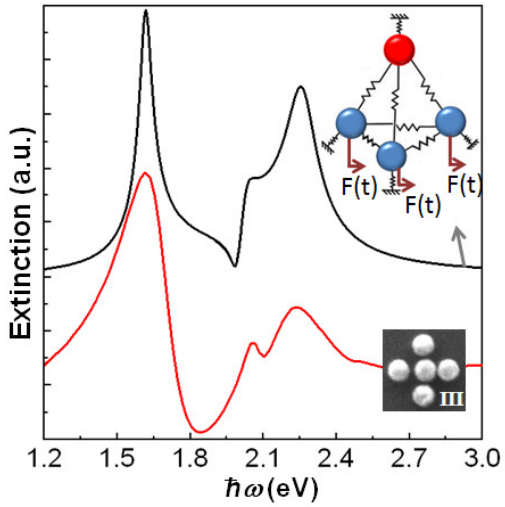

Figure 3. 12 Simulated FDTD (red line) and oscillator model calculated (black line) extinction spectra for pentamer Type III.

The analogy between the optical responses of asymmetric pentamer and the mass-spring model is one more way to proof the existence of the second FR in plasmonic systems. Figure 3.12 shows the comparison between the extinction spectrum of pentamer Type III, simulated by Lumerical FDTD at x-polarized normal incidence and power extinction of the oscillator system calculated by motion equations of 4 coupled interacting oscillator model.

This model is a simplified model of mass-spring model consisting of five coupled interacting oscillators, which can reproduce optical responses of the pentamer Type III. The simplified 3 coupled interacting oscillators model has been used to demonstrate the emergence of the first FR in symmetric pentamers recently. Similar coupling among disks A and C with respect to disk E, as well as disks B and D with respect to disk E in symmetric pentamers, allowed that system to be simplified from 5 oscillators to 3 oscillators [47]. However in the pentamers Type II and III, the coupling among disks A and C with respect to disk E are different because of different inter-disks distances. However the interaction among disks B and D with respect to disk E are still similar. Thus 4 interacting oscillators are established for mass-spring modeling. In this system 3 blue oscillators represent 4 outer disks in analogous asymmetric pentamers and red oscillator represents the central disk. Since the surrounding disks are responsible for bright mode exhibition in such optical systems, all blue oscillators are driven by harmonic force F(t). The good agreement between the mass-spring calculated and FDTD simulated extinction spectra shown in Fig. 3.12 demonstrates the clearly hybridized plasmon modes attributing to the twin FRs appearance in both systems [60].

3.8. Summary

In summary, it was shown that modulation in the ratio of anti-parallel dipole modes leads to a higher contrast of FR. The FR was obtained under normal incident light along all orientations of polarization. It was demonstrated that the monomers and the ring-like quadrumers behave the same as the isolated nanodisks exhibiting only the isolated dipole mode. After the addition of the central disk into the center of the quadrumers to form the pentamers, an anti-parallel coupling of dipolar modes appears. The ratio between anti-parallel and parallel dipole modes is 2/3 which results in the generation of a pronounced FR

as compared to the other planar symmetric oligomers. Meanwhile, the effects of elements` size and gaps among them were studied for 6 different types of pentamers.

Furthermore, it was shown that the extinction spectra of pentamers can be associated to different degrees of interference strength of eigen-modes of two nanodisks subgroups. Based on this observation, the spectral response can be analyzed and designed by changing the particle shape of either subgroup separately or simultaneously, thereby offering a powerful and flexible method to control the resonance lineshape systematically without invoking a change of particle size, inter-particle distance or the number of elements of the oligomers.

Another finding was that, once the gap among components was entirely filled, although the signature of FR vanishes, the results of the monolith rotor-shaped structures exhibited polarization-independent far-field properties. This finding was used to design and fabricate hybrid oligomers, consisting of rotor-shaped central elements and surrounding circular elements with polarization-independent far-field properties. Meanwhile, it was investigated that the oligomers possess a strong capability to exhibit multi-FRs. It has been shown that by applying an offset to the central disk in pentamers, an additional FR occurs while the first FR exists. The measured distinct spectral features in high-quality fabricated nanostructures at a precisely controlled gap down to 3 nm were in good agreement with the simulation.

Chapter 4.

Far-field optical properties of quadrumers

In Chapter 3, it was shown that reduction in the number of satellite elements from 8 in nonamers [195] and 6 in heptamers [45, 46, 54] to 4 in pentamers [47, 60] results in new sets of optical properties. In this chapter, the influence of further reduction in the number of surrounding elements to 3 is studied. Arrays of planar symmetric gold quadrumers consisting of a central nanodisk surrounded by three satellite nanodisks are designed, fabricated and studied in this chapter. Apart from a pronounced FR which is a result of high ratio anti-parallel dipole mode among plasmons arising from the central nanodisk versus three surrounding nanodisks, the geometry of quadrumers which belongs to D_{3h} point group, provides an analogues between the hybridization of the plasmons arising from each individual nanodisk in quadrumers and the same form of molecular orbital interactions from individual atomic orbital in trigonal molecules [46]. Consequently, the study on collective modes in the plasmonic quadrumer can provide more information on the complex electronic states in trigonal planar molecules. This analogy cannot be considered in other oligomers since atoms in molecular configurations with more than 3 outer atoms are not co-planar. Meanwhile, optical response of the quadrumer is modeled with mechanical coupled oscillators. It can further assist the understanding of the analogy between the plasmons in nanostructures and atomic and molecular wave functions. Effects of variation in the structural geometries of quadrumer such as elements' size and gap as well as gap filling among the elements, is also studied in this chapter. Decoding of individual contributing subgroups of quadrumers to form the spectral shape of resonances is investigated, as well.

4.1. Analogy to molecular configurations

The study on artificial molecules with different combinations and arrangements has been experimentally undertaken recently [210, 211]. The coupling mechanism of each individual

atom with the nearby atoms making up the molecules, is the key to predict the molecular characteristics [46]. Out of several analogues coupling mechanisms among the components of the nanostructures, plasmon coupling is a topic of intense current interest [21]. It is well known that the near-field associated at plasmonic resonance of the individual particles extends some distances away from it. Closely packed nanoparticle interact each other, mediated by this near-field. One advantage of oligomers is that such structures can be regarded as highly tunable artificial molecules [210]. This interaction is in direct analogy to molecular physics and the formation of molecules due to the overlap and interaction of the electronic orbitals of the individual atoms rather than plasmonic near-field [46, 48, 212].

The qualitative for unraveling the energy levels of the molecular orbitals in conjugated hydrocarbon molecules in benzene is one of well-studied analogues by plasmonic oligomers [46, 212]. In analogy to a benzene molecule, the structure of the plasmonic hexamer consisting of 6 ring-type nanoparticles was used [46]. It belongs to the D_{6h} point group, which exhibits a high spatial symmetry and the collective modes with finite in-plane dipole moments belong to the E_{1u} irreducible representation. As it was demonstrated earlier, a remarkable change of its resonant behavior can be seen when a central nanoparticle is introduced. This capability encourages researchers to predict the characteristics of corresponding molecules with the same configurations. As another example for analogy among planar oligomers and biochemical molecules, Liu et al. examined the magnetic plasmons of fused ring structures consisting of multiple connected heptamer units [212]. They found that in a two-unit heptamer structure, the magnetic mode consists of two opposite current loops and leads to the emergence of an anti-phase behavior of the

magnetic plasmons. The plasmon supported by this structure can be regarded as the plasmonic analogue to a naphthalene molecule [212].

One should be noticed that in analogy between planar oligomers and multigonal molecules, oligomers` components are co-planar while multigonal molecules are typically non-co-planar. It is due to the tendency of the surrounding atoms to achieve the maximum distance with respect to each other under a 3D configuration so as to provide the lowest energy for molecules in the stable state. CH_4 and PCl_5 are good examples of pentagonal and hexagonal molecules, in which the central atom and the surrounding atoms are not placed in the same plane. But trigonal planar molecules, such as BF_3, SO_3 and BCl_3 possess co-planar central and surrounding atoms. Therefore plasmonic quadrumers, composed of three similar nanodisks belonging to the D_{3h} point group, are perfect candidates for analogy to trigonal planar molecules [48, 49, 57].

In this section, the designed and fabricated arrays of planar symmetric quadrumers consisting of a central nanodisk and three outer ring-like nanodisks, which have D_{3h} spatial symmetry, are studied [48]. This geometry can be an analogue between the hybridization of the plasmons arising from each individual nanodisk in quadrumers and the same form of molecular orbital interactions from individual atomic orbital in molecules belonging to D_{3h} point group. It can provide more information on the complex electronic states [46] in trigonal planar molecules. The recent investigation on plasmon modes in three nanocylinder clusters was also related to irreducible representations of point group D_{3h} [213]. The difference between the mentioned paper and our work is the existence of the central cylinder or disk. The plasmon interaction nature, among the central nanodisk with the surrounding ones in our configuration, promises to predict and understand the electronic

states in trigonal planar molecules, which have similar configurations, such as BF_3, SO_3 and BCl_3.

A detailed study of plasmonic quadrumers is presented in which the near-field interaction among neighboring elements determines its optical response. A pronounced FR is observed experimentally and predicted theoretically. This resulting FR is attributed to the destructive interference among anti-parallel dipole modes which can be observed independently of the excitation polarization at normal incident light.

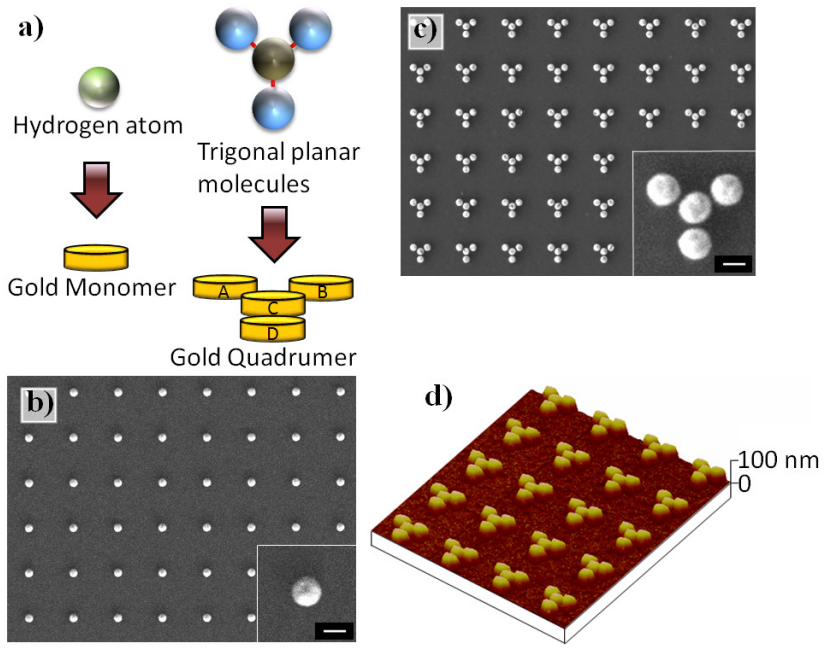

Figure 4.1 (a) (Upper row) Illustrations of the molecular geometries of an H atom and the trigonal planar molecule configuration. (bottom row) Their plasmonic analogues, a gold monomer and a gold quadrumer. SEM images of periodic array patterns of (b) monomers and (c) quadrumers. Scale bar is 100 nm. (d) AFM image of quadrumers.

Figure 4.1 (a) illustrates the molecular geometries of an H atom and planar trigonal molecules, and subsequently a gold monomer and a gold planar quadrumer formed as their plasmonic analogues, respectively. The formation of artificial molecules draws on the

compelling analogy to the formation of molecules in chemistry. Figures 4.1 (b) and (c) show the SEM images of the periodic patterns of the monomers and quadrumers fabricated on the silicon substrates and Fig. 4.1 (d) plots the AFM image of the quadrumer. The sizes and array configurations of the monomers were the same as those in the quadrumer array for the comparison and further analyses. The diameter and height of the nanodisks are 142 nm and 60 nm and the gap between the nanodisks in the quadrumers is 18 nm. Significant efforts have been made to fabricate circular nanodisks in our experiments to avoid perturbation in the arising plasmons which are extremely sensitive to the shapes of the nanostructures.

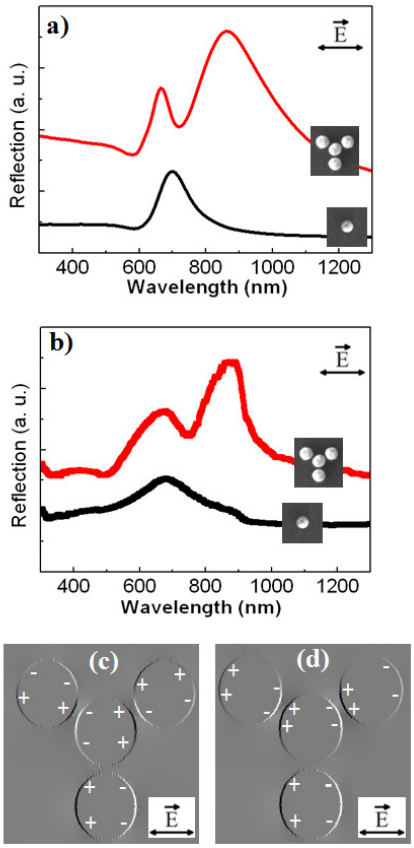

Figure 4.2 (a) Simulated and (b) measured reflection spectra of the monomers and quadrumers at x-polarized normal incidence. Calculated charge distribution of the quadrumer at a wavelength of (c) 740 nm and (d) 880 nm by FDTD simulation.

In order to investigate the hybridization among the nanodisks, the optical reflection responses of the plasmonic monomers and quadrumers were simulated as shown in Fig. 4.2(a). The measured reflection spectra (Via micro UV-Visible spectroscopy) are displayed in Fig. 4.2 (b). It is apparent that the spectral profiles in Fig. 4.2 (b) display the same characteristics as those simulated in Fig. 4.2 (a). The reflection spectra of the Au monomers reveal the excitation of the dipolar mode which attributes to emergence of a single resonance. But hybridizing feature in the spectrum appears when three nanodisks are symmetrically placed in close proximity to the monomer, which functions as the central nanodisk. In this case, the mixed plasmons of the nanodisks hybridize and increase the chance to form anti-bonding and bonding plasmonics mode [214] transition. It is in direct analogy to the electron wave functions of atoms involving in trigonal planar molecules, which belong to the D_{3h} point group [48].

The interaction of light and this gold quadrumer leads to the excitation of collective plasmons in the nanodisks. The net anti-parallel dipolar plasmon, arising from individual disks, hybridizes destructively, allowing the formation of a subradiant collective mode in addition to the superradiant collective mode [110]. Consequently FR asymmetric line-shape profile is around 740 nm as well. The existence of the FR in the quadrumers demonstrates that the condition of the destructive interference between the subradiant mode and the superradiant mode is sufficiently fulfilled. It is worthwhile mentioning that although the obtained FR shown in Figs. 4.2 (a) and (b) is under x-polarized incident light, the reflection spectra for the other polarization directions are identical, as being expected from the symmetry considerations [52]. It happens because the destructive interference in such structures is a result of interference among plasmons arising from each individual

component as well as gaps among them, whose scales are not comparable with the incoming light wavelength. That is why the quadrumer can be considered as an in-plane isotropic structure, in which the FR is achieved under totally symmetric condition at normal incidence and also independent of the excitation polarization.

In order to elucidate the physics behind the appearance of subradiant mode and superradiant mode, charge distributions at the respective simulated spectral positions of 740 nm and 880 nm are shown in Figs. 4.2 (c) and (d), respectively. These plots are calculated for x-polarized incident light, keeping in mind that due to the planar symmetry of quadrumers, the excitation polarization does not affect the optical response and it only leads to the rotation of charge distribution pattern in all nanodisks simultaneously.

The charge distribution pattern in a single quadrumer at a wavelength of 740 nm plotted in Fig. 4.2 (c) shows the configuration of the anti-parallel dipole, which is responsible for the emergence of the subradiant mode. Although the disks A and B exhibit rotated charge distribution pattern with respect to the central nanodisk C (see illustration in Fig. 4.1), the total oscillation directions of the mentioned two nanodisks are parallel to the oscillation direction of the nanodisk D. In other words, at this wavelength the dipole moments of the nanodisks A and B only boost the dipole moment of the nanodisk D, while the central nanodisk C oscillates totally out of phase. This central disk exhibits an anti-parallel dipole with respect to the total dipole moment of the other three nanodisks. Unlike this mode, the superradiant bright mode in the quadrumers exists when the plasmons of all the four nanodisks oscillate in the same phase.

The charge distribution pattern at a wavelength of 880 nm plotted in Fig. 4.2(d) represents the formation of the superradiant mode. In this case, all the nanodisks within the quadrumer structure experience strong coupling and form collective plasmonic mode. It is the wavelength in which the effect of the destructive interference decays totally. This destructive interference is also observed experimentally in reflection measurement in Fig. 4.2 (b) where the FR becomes excited at around 740 nm. This plasmon hybridization in quadrumers can be used to express transformation among atoms with D_{3h} symmetry. It could be applied in an analogous manner to the molecular orbital theory [211] of trigonal planar molecules.

4.2. Mass-spring analogy

Optical response of the quadrumer is modeled with mechanical coupled oscillators to have better understanding of the analogy between the plasmons in nanostructures and atomic and molecular wave functions. The quadrumer plasmonic system can be modeled by a three coupled interacting oscillators system, which is shown in Fig. 4.3 (a). This physical model is an extension of the classical two oscillators system which was used to study the nature of FR [69]. Our model is the simplified form from the 3D system consisting of four interacting oscillators to 1D oscillator models, which is shown in Fig 4.3 (a). Similar to section 3.2 the simplification is based on two assumptions: firstly, the plasmons of the surrounding nanodisks do not interact each other unlike their individual interaction with the central nanodisk. Meanwhile, in all polarization excitations, two out of the three surrounding nanodisks have got totally similar interaction with the central nanodisk. The oscillator 2 in the model shown in Fig. 4.3 (a) represents these two disks. Meanwhile, the interaction of the third nanodisk with the central nanodisk is different. Then the oscillator 3 represents the

third surrounding nanodisk. Eventually the oscillator 1 is assumed as the representive of the central disk [48].

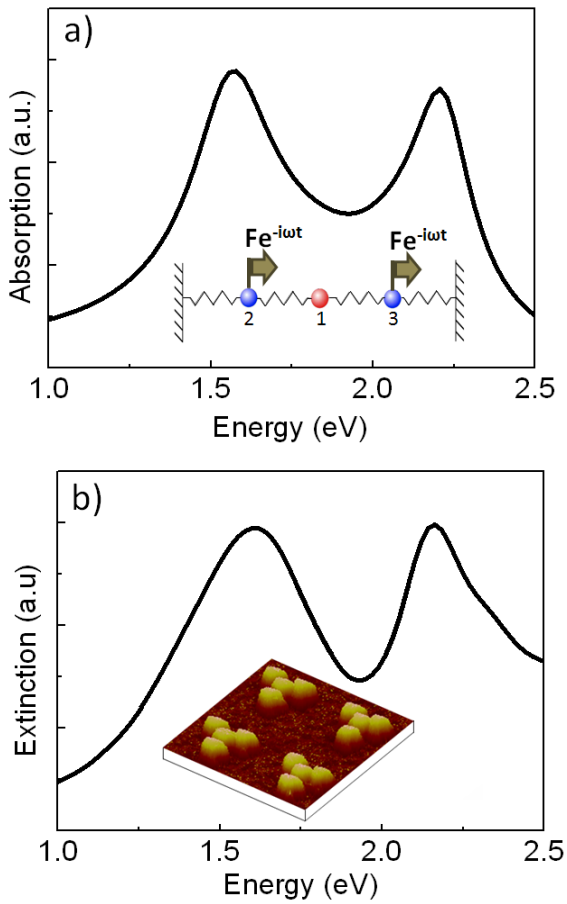

Figure 4.3 (a) Three coupled interacting oscillators representing the quadrumer optical responses and corresponding calculated power absorption, and (b) simulated extinction spectra of the quadrumer at x-polarized normal incidence by FDTD.

In the planar symmetric oligomers including the central nanodisk or particle, a subradiant mode exists when a nanodisk or particle is added to the center of surrounding ring-like nanodisks or particles [45, 46]. It means in the optical system, in the absence of central nanodisk or particle only bright mode can be excited. Subsequently in our mechanical system, only the oscillators |2> and |3> are driven by a periodic harmonic force

F(t)= **F**$e^{-i\omega t}$ due to their responsibility for the appearance of bright mode. This is analogous to optical excitation of the superradiant mode.

The equations of motion of oscillators |1>, |2> and |3>, are solved in terms of the displacements x_1, x_2 and x_3 from their respective equilibrium positions as was stated in Eqs. (3.1) to (3.3) in section 3.2. The quadrumer bright plasmon mode is modeled with ω_2 = 1.9 eV and ω_3 =2 eV as the representives of resonance frequencies of three surrounding disks and resonance frequency ω_1 =1.9 eV which represents the central nano-disk frequency. By tuning the coupling between modes (Ω^2= 0.9) and other parameters (γ_1 =2 E-1, γ_2 =4E-1, γ_3 =5E-2 and F=1.5), the absorption power of the oscillator system is calculated and sketched in Fig. 4(a). This is an analogue to the optical excitation which reproduces the plasmon response of the quadrumer. Figure 4.3 (b) shows the extinction spectra by FDTD simulation at x-polarized normal incidence. Absorbed powers of the oscillator system calculated by Eq. (3.1) to (3.3) and the FDTD simulated extinction are in good agreement. The dip position of the both absorption profiles in the mechanical model of Fig. 4(a) and extinction profile in the simulation result in Fig. 4.3 (b) is around 1.9 eV which is the position of destructive interference among plasmons arising from nanodisks.

4.3. Geometrical influence

In this section, it is shown that nanodisk dimensions and the gaps among them affect the optical properties of quadrumers, similarly to other oligomers [61]. Table 4.1 list out the dimensions and sizes of 4 different sets of quadrumers. Similar to the trend which was established for pentamers to choose the gap and size in section 3.4, for the case of quadrumers, we also choose 2 quadrumer sets with same disks` diameter and different gaps.

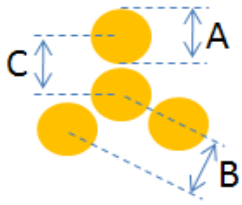

	I	II	III	IV
A	130	130	110	110
B	160	140	160	140
C	160	140	160	140

Table 4.1 Dimensions (nm) of 4 various types of quadrumers

Transmission spectra of each set is simulated and shown in Fig. 4.4. It helps to determine the wavelength in which the destructive interference vanishes and the structure resumes to exhibit plasmons constructively. This figure reveals that in quadrumers, the gap size among the disks plays a more important role than the disk size in terms of amplitude and full width at half maximum of Fano-like shape spectra, as well. As can be seen, the quadrumers Types I and II exhibit different asymmetric Fano-shape spectra while the diameters of elements are similar but the gaps are different. The similar trend can be seen in the quadrumers Types III and IV. Again more pronounced FR is obtained with the quadrumer Type II with the smallest gap of 10 nm.

Meanwhile, it is found that quadrumeric geometry also allows tailoring the overall spectral profile in plasmonic nanoclusters. Previously It has been shown in nonamers [195] and pentamers [66] that the spectral shape of resonances in plasmonic quadrumers can also be decoded into two individual contributions from their subgroups. In nonamer, 2 subgroups were classified to central element and eight surrounding elements [195] and in pentamers two subgroups were: 4 outer elements and three middle ones [66].

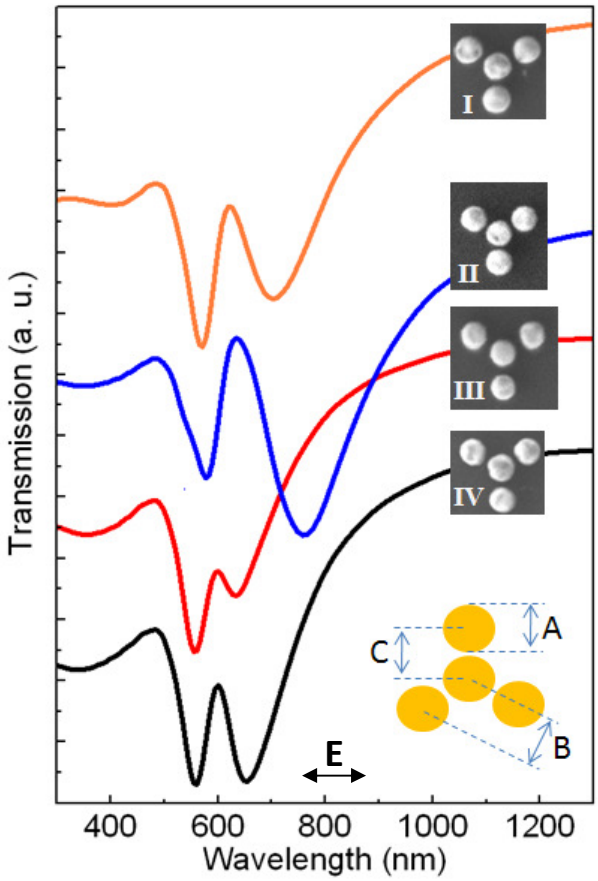

Figure 4.4 Simulated transmission spectra of 6 various types of pentamers at x-polarized normal incidence.

Figure 4.5 shows detailed optical properties of an array of quadrumers consisting of 140 nm diameter circular-shaped disks with 20 nm inter-particle distances. Figures 4.5 (a) and (b) show the simulated (black line) and the measured extinction (via FTIR) spectrum in good agreement. Both spectra are dominated by a remarkable Fano dip, akin to previous investigations of quadrumers in this chapter. As can be seen, two dominant peaks in Fig. 4.5 (b) seem to be well described by two separate resonances given by two subgroups (see Fig. 4.5 (c)). This observation is further confirmed by calculating the electric field intensity distribution in the quadrumer at the two peak wavelengths. The left panel of Fig. 4.5 (d) clearly demonstrates that at the first peak position, three outer disks are efficiently excited, inducing strong field enhancements around each particle while the central disk is relatively

dark. Such a selective excitation of different particles is even more pronounced at the second peak position where the three upper disks become dominant, leaving the other two disks in the top and bottom completely dark. As can be noticed for quadrumer case, the fitting between subgroups is much better than the nonamers and pentamers with their subgroups.

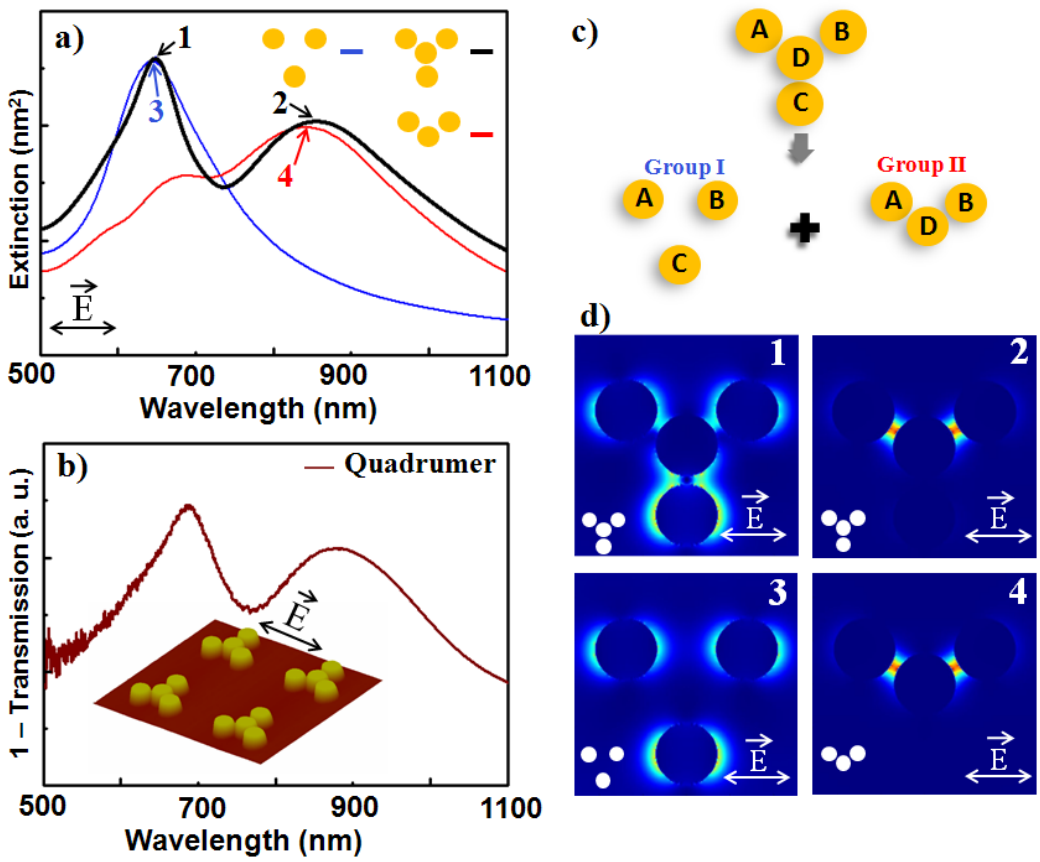

Figure 4.5 (a) Simulated extinction spectra of an individual quadrumer (black curve) and the two subgroups (blue and red curves). (b) Measured extinction (1-Transmission) spectrum of the quadrumer array at normal incidence. The inset shows a 3D AFM image of the quadrumers and the incident polarization. (c) Sketch of decomposing a quadrumer into Groups I and II. (d) Electric field intensity distribution in the pentamer at peaks 1 and 2 and in the two subgroups at their respective scattering peaks 3 and 4. (Adapted with permission from Ref. [66], ©2012, American Chemical Society.)

Based on these observations, we propose that the complex optical excitation in the whole quadrumer structure can be decomposed into two separate contributions from its

subgroups. Group I is composed of the outer three disks and group II of the upper three disks (see Fig. 4.5(c)). Comparison between extinction spectra of two separate subgroups (blue and red lines in Fig. 4.5 (a)) with the extinction of the full nanostructure (black line in Fig. 4.5 (a)) which are plotted in the same units, possess almost perfect overlap in terms of both the position and amplitude of resonances. It shows that that the overall spectral response of the quadrumer is due to the interaction of the separate excitations of the subgroups at different wavelengths. Meanwhile, the electric near-field distribution of each subgroup at the peak frequencies is similar to that obtained for the complete nanocluster (see Fig. 4.5 (d)), confirming the decomposition assumption.

Like pentamers` decomposition recipe shown in sections 3.4 and 3.5, finding the quadrumer subgroups which were shown in Fig. 4.5 (c), is highly useful to deign FR signature. If we change the central particle shape, indeed, we modify only the optical property of group II, i.e. only the second resonance (red curve Fig. 4.5 (a)) but leaving the first one unmodified (blue curve Fig. 4.5 (a)). Also we can change for example only the external nanoparticles, modifying both groups in this way. Those situations are shown in Fig. 4.6. By changing the shape of the nanoparticle but keeping the particle size and inter-particle distance as constants, a flexible remodeling of the overall spectral shape can be obtained, manifested by a systematic variation in the relative height of the two peaks as well as the resonance linewidth of the spectral dip.

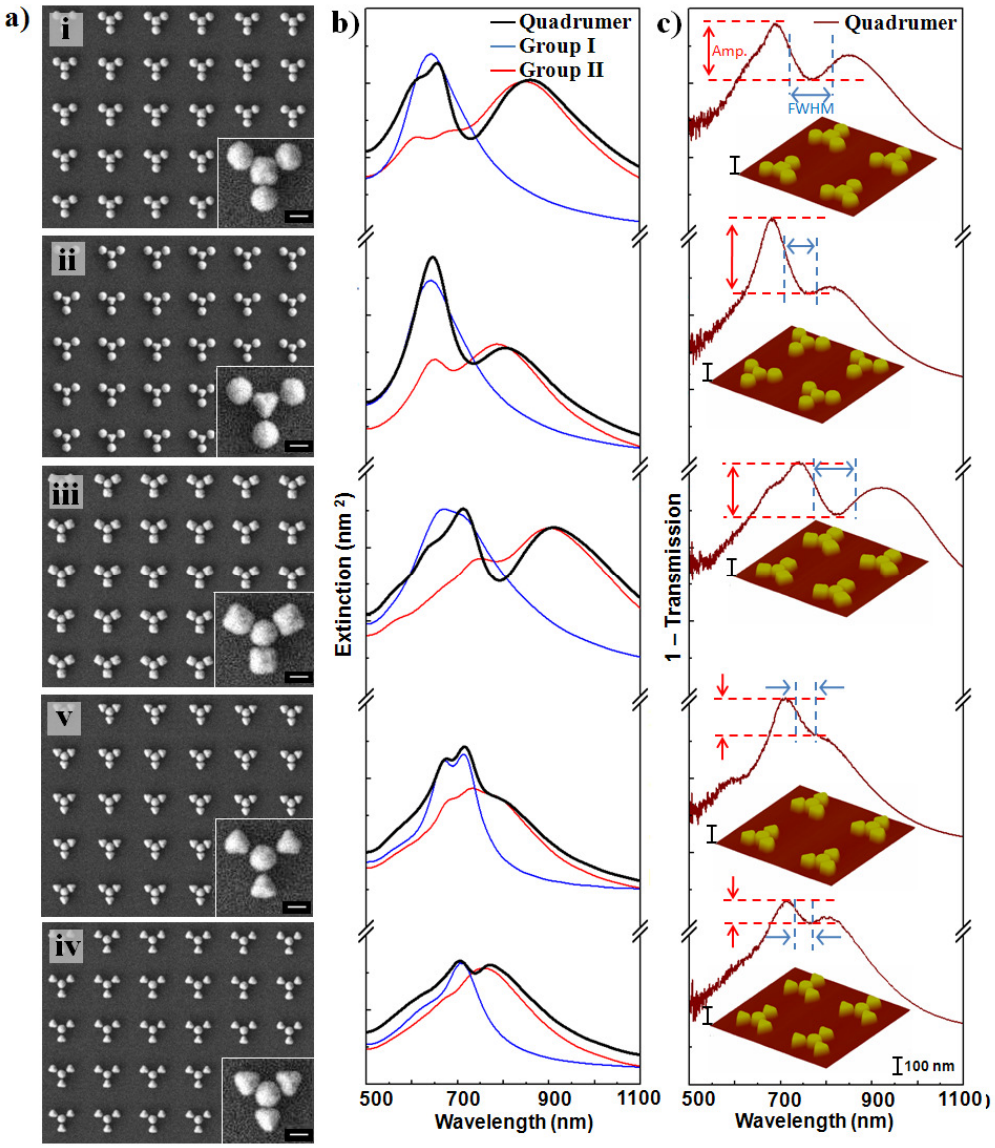

Figure 4.6 Tuning of resonance linewidth and spectral contrast of plasmon resonances in different quadrumers. (a) SEM images of hybrid quadrumers consisting of differently-shaped elements. The scale bar in each image is 100 nm. (b) Simulated extinction spectra for the pentamers (black curve) and their two subgroups (blue and red curves). (c) Measured extinction spectra for the same pentamers at normal incidence, along with 3D AFM images of the nanostructures. (Adapted with permission from Ref. [66], ©2012, American Chemical Society.)

More specifically, replacing the central circularly-shaped disk of the quadrumer shown in Fig. 4.5 with a square- or triangle-shape nanodisk allows for significant tuning of the peak-dip contrast and the resonance full width at half maximum (FWHM) (see the first two cases in Fig. 4.6), which are two crucial parameters to realize high resolution plasmonic biosensors.

More pronounced modification of the spectral profile can be obtained by changing the particle shape of the outer four disks in the quadrumer (see the last three cases in Fig. 4.6) because the spectral response of both subgroups is altered in this way.

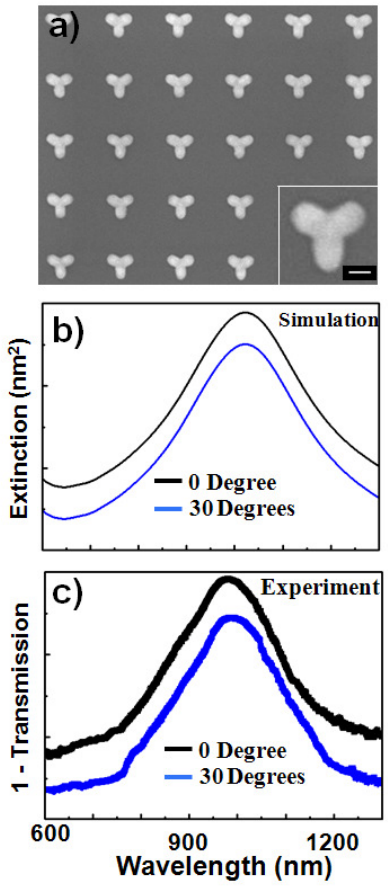

Figure 4.7 (a) SEM images of 120° symmetric rotor-shaped nanostructures, (b) simulated and (c) experimental extinction spectra of the corresponding structures in (a) at indicated polarization excitation with respect to x-axis. Scale bar is 100 nm.

Furthermore, similar to pentamers, far-field optical properties of quadrumers with filled gap is polarization-independent, as well. It is shown that once the gap among the components is completely filled, resulted monolith rotor-shaped structure still exhibit isotropic SPR. Figure 4.7 shows that the optical properties of 120° symmetric rotor-shaped nanostructures are polarization-independent (isotropic). SEM images of designed and

fabricated arrays of symmetric rotor-shaped nanostructures accompanied by corresponding simulation and experimental Extinction (1 – Transmission) spectra are shown in Fig. 4.7. The diameter and height of each individual nanorotor are 350 nm and 60 nm, respectively. The polarization independent optical properties can be seen clearly in the both simulated and experimental results.

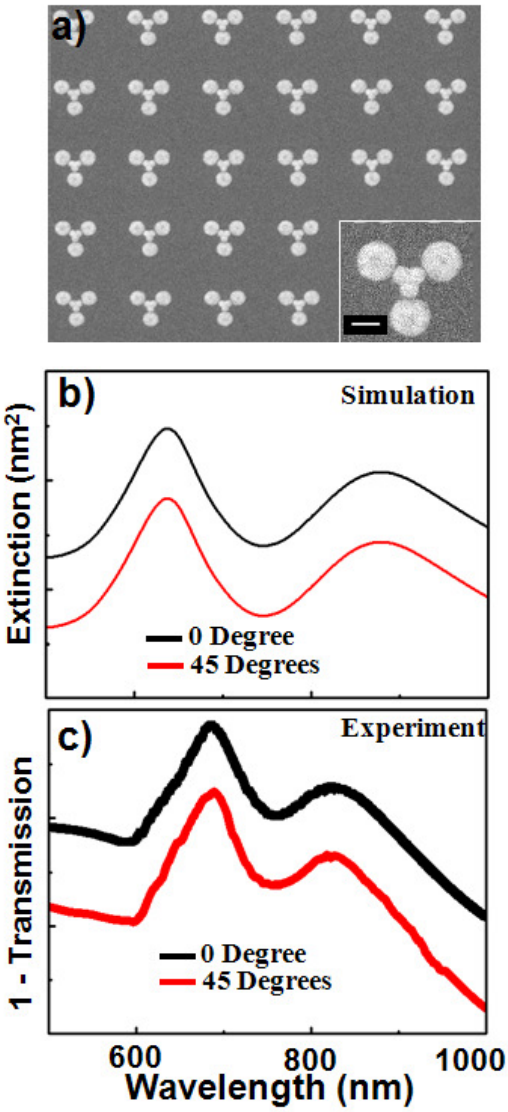

Figure 4.8 (a) SEM images of designed hybrid quadrumers, (b) simulated and (c) experimental extinction spectra of the corresponding structures in (a) at indicated polarization excitation with respect to x-axis. Scale bar is 100 nm

Consequently, the central element of regular oligomers is replaced by rotor-shaped structures. In fact this hybrid structure is a result of the combination of regular quadrumers

consisting of all circular components and rotor shaped structures which are both isotropic. Therefore the resulting hybrid quadrumers are proved to exhibit far-field optical properties independently of polarization excitation as well. Figure 4.8 (a) shows the designed and fabricated arrays of hybrid pentamers as well as corresponding simulated and experimental extinction spectra with good agreement. The spectra reveal that the combination of the isotropic rotor-shaped nanostructures and the isotropic oligomers still leads to the exhibition of the isotropic pronounced FRs at ~ 760 nm. Near-field properties of oligomers and subsequently such hybrid oligomers will be studied in detail in Chapter 5.

4.4. Summary

Far-field optical responses of the designed and fabricated plasmonic quadrumers were studied theoretically and experimentally in this chapter. It was shown that further reduction in the number of surrounding satellite elements from 8 in nonamer, 6 in heptamer and 4 in pentamers, to 3 in quadrumers leads to the ratio of 1/3 among anti-parallel dipole modes. It attributes to a pronounced FR at normal incident light and independent of the excitation polarization. Meanwhile, the experimental results, the FDTD simulations and mass-springs model simulation are in good agreement.

The fabricated quadrumer provides an opportunity to draw inspiration to design artificial trigonal molecules, which can lead to the discovery of numerous useful electromagnetic analogues of chemical molecules in plasmonics. Particularly it can provide the opportunity for the better understanding of the molecular orbital theory of the planar trigonal molecules, where the plasmons of neighboring structures or surfaces interact each other. Therefore, the plasmons mix and hybridize just like the electron wave functions in

similar atomic and molecular orbitals. Meanwhile, spectral response of quadrumers was decoded to 2 separate subgroups, thereby offering a powerful and flexible method to control the resonance lineshape systematically. Furthermore, optical properties of monolith rotor-shaped 120 ^{0} nanostructures as well as hybrid quadrumers consisting of rotor-shaped central elements and surrounding circular elements, were shown to have polarization-independent characteristics.

Chapter 5.

Near-field optical properties of oligomers: Energy localization

In chapters 3 and 4 far-field optical properties of oligomers were studied in detail. It was shown that reduction in the number of surrounding components of oligomers gives rise to higher ratio of anti-parallel dipole modes resulting in higher contrast of FR in far-field responses. In this chapter it is shown that this reduction in the components quantities provides more promising applications not only in far-field responses but also in near-field responses. It is known that all oligomers have the capability to enhance localized near-field energies known as hot-spots in nanoscale gaps among the components. But these hot-spots in regular oligomers can be excited inside all gaps including the gaps among outer elements and central one as well as the gaps among neighboring outer elements. We found that near-field energy in oligomers with the fewer number of satellite elements such as pentamers and quadrumers, take place only among the surrounding disks and the central one. This characteristic provides the capability to localize and tune the hot-spots among the subdiffraction length scale gaps via polarization orientation as an efficient tool. It is worth noting that the tuning of light spatial distribution can be achieved by only a single source, instead of applying a phase shift in a co-illumination system [87, 196]. It provides a number of potential applications in nanolithography [197], nonlinear spectroscopy [196], optical information processing such as optical modeling and switching [215] and other research fields in which optical investigations are carried out with a high spatial resolution.

Furthermore in this chapter, a comprehensive extensional study on the effect of nanodisk sizes and the gap among them on the near-field optical properties of pentamers and quadrumer is presented. Moreover, it is found that some defects, such as symmetry breaking can also lead to novel near-field energy distributions. Finally, the near-field energy characteristics in a novel type of hybrid pentamers, consisting of the rotor-shaped central

elements, are investigated. It is shown that these hybrid oligomers can enhance the near-field energy intensity and localization of planar oligomers significantly while the net optical properties of the system are still kept isotropic.

5.1. Near-field localization

Localized near-field energy known as hot-spots are studied in nonamers [195] and heptamers [46, 56] in details. It is shown that based on the frequency and polarization direction of incident light, hot spots in such structures take place in some of the gaps among central component and satellite components as well as some hot-spots among the satellite components. One advantage of pentamers and quadrumers as compared to oligomers with higher number of surrounding elements is the unique potential for the localization of near-field energy intensities. In pentamers and quadrumers, the outer satellite elements are sufficiently far from each other. Therefore, in certain frequency window, hot-spots can be localized only among the central component and outer elements. Figures 5.1 (a) to (c) show the calculated near-field energy localization plots in pentamers under consideration in section 3.1 at various polarized illuminations at a wavelength of 880 nm. It is the wavelength of the second extinction peak (transmission dip) at which destructive interference vanishes and all elements oscillate in phase. The field intensities show hundreds-fold enhancement inside the gaps, revealing that these separated disks can be used as an optical antenna. These plots demonstrate that the field can be strongly localized in the right and left gaps at x-polarized excitation, in the top and bottom gaps at y-polarized excitation and in all four gaps at a 45-degree polarization. It is the unique feature of the pentamers to store light energy at different positions selectively by changing the polarization. This ability to concentrate light energy in different positions by changing the polarization is a unique

feature of pentamers which can make them as good candidates for various applications on the optical switching and nonlinear spectroscopy.

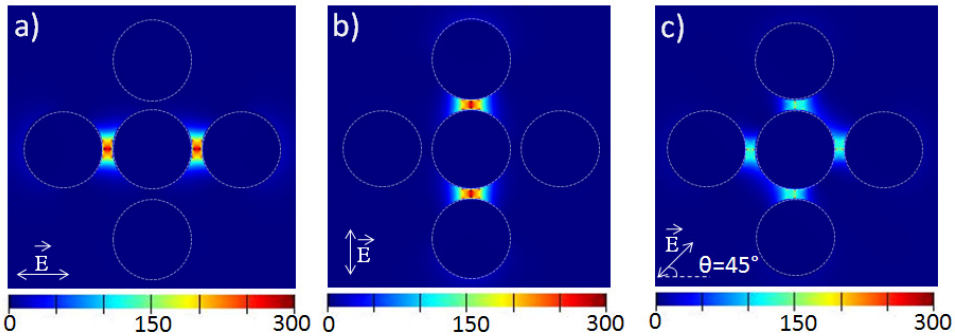

Figure 5.1 Calculated electric field distributions at x-polarized normal incidence at a wavelengths of 880 nm and at (a) x-polarized (b) y-polarized and (c) 45-degree polarized light incidence.

This ability can be seen in the quadrumers even with wider potentials. Quadrumers show to have capability to turn off one of the hot-spots, entirely. Figures 5.2 (a) ~ (c) plot the spatial energy distributions at 30^0 and 60^0 excitation polarization with respect to the *x*-axis and non-polarized incident light, respectively. The unequal nanoscale triangular localized energies shown in Fig. 3(a) can overcome the difficulties of sharp corner exposure in plasmon-lithography [197]. More interestingly, the energy localization pattern plotted in Fig 5.2 (b) shows how the quadrumer can be used as a planar optical switch [215] along the three directions, simultaneously. As can be seen, when a 60^0 excitation polarization is applied, the near field energy is localized at two gaps out of the three gaps inside the structure. The third gap exhibits almost no near-field energy. This unique ability to localize the near-field energy in the selected gaps between the nanodisks via the excitation polarization in quadrumers and pentamers provides the possibility to realize synchronized control systems in molecular nanoscale circuits [216]. Similar to pentamers, quadrumers can also witness localized near-field energy in all gaps at certain conditions. For quadrumers,

non-polarized incident light can fulfill the requirement for such patterns of near-field localization as can be seen in Fig. 5.2 (c).

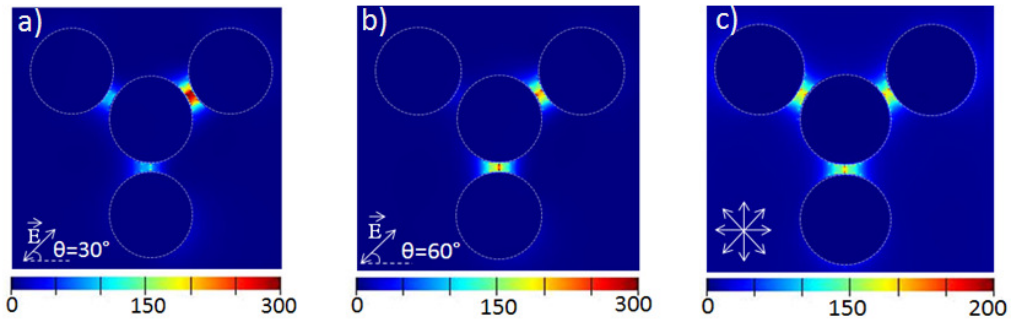

Figure 5.2 Calculated field distribution at x-polarized normal incidence at a wavelengths of 780 nm at (a) 30-degree polarized, (b) 60-degree polarized and (c) non-polarized, to normal light incidence.

5.2. Influence of geometry on the near-field energy

So far, we have demonstrated that the control of light localization with nanoplasmonics is one of the promising areas which can make metallic nanostrcutures good candidates for various applications in sensing [13]. In this section, the effects of the disk size, and the gap among the disks on the intensity and shape of this excited near-field energy "hot-spots" are studied [61]. In section 3.3, the effect of nanodisk size and the gap on the far-field optical properties of six different types of pentamers were studied [45, 46, 49]. Here, this effect on the intensity and localization of the near-field energy in such pentamers will be studied. We recall Table 3.1 in which the dimensions and sizes of 6 different sets of pentamers are listed out. The simulated transmission spectra of each set shown in section 3.5 Fig. 3.5 helps to determine the wavelength in which the destructive interference vanishes and the structure resumes to exhibit plasmons constructively which is at the position of the second dip of transmission [47]. Consequently linear and logarithm scales of field distribution for each set of pentamers are calculated and shown in Figs 5.3 (a) and (b). The vertical bars indicate the

color scale for the magnitude of the electric field intensity. The linear scale of the field distribution patterns can be used to show field intensity and the logarithm scale is useful to determine the minimum field intensity comparable to zero. This figure reveals that the gap size among the disks plays a more important role than the disk size in terms of field intensity enhancement.

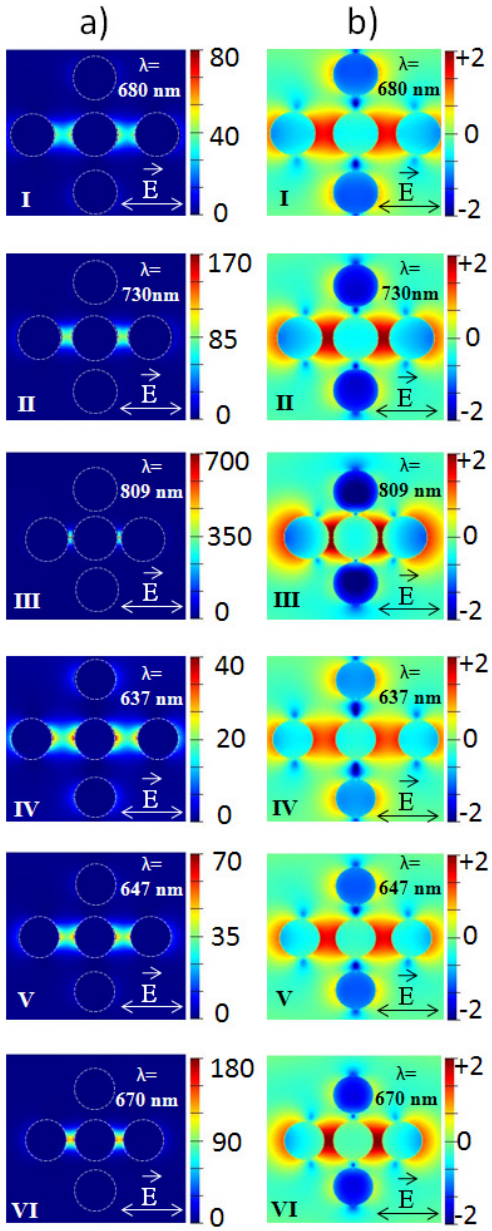

Figure 5.3 (a) Linear and (b) logarithm scales of the calculated electric field distribution within the 6 various pentamers at x-polarized normal incidence and a wavelength of the second dip in the corresponding transmission spectra of Fig. 3.5.

As can be seen, the pentamers Types I and V at a gap of 50 nm possess 80 and 70 times electric field enhancement, respectively which are comparable. The similar trend can be seen in the pentamers Types II and VI, in which though the disk sizes are different, their optical properties are similar. The gap among the disks in these two pentamers is 30 nm. The calculated optical properties for the pentamer Type IV also support this conclusion that when the gap increases, the electric field intensity decreases significantly. Finally the results of the pentamer type III show a huge increase in electric field intensity when the gap among the nanodisks decreases to 10 nm.

Moreover, the logarithm scale plot of electric field intensity reveals an interesting trend in the localization of near-field energy among the disks. While the smaller gap among the nanodisks results in higher near-field energy among three middle disks, but it attributes to a lower exhibited intensity inside the disks at the bottom and top. A comparison in the logarithm plots corresponding to pentamers Type III and IV shows this difference clearly. In pentamer Type III which possess the minimum gap feature among all pentamer types, the exhibited intensity in the disks at the top and bottom are close to zero. But in pentamer Type IV, the disks in the bottom and top exhibit much higher field intensity. It shows more contribution of three middle disks at this wavelength which is an additional proof of subgroup decomposition recipe for pentamers given in section 3.4.

The same study is established for quadrumers. We recall Table 4.1 in which the dimensions and sizes of 4 different sets of quadrumers are listed out. Again, linear and logarithm scales of field distribution for each set of quadrumers are calculated at the position of the second dip of transmission spectra shown in section 4.3, Fig. 4.4. Similar to pentamers, in this position the destructive interference vanishes and the structure resumes

to exhibit plasmons constructively [47]. Consequently, linear and logarithm scales are calculated and shown in Figs 5.4 (a) and (b). As can be seen, similar to pentamers, in quadrumers the gap size among the disks is a key point. The quadrumers Type I and IV at a gap of 30 nm possess 120 and 110 times electric field enhancement, respectively which are comparable. But a comparison between Quadrumers Type I and II reveals a significant difference in electric field intensity, while the quadrumers have similar disks size but different gaps. The same trend can be seen in the comparison between quadrumers III and IV.

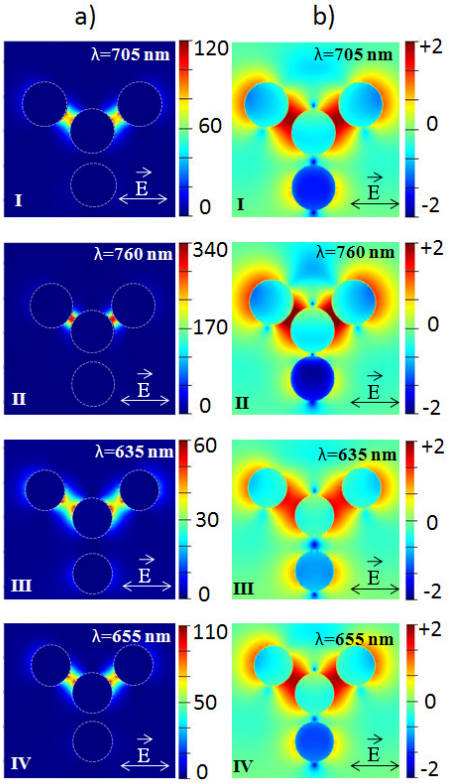

Figure 5.4 (a) Linear and (b) logarithm scales of the calculated electric field distribution within the 4 various quadrumers at x-polarized normal incidence and a wavelength of the second dip in the corresponding transmission spectra of Fig. 4.4.

Meanwhile, the logarithm scale plot of electric field intensity proves that the smaller gap among the nanodisks results in lower exhibited intensity inside the disks at the bottom.

A comparison between the logarithm plots corresponding to quadrumers Type I to IV shows that quadrumer Type II possess the darkest bottom disk while the gaps in this quadrumer is the minimum. It also can be used as a proof of subgroup decomposition recipe of quadrumers explained in section 4.3.

5.3 Influence of defects on the near-field energy

Thus far, near-field energy properties in symmetric oligomers have been considered. In this section, the effect of geometrical defects via symmetry breaking of pentamers on near-field energy localization is studied. With an applied offset to the position of central nanodisk, an unique capability appears which allows us to localize the near-field energy selectively [60]. Figure 5.5 shows the calculated near-field energy intensity distribution in the asymmetric pentamer studied in section 3.7. These plots are calculated at the normal incidence of a single light source at a wavelength of 800 nm for various polarizations. Figure 5.5 (a) shows that when the structure is illuminated by the x-polarized light, energy localization can be achieved in the 3 nm gap between the central disk E and disk C, while the interaction between the central disk C and disk A experiences the minimum amount of the stored energy at this wavelength. Figure 5.5 (b) shows the effect of the y-polarized light on the localization of the energy. In this case, all the energy is stored at the gaps among the central disks E and disks B and D. An interesting feature appears when the light polarization is changed to 45 degree with respect to the x-axis in the X-Y plane. As can be seen in Fig. 5.5(c), the near-field energy is unequally distributed among three gaps of the central disk E and disks B, C and D. While the two gaps among the central disk E and disks B and D, store equal near-field energy, the gap between central disk E and disk C exhibits a higher amount of localized energy. These selective energy localizations show the advantages of this

asymmetric pentamers as compared to the symmetric pentamers [47], in which the near-field energy can be tuned either along x- or y-direction. It is worth reminding that the tuning of spatial near-field localization in the asymmetric pentamers is also established without the requirement of co-illumination by two light sources [87] or the adjustment of the phase delay between them [196].

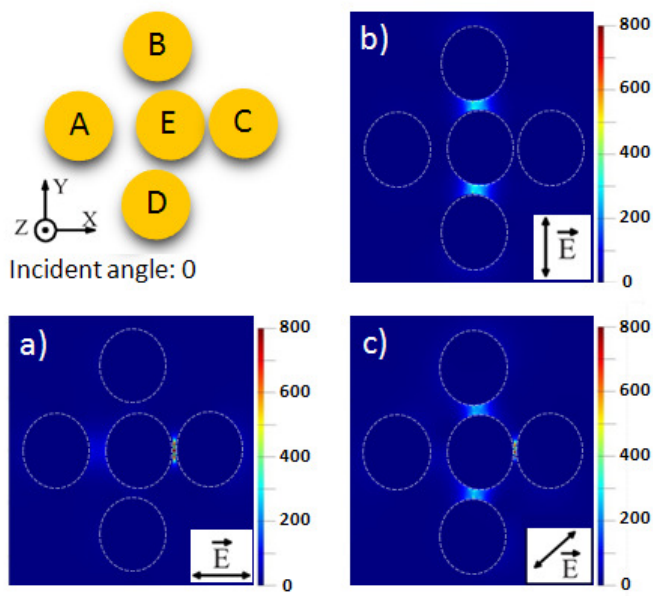

Figure 5. 5 Calculated near-field energy distribution within the Type III pentamer at x-polarized normal incidence and a wavelength of 800 nm: (a) x- polarization, (b) y-polarization and (c) 45-degree polarization, with respect to x axis.

5.4. Near-field energy enhancement by rotor-shaped structures

In Chapters 3 and 4, hybrid oligomers consisting of circular satellite elements and rotor-shaped central elements were introduced [62]. Isotropic far-field optical properties of such structures were studied in details. In this section, near-field optical properties of these hybrid oligomers are investigated. It is shown that these oligomers enhance the exhibited near-field energy among the gaps significantly. Meanwhile, these structures allow achieving

more precise localization of the near-field energy. It should be noted that all comparisons in this section are established with the same gap but different central elements of pentamers.

Starting with pentamers, Fig. 5.6 shows a comparison among regular pentamers [4-6] consisting of circular similar disk versus hybrid pentamers consisting of rotor-shaped central element and circular satellite surrounding elements. In section 3.6, it was shown that the rotor-shaped structure as a monolith structure, just exhibit a SPR at 1010 nm. Calculated field intensity shown in Fig. 5.6 (a) is at this wavelength. As can be seen the field enhancement is only around 100 times and the field localization is relatively poor [62].

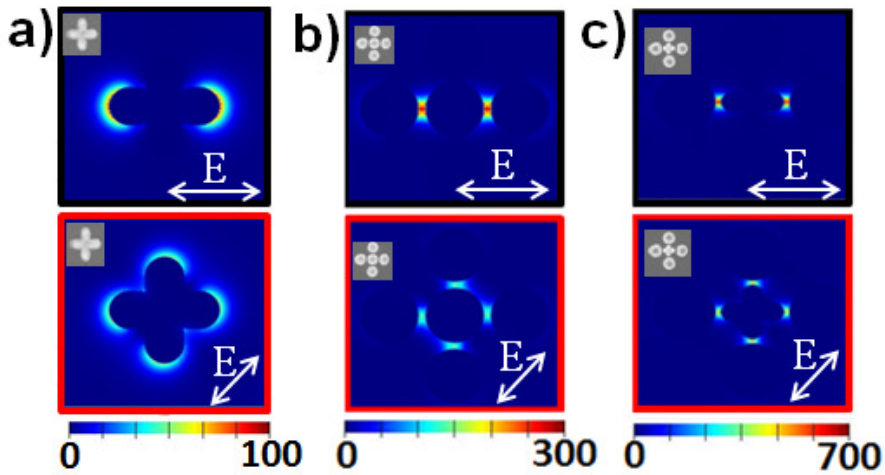

Figure 5.6 Calculated field distribution at indicated polarization excitation for (a) rotor shaped structure, (b) regular pentamer and (c) hybrid pentamer at a wavelength of 1010 nm and structure II at a wavelength of 1025 nm.

But the replacement of the central element of regular pentamers with such rotor-shaped structures is found to enhance field intensity and its localization capabilities. For this purpose, the near-field energy of regular pentamers consisting of all circular disks and hybrid pentamers consisting of a replaced rotor-shaped central disks are compared. The inter-particle gaps among the elements of all structures are kept at 20nm. Meanwhile, the near-field energy for each structure is calculated at the wavelength of second extinction peak

which is 890 nm for regular pentamer and 877 nm for hybrid pentamer. More than two times enhancement in near-field intensity and much more localizations inside the same gaps can be seen clearly in the combined oligomers as compared to either rotor-shaped nanostructures or regular oligomers.

The same trend can be seen in quadrumers. Figure 5.7 shows a comparison among regular quadrumers consisting of similar disks with identical diameters versus hybrid pentamers consisting of rotor-shaped central element and circular satellite surrounding elements. Far-field optical properties of these structures are studied in section 4.3. It was shown that 120^0 rotor-shaped structure exhibit a SPR at 1025 nm. Calculated field intensity shown in Fig. 5.7 (a) is at this wavelength. Again weak field enhancement and localization are obvious in this plot. The near-field energy for regular quadrumer at 880 nm and hybrid quadrumer at 866 nm, shown in Figs 5.7 (b) and (c), respectively, reveal more than two times enhancement in near-field intensity once the central element of regular quadrumer replaced with rotor-shaped structure. It should be noted that the gaps sizes are the same. Better localization inside the same gaps in the hybrid quadrumer as compared to regular quadrumers is another advantage.

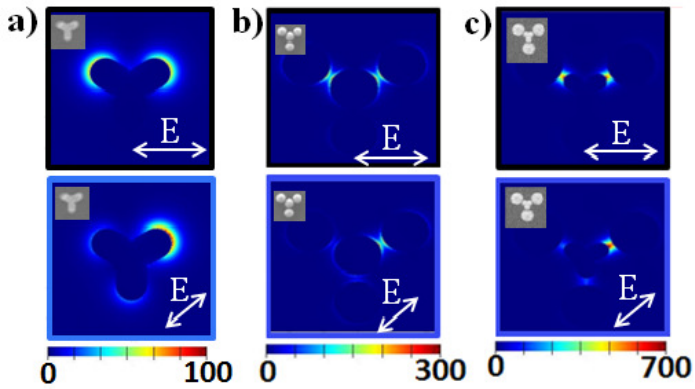

Figure 5.7 Calculated field distribution at indicated polarization excitation for (a) rotor shaped structure, (b) regular pentamer and (c) hybrid pentamer at a wavelength of 1010 nm and structure II at a wavelength of 1025 nm.

Such hybrid oligomers can find wide potential applications in plasmonic systems because of their isotropic optical properties in parallel to the tunability of the field localization at the same time. Use of such structures in oligomers is one of these applications which attribute to considerable enhancement in field intensity and strong localizations [62].

5.5. Summary

Near-field optical properties of planar symmetric coupled oligomers such as pentamers and quadrumers, were studied in this chapter. It was shown that such oligomers support higher sensitivity optical response than uncoupled plasmonic systems. It was shown that while the far-field spectral responses of oligomers are polarization-independent, due to the structure symmetry, the near-field energy in nanogaps can be polarization-controlled. This localization is established at a normal incident light of a single source rather than co-illumination by two light sources accompanied by different incident angles or phase shift.

It was shown that in symmetric pentamers, near-field energy can be localized among either horizontal or vertical elements based on the polarization direction. In quadrumers, one more capability was investigated to turn one of the hot-spots entirely off. Influence of the nanodisk sizes and gaps among them as well as geometrical defects on the intensity and shape of the hot spots in pentamers and quadrumers are also studied. Finally, a new type of hybrid quadrumers and pentamers were introduced to show the enhancement in near-field energy at the same gap just via geometrical manipulations. All these potentials can overcome the spatial restrictions of conventional optics

Chapter 6.

Conclusions and future Work

6.1. Conclusions

In this thesis, far-field and near-field optical properties of novel oligomers such as pentamers and quadrumers were studied in detail. These configurations of nanodisks with sufficiently small inter-particle separation were designed and fabricated with high precisions. It was shown that the strong coupling among components of oligomers led to exhibition of higher sensitivities and consequently a novel set of optical properties.

Detailed study of far-field optical properties of pentamers and quadrumers revealed high propensity to exhibit sharp FR independent of polarization of excitation and without resorting to excitation of challenging high-order modes. Meanwhile, it was shown that manipulation in the number of satellite elements in such structures led to the modulation in the ratio of anti-parallel dipole modes and FR consequently. It is a result of changing the ratio between the opposing phase oscillating plasmons from 1/8 and 1/6 in nonamers and heptamers to 2/3 and 1/3 in the designed pentamers and quadrumers, respectively. The effect of element size and gaps on far-field optical properties was also studied in different types of pentamers and quadrumers. It was shown that the gaps among the elements play more important role than the elements size. Meanwhile, it was investigated that oligomers possess capability to exhibit multi FRs, as well. It has been shown that breaking the symmetry in oligomers, may lead to emergence of an additional FR while the first FR exists. It was proved through a presence of a new pattern of anti-parallel dipole modes in a short wavelentgh window.

Furthermore, it was shown that far-field spectra of pentamers and quadrumers can be associated to different degrees of interference strength of eigen-modes of two subgroups of

components. Based on this observation, the spectral response was designed by changing the particle shape of either subgroup separately or simultaneously. This flexible method to control the resonance lineshape was obtained without invoking a change of particle size, inter-particle distance and the number of elements of the oligomers.

On the other hand, detailed study on the near-field optical properties of oligomers revealed that the reduction in the components quantities provides more promising applications not only in far-field responses but also in near-field responses. It was investigated that pentamers and quadrumers have the capability to enhance localized near-field energies known as hot-spots in nanoscale gaps just among the central element and surrounding satellite elements. Polarization direction was used as a versatile tool to localize these hot spots. Meanwhile, it was shown that by geometrical manipulation in hybrid oligomers, one can enhance field intensity and localization of such hot spots while the gap is kept constant. The influence of geometrical defects on these structures was also considered.

6.2. Future works

Future studies on this research can be extended to the points listed below:

1. Realization of actual applications of oligomers is a high promising research direction which can be considered. Existence of FR in far-field optical properties of oligomers provides high potentials for bio-chemical sensing and slow light application. Meanwhile, unique near-field energy distributions of oligomers can be used in optical switching, non-linear spectroscopy and nanolithography.

2. Near-field optical properties, such as large electric field enhancement at the gap regions, were only shown in simulation. Measurement and imaging of the electric field

distributions experimentally is a critical issue in such subdiffraction scales. It is another interesting research pathway for oligomers.

3. Fabricated oligomers in this research work were established by electron beam lithography which is a serial writing method with low speed and high cost. Mass production of such structures in a big area with other methods would benefit actual applications.

4. In terms of analogy to molecular configurations, co-planar oligomers are not good candidates. It is due to non-co-planar geometry of most of molecules in the universe. 3D oligomers can be used to fill this gap.

5. Flexible substrate can be used to fabricate oligomers. Therefore, the metamaterials with different shapes can be investigated, such as pyramid, cone, and sphere. These metamaterials proposed can be used for cloaking and superlense generation, which are of both scientific interest and potential applications.

References and links

1. B. Luk'yanchuk, N. I. Zheludev, S. A. Maier, N. J. Halas, P. Nordlander, H. Giessen, and C. T. Chong, "The Fano resonance in plasmonic nanostructures and metamaterials," Nature Materials **9**, 707-715 (2010).
2. M. Rahmani, B. Luk'yanchuk, and M. Hong, "Fano resonance in novel plasmonic nanostructures," Laser & Photonics Reviews, DOI: 10.1002/lpor.201200021 (2012).
3. U. Fano, "Effects of configuration interaction on intensities and phase shifts," Physical Review **124**, 1866-1878 (1961).
4. A. E. Miroshnichenko, S. Flach, and Y. S. Kivshar, "Fano resonances in nanoscale structures," Reviews of Modern Physics **82**, 2257-2298 (2010).
5. V. Giannini, A. I. Fernández-Domínguez, S. C. Heck, and S. A. Maier, "Plasmonic nanoantennas: Fundamentals and their use in controlling the radiative properties of nanoemitters," Chemical Reviews **111**, 3888-3912 (2011).
6. N. J. Halas, S. Lal, W. S. Chang, S. Link, and P. Nordlander, "Plasmons in strongly coupled metallic nanostructures," Chemical Reviews **111**, 3913-3961 (2011).
7. M. R. Jones, K. D. Osberg, R. J. MacFarlane, M. R. Langille, and C. A. Mirkin, "Templated techniques for the synthesis and assembly of plasmonic nanostructures," Chemical Reviews **111**, 3736-3827 (2011).
8. M. I. Rabinovitch, and D. I. Trubetskov, *Oscillations and Waves in Linear and Nonlinear Systems* (Kluwer Academic Publishers, 1989).
9. A. C. Johnson, C. M. Marcus, M. P. Hanson, and A. C. Gossard, "Coulomb-modified Fano resonance in a one-lead quantum dot," Physical Review B **71**, 115333 (2005)
10. R. Franco, M. S. Figueira, and E. V. Anda, "Fano resonance in electronic transport through a quantum wire with a side-coupled quantum dot: X-boson treatment," Physical Review B **67**, 1553011 (2003).
11. K. Kobayashi, H. Aikawa, A. Sano, S. Katsumoto, and Y. Iye, "Fano resonance in a quantum wire with a side-coupled quantum dot," Physical Review B **70**, 035319 (2004).
12. Y. Alhassid, Y. V. Fyodorov, T. Gorin, W. Ihra, and B. Mehlig, "Fano interference and cross-section fluctuations in molecular photodissociation," Physical Review A - Atomic, Molecular, and Optical Physics **73**, 042711 (2006).
13. T. H. Hoffmann, M. Allan, K. Franz, M. W. Ruf, H. Hotop, G. Sauter, and W. Meyer, "Resonance structure in electron-N2 scattering around 11.5 eV: High-resolution measurements, ab initio calculations and line shape analyses," Journal of Physics B: Atomic, Molecular and Optical Physics **42**, 211001(2009).
14. S. Mukhopadhyay, R. Biswas, and C. Sinha, "Tunable Fano resonances in the ballistic transmission and tunneling lifetime in a biased bilayer graphene nanostructure," Physics Letters, Section A: General, Atomic and Solid State Physics **375**, 2921-2927 (2011).
15. S. Mukhopadhyay, R. Biswas, and C. Sinha, "Signature of quantum interference and the Fano resonances in the transmission spectrum of bilayer graphene nanostructure," Journal of Applied Physics **110**, 014306 (2011).

16. H. G. Luo, T. Xiang, X. Q. Wang, Z. B. Su, and L. Yu, "Fano resonance for Anderson impurity systems," Physical Review Letters **92**, 256602 (2004).
17. M. V. Rybin, A. B. Khanikaev, M. Inoue, A. K. Samusev, M. J. Steel, G. Yushin, and M. F. Limonov, "Bragg scattering induces Fano resonance in photonic crystals," Photonics and Nanostructures - Fundamentals and Applications **8**, 86-93 (2010).
18. M. V. Rybin, A. B. Khanikaev, M. Inoue, K. B. Samusev, M. J. Steel, G. Yushin, and M. F. Limonov, "Fano Resonance between Mie and Bragg Scattering in Photonic Crystals," Physical Review Letters **103**, 023901 (2009).
19. D. Y. Lei, K. Appavoo, Y. Sonnefraud, R. F. Haglund Jr, and S. A. Maier, "Single-particle plasmon resonance spectroscopy of phase transition in vanadium dioxide," Optics Letters **35**, 3988-3990 (2010).
20. D. Y. Lei, A. Aubry, S. A. Maier, and J. B. Pendry, "Broadband nano-focusing of light using kissing nanowires," New Journal of Physics **12**, 093030 (2010).
21. S. Maier, *Plasmonics: fundamentals and applications* (Springer, Berlin, 2007).
22. M. I. Stockman, "Nanoplasmonics: Past, present, and glimpse into future," Optics Express **19**, 22029-22106 (2011).
23. A. I. Fernández-Domínguez, and S. A. Maier, "New design principles for nanoplasmonics," IEEE Photonics Journal **3**, 284-287 (2011).
24. S. A. Maier, "Nanoplasmonic cavities and waveguides: From design principles to active modulation and gain," Proceedings of the Photonics Society Summer Topical Meeting Series, 2010 IEEE, London, UK, 66-67 (2010).
25. W. Zhang, B. Gallinet, and O. J. F. Martin, "Symmetry and selection rules for localized surface plasmon resonances in nanostructures," Physical Review B - Condensed Matter and Materials Physics **81**, 235427 (2010).
26. E. Petryayeva, and U. J. Krull, "Localized surface plasmon resonance: Nanostructures, bioassays and biosensing-A review," Analytica Chimica Acta **706**, 8-24 (2011).
27. F. Papoff, and B. Hourahine, "The geometrical nature of optical resonances in nanoparticles," arXiv:1102.4958v1, 4 (2011).
28. T. Utikal, T. Zentgraf, T. Paul, C. Rockstuhl, F. Lederer, M. Lippitz, and H. Giessen, "Towards the origin of the nonlinear response in hybrid plasmonic systems," Physical Review Letters **106**, 133901(2011).
29. P. Biagioni, J. S. Huang, and B. Hecht, "Nanoantennas for visible and infrared radiation," Reports On Progress In Physics **75,** 40 (2012).
30. D. Y. Lei, A. I. Fernández-Domínguez, Y. Sonnefraud, K. Appavoo, R. F. Haglund Jr, J. B. Pendry, and S. Maier, "Revealing Plasmonic Gap Modes in Particle-on-Film Systems Using Dark-Field Spectroscopy," ACS Nano **6**, 1380–1386 (2012).
31. M. Agio, "Optical antennas as nanoscale resonators," Nanoscale **4**, 692-706 (2012).
32. R. Singh, I. A. I. Al-Naib, M. Koch, and W. Zhang, "Sharp Fano resonances in THz metamaterials," Optics Express **19**, 6312-6319 (2011).

33. A. P. Sukhorukov, D. O. Ignatyeva, and A. N. Kalish, "Terahertz and infrared surface wave beams and pulses on gyrotropic, nonlinear and metamaterial interfaces," Journal of Infrared, Millimeter, and Terahertz Waves **32**, 1223-1235 (2011).
34. Z. Li, Y. Ma, R. Huang, R. Singh, J. Gu, Z. Tian, J. Han, and W. Zhang, "Manipulating the plasmon-induced transparency in terahertz metamaterials," Optics Express **19**, 8912-8919 (2011).
35. I. A. I. Al-Naib, C. Jansen, N. Born, and M. Koch, "Polarization and angle independent terahertz metamaterials with high Q-factors," Applied Physics Letters **98**, 091107 (2011).
36. R. Singh, I. A. I. Al-Naib, Y. Yang, D. Roy Chowdhury, W. Cao, C. Rockstuhl, T. Ozaki, R. Morandotti, and W. Zhang, "Observing metamaterial induced transparency in individual Fano resonators with broken symmetry," Applied Physics Letters **99**, 201107 (2011).
37. X. Xiao, J. Wu, F. Miyamaru, M. Zhang, S. Li, M. W. Takeda, W. Wen, and P. Sheng, "Fano effect of metamaterial resonance in terahertz extraordinary transmission," Applied Physics Letters **98**, 011911 (2011).
38. A. Tuniz, R. Lwin, A. Argyros, S. C. Fleming, E. M. Pogson, E. Constable, R. A. Lewis, and B. T. Kuhlmey, "Stacked-and-drawn metamaterials with magnetic resonances in the terahertz range," Optics Express **19**, 16480-16490 (2011).
39. B. Pradarutti, G. Torosyan, M. Theuer, and R. Beigang, "Fano profiles in transmission spectra of terahertz radiation through one-dimensional periodic metallic structures," Applied Physics Letters **97**, 244103 (2010).
40. C. Jansen, I. A. I. Al-Naib, N. Born, and M. Koch, "Terahertz metasurfaces with high Q-factors," Applied Physics Letters **98**, 051109 (2011).
41. Y. Ma, Z. Li, Y. Yang, R. Huang, R. Singh, S. Zhang, J. Gu, Z. Tian, J. Han, and W. Zhang, "Plasmon-induced transparency in twisted Fano terahertz metamaterials," Optical Materials Express **1**, 391-399 (2011).
42. A. E. Nikolaenko, N. Papasimakis, A. Chipouline, F. DeAngelis, E. DiFabrizio, and N. I. Zheludev, "THz bandwidth optical switching with carbon nanotube metamaterial," Optics Express **20**, 6068-6079 (2012).
43. Z. Chen, R. Mohsen, G. Yandong, C. T. Chong, and M. H. Hong, "Realization of Variable Three-Dimensional Terahertz Metamaterial Tubes for Passive Resonance Tunability," Advanced Materials **24**, OP143-OP147 (2012).
44. Z. C. Chen, M. H. Hong, C. S. Lim, N. R. Han, L. P. Shi, and T. C. Chong, "Parallel laser microfabrication of large-area asymmetric split ring resonator metamaterials and its structural tuning for terahertz resonance," Applied Physics Letters **96**, 3224793 (2010).
45. J. B. Lassiter, H. Sobhani, J. A. Fan, J. Kundu, F. Capasso, P. Nordlander, and N. J. Halas, "Fano resonances in plasmonic nanoclusters: Geometrical and chemical tunability," Nano Letters **10**, 3184-3189 (2010).

46. M. Hentschel, M. Saliba, R. Vogelgesang, H. Giessen, A. P. Alivisatos, and N. Liu, "Transition from Isolated to Collective Modes in Plasmonic Oligomers," Nano Letters **10**, 2721-2726 (2010).
47. M. Rahmani, B. Lukiyanchuk, B. Ng, A. K. G. Tavakkoli, Y. F. Liew, and M. H. Hong, "Generation of pronounced Fano Resonances and tuning of subwavelength spatial light distribution in plasmonic pentamers," Optics Express **19**, 4949-4956 (2011).
48. M. Rahmani, T. Tahmasebi, Y. Lin, B. Lukiyanchuk, T. Y. F. Liew, and M. H. Hong, "Influence of plasmon destructive interferences on optical properties of gold planar quadrumers," Nanotechnology **22,** 245204 (2011).
49. M. Hentschel, D. Dregely, R. Vogelgesang, H. Giessen, and N. Liu, "Plasmonic oligomers: The role of individual particles in collective behavior," ACS Nano **5**, 2042-2050 (2011).
50. D. Dregely, M. Hentschel, and H. Giessen, "Excitation and tuning of higher-order fano resonances in plasmonic oligomer clusters," ACS Nano **5**, 8202-8211 (2011).
51. J. A. Fan, K. Bao, C. Wu, J. Bao, R. Bardhan, N. J. Halas, V. N. Manoharan, G. Shvets, P. Nordlander, and F. Capasso, "Fano-like interference in self-assembled plasmonic quadrumer clusters," Nano Letters **10**, 4680-4685 (2010).
52. K. Bao, N. A. Mirin, and P. Nordlander, "Fano resonances in planar silver nanosphere clusters," Applied Physics A **100**, 333-339 (2010).
53. J. A. Fan, Y. He, K. Bao, C. Wu, J. Bao, N. B. Schade, V. N. Manoharan, G. Shvets, P. Nordlander, D. R. Liu, and F. Capasso, "DNA-enabled self-assembly of plasmonic nanoclusters," Nano Letters **11**, 4859-4864 (2011).
54. J. A. Fan, C. Wu, K. Bao, J. Bao, R. Bardhan, N. J. Halas, V. N. Manoharan, P. Nordlander, G. Shvets, and F. Capasso, "Self-assembled plasmonic nanoparticle clusters," Science **328**, 1135-1138 (2010).
55. S. N. Sheikholeslami, A. García-Etxarri, and J. A. Dionne, "Controlling the interplay of electric and magnetic modes via Fano-like plasmon resonances," Nano Letters **11**, 3927-3934 (2011).
56. P. Alonso-Gonzalez, M. Schnell, P. Sarriugarte, H. Sobhani, C. Wu, N. Arju, A. Khanikaev, F. Golmar, P. Albella, L. Arzubiaga, F. Casanova, L. E. Hueso, P. Nordlander, G. Shvets, and R. Hillenbrand, "Real-space mapping of Fano interference in plasmonic metamolecules," Nano Letters **11**, 3922-3926 (2011).
57. M. Hentschel, N. Liu, D. Dregely, and H. Giessen, "Plasmonic oligomers: The role of individual particles in collective behavior," ACS Nano **5**, 2042–2050 (2011)
58. T. C. M. Frimmer, and A. F. Koenderink, "Signature of a Fano-resonance in a plasmonic meta-molecule's local density of optical states," arXiv:1109.5407v1 (2011).
59. B. Yan, S. V. Boriskina, and B. M. Reinhard, "Optimizing Gold Nanoparticle Cluster Configurations (n ≤ 7) for array applications," Journal of Physical Chemistry C **115**, 4578-4583 (2011).
60. M. Rahmani, B. Lukiyanchuk, T. T. V. Nguyen, T. Tahmasebi, Y. Lin, T. Y. F. Liew, and M. H. Hong, "Influence of symmetry breaking in pentamers on Fano resonance and near-field energy localization," Optical Materials Express **1**, 1409-1415 (2011).

61. M. Rahmani, B. Lukiyanchuk, T. Tahmasebi, Y. Lin, T. Y. F. Liew, and M. H. Hong, "Polarization-controlled spatial localization of near-field energy in planar symmetric coupled oligomers," Applied Physics A **107**, 23-30 (2011).
62. M. Rahmani, B. Lukiyanhuk, T.Y. F. Liew, and M. H. Hong,"Planar Isotropic Rotor-Shaped Nanostructures: an Alternative to Develop Oligomers," Proceedings of Laser Science to Photonic Application (CLEO), San Jose, USA, 2012, QTh4F.2 (2012).
63. J. Yang, M. Rahmani, J. H. Teng, and M. H. Hong, "Magnetic-electric interference in metal-dielectric-metal oligomers: generation of magneto-electric Fano resonance," Opt. Mater. Express **2**, 1407-1415 (2012).
64. N. A. Mirin, K. Bao, and P. Nordlander, "Fano Resonances in plasmonic nanoparticle aggregates," Journal of Physical Chemistry A **113**, 4028-4034 (2009).
65. Y. Cui, J. Zhou, V. A. Tamma, and W. Park, "Dynamic Tuning and Symmetry Lowering of Fano Resonance in Plasmonic Nanostructure," ACS Nano **6**, 2385–2393 (2012).
66. M. Rahmani, D. Y. Lei, V. Giannini, B. Lukiyanchuk, M. Ranjbar, T. Y. F. Liew, M. H. Hong, and S. A. Maier, "Subgroup Decomposition of Plasmonic Resonances in Hybrid Oligomers: Modeling the Resonance Lineshape," Nano Letters **12**, 2101–2106 (2012).
67. D. M. Riffe, "Classical Fano oscillator," Physical Review B **84**, 064308 (2011).
68. S. Mukherjee, H. Sobhani, J. B. Lassiter, R. Bardhan, P. Nordlander, and N. J. Halas, "Fanoshells: Nanoparticles with built-in Fano resonances," Nano Letters **10**, 2694-2701 (2010).
69. Y. S. Joe, A. M. Satanin, and C. S. Kim, "Classical analogy of Fano resonances," Physica Scripta **74**, 259-266 (2006).
70. H. T. Lee, and A. W. Poon, "Fano resonances in prism-coupled square micropillars," Optics Letters **29**, 5-7 (2004).
71. H. Duan, H. Hu, K. Kumar, Z. Shen, and J. K. W. Yang, "Direct and reliable patterning of plasmonic nanostructures with sub-10-nm gaps," ACS Nano **5**, 7593-7600 (2011).
72. A. K. G. Tavakkoli, S. N. Piramanayagam, M. Ranjbar, R. Sbiaa, and T. C. Chong, "Path to achieve sub-10-nm half-pitch using electron beam lithography," Journal of Vacuum Science and Technology B: Microelectronics and Nanometer Structures **29**, 0110351-0110357 (2011).
73. A. E. Miroshnichenko, S. Flach, A. V. Gorbach, B. S. Luk'yanchuk, Y. S. Kivshar, and M. I. Tribelsky, "Fano resonances: A Discovery that was not made 100 years ago," Optics and Photonics News **19**, 48 (2008).
74. S. C. Yang, H. Kobori, C. L. He, M. H. Lin, C. Hung-Ying, C. Li, M. Kanehara, T. Teranishi, and S. Gwo, "Plasmon hybridization in individual gold nanocrystal dimers: Direct observation of bright and dark modes," Nano Letters **10**, 632-637 (2010).
75. J. Ye, N. Verellen, W. Van Roy, L. Lagae, G. Maes, G. Borghs, and P. Van Dorpe, "Plasmonic modes of metallic semishells in a polymer film," ACS Nano **4**, 1457-1464 (2010).

76. R. Ortuño, C. García-Meca, F. J. Rodríguez-Fortuño, J. Martí, and A. Martínez, "Multiple extraordinary optical transmission peaks from evanescent coupling in perforated metal plates surrounded by dielectrics," Optics Express **18**, 7893-7898 (2010).
77. R. Ortuño, C. García-Meca, F. J. Rodríguez-Fortuño, and A. Martínez, "Enlarging the negative-index bandwidth of optical metamaterials by hybridized plasmon resonances," Optics Letters 35, 4205-4207 (2010).
78. J. I. Ziegler, and R. F. Haglund Jr, "Plasmonic response of nanoscale spirals," Nano Letters 10, 3013-3018 (2010).
79. J. I. Ziegler, J. Nag, and R. F. Haglund, Jr, "Plasmonic response of nanoscale spirals," Proceedings of Plasmonics: Metallic Nanostructures and Their Optical Properties VII, San Diego, USA, 7394 (2009).
80. B. Kang, E. Choi, H. H. Lee, E. S. Kim, J. H. Woo, J. Kim, T. Y. Hong, J. H. Kim, and J. W. Wu, "Polarization angle control of coherent coupling in metamaterial superlattice for closed mode excitation," Optics Express 18, 11552-11561 (2010).
81. M. Geiselmann, T. Utikal, M. Lippitz, and H. Giessen, "Tailoring the ultrafast dynamics of the magnetic mode in magnetic photonic crystals," Physical Review B - Condensed Matter and Materials Physics **81**, 235101 (2010).
82. S. Campione, A. Vallecchi, M. Albani, F. Mesa, and F. Capolino, "Closed form formulas and tunability of resonances in pairs of gold-dielectric nanoshells," Proceedings of the SPIE Villa Conference on Metamaterials, LasVegas, USA, 775738 (2011).
83. A. Vallecchi, S. Campione, and F. Capolino, "Symmetric and antisymmetric resonances in a pair of metal-dielectric nanoshells: Tunability and closed-form formulas," Journal of Nanophotonics **4**, 041577 (2010).
84. F. Neubrech, A. Garcia-Etxarri, D. Weber, J. Bochterle, H. Shen, M. Lamy De La Chapelle, G. W. Bryant, J. Aizpurua, and A. Pucci, "Defect-induced activation of symmetry forbidden infrared resonances in individual metallic nanorods," Applied Physics Letters **96**, 157403 (2010).
85. D. Weber, P. Albella, P. Alonso-González, F. Neubrech, H. Gui, T. Nagao, R. Hillenbrand, J. Aizpurua, and A. Pucci, "Longitudinal and transverse coupling in infrared gold nanoantenna arrays: Long range versus short range interaction regimes," Optics Express **19**, 15047-15061 (2011).
86. D. E. Gómez, K. C. Vernon, and T. J. Davis, "Symmetry effects on the optical coupling between plasmonic nanoparticles with applications to hierarchical structures," Physical Review B - Condensed Matter and Materials Physics **81**, 233401 (2010).
87. X. R. Su, Z. S. Zhang, L. H. Zhang, Q. Q. Li, C. C. Chen, Z. J. Yang, and Q. Q. Wang, "Plasmonic interferences and optical modulations in dark-bright-dark plasmon resonators," Applied Physics Letters **96**, 043113 (2010).
88. J. Ye, P. V. Dorpe, W. V. Roy, K. Lodewijks, I. D. Vlaminck, G. Borghs, and G. Maes, "Fabrication and optical properties of gold semishells," Journal of Physical Chemistry C **113**, 3110-3115 (2009).

89. A. Bitzer, J. Wallauer, H. Helm, H. Merbold, T. Feurer, and M. Walther, "Lattice modes mediate radiative coupling in metamaterial arrays," Optics Express **17**, 22108-22113 (2009).
90. F. Hao, P. Nordlander, Y. Sonnefraud, P. Van Dorpe, and S. A. Maier, "Tunability of subradiant dipolar and fano-type plasmon resonances in metallic ring/disk cavities: Implications for nanoscale optical sensing," ACS Nano **3**, 643-652 (2009).
91. F. Hao, Y. Sonnefraud, P. Van Dorpe, S. A. Maier, N. J. Halas, and P. Nordlander, "Symmetry breaking in plasmonic nanocavities: Subradiant LSPR sensing and a tunable Fano resonance," Nano Letters **8**, 3983-3988 (2008).
92. S. A. Maier, "Plasmonics: The benefits of darkness," Nature Materials **8**, 699-700 (2009).
93. N. Verellen, Y. Sonnefraud, H. Sobhani, F. Hao, V. V. Moshehalkov, P. Van Dorpe, P. Nordlander, and S. A. Maier, "Fano resonances in individual coherent plasmonic nanocavities," Nano Letters **9**, 1663-1667 (2009).
94. R. L. Chern, and W. T. Hong, "Transmission resonances and antiresonances in metallic arrays of compound subwavelength holes," Journal of Optics **12**, 065101 (2010).
95. Z. G. Dong, H. Liu, M. X. Xu, T. Li, S. M. Wang, J. X. Cao, S. N. Zhu, and X. Zhang, "Role of asymmetric environment on the dark mode excitation in metamaterial analogue of electromagnetically-induced transparency," Optics Express **18**, 22412-22417 (2010).
96. K. Aydin, I. M. Pryce, and H. A. Atwater, "Symmetry breaking and strong coupling in planar optical metamaterials," Optics Express **18**, 13407-13417 (2010).
97. A. Yar, A. Donarini, S. Koller, and M. Grifoni, "Dynamical symmetry breaking in vibration-assisted transport through nanostructures," Physical Review B **84,** 115432 (2011).
98. J. Shi, C. Guan, and Z. Wang, "Ultra-narrow resonances and near-field energy density enhancement in planar cross-linked metamaterials," Photonics and Nanostructures - Fundamentals and Applications **9**, 255-260 (2011).
99. X. Fan, Z. Shen, and B. Luk'yanchuk, "Huge light scattering from active anisotropic spherical particles," Optics Express **18**, 24868-24880 (2010).
100. J. Shi, C. Guan, and Z. Wang, "Highly resonant positive and negative metamaterials," Phot. Nano. Fund. Appl. 9, 255–260 (2010).
101. S. Iyer, S. Popov, and A. T. Friberg, "Effective tunability and realistic estimates of group index in plasmonic metamaterials exhibiting electromagnetically induced transparency," Applied Optics **50**, 3958-3961 (2011).
102. E. Plum, K. Tanaka, W. T. Chen, V. A. Fedotov, D. P. Tsai, and N. I. Zheludev, "A combinatorial approach to metamaterials discovery," Journal of Optics **13** , 055102 (2011).
103. M. Kang, H. X. Cui, Y. Li, B. Gu, J. Chen, and H. T. Wang, "Fano-Feshbach resonance in structural symmetry broken metamaterials," Journal of Applied Physics **109** (2011).

104. J. Ye, L. Lagae, G. Maes, G. Borghs, and P. Van Dorpe, "Symmetry breaking induced optical properties of gold open shell nanostructures," Optics Express **17**, 23765-23771 (2009).
105. P. J. Schuck, Z. Zhang, A. Weber-Bargioni, Sh. Wu, S. Dhuey, and S. Cabrini, "Manipulating nano-scale light fields with the asymmetric bowtie nano-Colorsorter," Proceedings of the Quantum Electronics and Laser Science Conference (QELS), San Jose, USA, QFAS (2010).
106. Z. Zhang, A. Weber-Bargioni, S. W. Wu, S. Dhuey, S. Cabrini, and P. J. Schuck, "Manipulating nanoscale light fields with the asymmetric bowtie nano-colorsorter," Nano Letters **9**, 4505-4509 (2009).
107. T. G. Habteyes, S. Dhuey, S. Cabrini, P. J. Schuck, and S. R. Leone, "Theta-shaped plasmonic nanostructures: Bringing "dark" multipole plasmon resonances into action via conductive coupling," Nano Letters **11**, 1819-1825 (2011).
108. A. Artar, A. A. Yanik, and H. Altug, "Directional double Fano resonances in plasmonic hetero-oligomers," Nano Letters 11, 1685–1689 (2011).
109. L. V. Brown, H. Sobhani, J. B. Lassiter, P. Nordlander, and N. J. Halas, "Heterodimers: Plasmonic properties of mismatched nanoparticle pairs," ACS Nano **4**, 819-832 (2010).
110. A. Christ, O. J. F. Martin, Y. Ekinci, N. A. Gippius, and S. G. Tikhodeev, "Symmetry breaking in a plasmonic metamaterial at optical wavelength," Nano Letters **8**, 2171-2175 (2008).
111. Z. Fang, J. Cai, Z. Yan, P. Nordlander, N. J. Halas, and X. Zhu, "Removing a wedge from a metallic nanodisk reveals a fano resonance," Nano Letters **11**, 4475-4479 (2011).
112. Z. Fang, J. Cai, Z. Yan, N. K. Grady, and X. Zhu, "Fano Resonances of Plasmonic Nanodisk," arXiv:1105.1568v1 (2011).
113. L. J. Sherry, S. H. Chang, G. C. Schatz, R. P. Van Duyne, B. J. Wiley, and Y. Xia, "Localized surface plasmon resonance spectroscopy of single silver nanocubes," Nano Letters **5**, 2034-2038 (2005).
114. S. Zhang, K. Bao, N. J. Halas, H. Xu, and P. Nordlander, "Substrate-induced Fano resonances of a plasmonic nanocube: A route to increased-sensitivity localized surface plasmon resonance sensors revealed," Nano Letters **11**, 1657-1663 (2011).
115. H. Lu, X. Liu, D. Mao, Y. Gong, and G. Wang, "Induced transparency in nanoscale plasmonic resonator systems," Optics Letters **36**, 3233-3235 (2011).
116. H. Husu, J. Mäkitalo, R. Siikanen, G. Genty, H. Pietarinen, J. Lehtolahti, J. Laukkanen, M. Kuittinen, and M. Kauranen, "Spectral control in anisotropic resonance-domain metamaterials," Optics Letters **36**, 2375-2377 (2011).
117. A. Santillán, and S. I. Bozhevolnyi, "Acoustic transparency and slow sound using detuned acoustic resonators," Physical Review B **84** ,064304 (2011).
118. T. Utikal, T. Zentgraf, S. G. Tikhodeev, M. Lippitz, and H. Giessen, "Tailoring the photonic band splitting in metallodielectric photonic crystal superlattices," Physical Review B **84**, 133901(2011).

119. C. Wu, A. B. Khanikaev, and G. Shvets, "Broadband slow light metamaterial based on a double-continuum Fano resonance," Physical Review Letters **106**, 107403 (2011).
120. T. J. Davis, M. Hentschel, N. Liu, and H. Giesse, "Analytical model of the three-dimensional plasmonic ruler", ACS Nano **6**, 1291-1295 (2012).
121. Y. Sun, H. Jiang, Y. Yang, Y. Zhang, H. Chen, and S. Zhu, "Electromagnetically induced transparency in metamaterials: Influence of intrinsic loss and dynamic evolution," Physical Review B **83**, 195140 (2011).
122. E. Ye, K. Y. Win, H. R. Tan, M. Lin, C. P. Teng, A. Mlayah, and M. Y. Han, "Plasmonic gold nanocrosses with multidirectional excitation and strong photothermal effect," Journal of the American Chemical Society **133**, 8506-8509 (2011).
123. Y. Chu, D. Wang, W. Zhu, and K. B. Crozier, "Double resonance surface enhanced Raman scattering substrates: An intuitive coupled oscillator model," Optics Express **19**, 14919-14928 (2011).
124. S. V. Boriskina, and B. M. Reinhard, "Adaptive on-chip control of nano-optical fields with optoplasmonic vortex nanogates," Optics Express **19**, 22305-22315 (2011).
125. W. T. Chen, C. J. Chen, P. C. Wu, S. Sun, L. Zhou, G. Y. Guo, C. T. Hsiao, K. Y. Yang, N. I. Zheludev, and D. P. Tsai, "Optical magnetic response in three-dimensional metamaterial of upright plasmonic meta-molecules," Optics Express **19**, 12837-12842 (2011).
126. J. M. Reed, H. Wang, W. Hu, and S. Zou, "Shape of Fano resonance line spectra calculated for silver nanorods," Optics Letters **36**, 4386-4388 (2011).
127. L. Langguth, and H. Giessen, "Coupling strength of complex plasmonic structures in the multiple dipole approximation," Optics Express **19**, 22156-22166 (2011).
128. J. Chen, P. Wang, C. Chen, Y. Lu, H. Ming, and Q. Zhan, "Plasmonic EIT-like switching in bright-dark-bright plasmon resonators," Optics Express **19**, 5970-5978 (2011).
129. M. Abb, P. Albella, J. Aizpurua, and O. L. Muskens, "All-Optical control of a single plasmonic nanoantenna┌ITO hybrid" ACS, Nano **11**, 2457–2463 (2011).
130. M. G. Nielsen, A. Pors, O. Albrektsen, M. Willatzen, and S. I. Bozhevolnyi, "Experimental determination of the refractive index of metamaterials," Journal of Optics **13** ,055106 (2011).
131. N. Verellen, P. Van Dorpe, D. Vercruysse, G. A. E. Vandenbosch, and V. V. Moshchalkov, "Dark and bright localized surface plasmons in nanocrosses," Optics Express **19**, 11034-11051 (2011).
132. W. J. Chen, J. C. W. Lee, J. W. Dong, C. W. Qiu, and H. Z. Wang, "Fano resonance of three-dimensional spiral photonic crystals: Paradoxical transmission and polarization gap," Applied Physics Letters **98** ,08116 (2011).
133. Y. He, H. Zhou, Y. Jin, and S. He, "Plasmon induced transparency in a dielectric waveguide," Applied Physics Letters **99**, 043113 (2011).
134. B. Tang, L. Dai, and C. Jiang, "Electromagnetically induced transparency in hybrid plasmonic-dielectric system," Optics Express **19**, 628-637 (2011).

135. S. Peng, C. Qiu, Z. He, Y. Ye, S. Xu, K. Tang, M. Ke, and Z. Liu, Journal of Applied Physics **110** , 014509 (2011).
136. J. Shi, Zh. Zhu, Ch. Guan, Y. Li, and Z. Wang, "Extraordinary acoustic shielding by a monolayer of periodical polymethyl methacrylate cylinders immersed in water," Proceedings of Advances in Optoelectronics and Micro/Nano- Optics (AOM), Harbin, China, 1–3 (2010).
137. J. Shi, C. Guan, and Z. Wang, "Local field energy density enhancement in planar metamaterials," Photonic and Nanostructures: Fundamental and Applications **9**, 255–260 (2011).
138. Y. W. Huang, W. T. Chen, P. C. Wu, Y. F. Chau, N. I. Zheludev, and D. P. Tsai, "Toroidal and magnetic spectral responses of four split-ring resonators," Optics Express 20, 1760–1761 (2012).
139. Y. Liu, H. Jiang, C. Xue, W. Tan, H. Chen, and Y. Shi, "Fano resonances in a bilayer structure composed of two kinds of dispersive meta-materials," Progress in Electromagnetics Research Letters **26**, 49-57 (2011).
140. W. Chen, G. Y. Chen, and Y. N. Chen, "Controlling fano resonance of nanowire surface plasmons," Optics Letters **36**, 3602-3604 (2011).
141. X. G. Yin, C. P. Huang, Q. J. Wang, W. X. Huang, L. Zhou, C. Zhang, and Y. Y. Zhu, "Fanolike resonance due to plasmon excitation in linear chains of metal bumps," Optics Express **19**, 10485-10493 (2011).
142. Y. Lu, X. Jin, S. Lee, J. Y. Rhee, W. H. Jang, and Y. P. Lee, "Passive and active control of a plasmonic mimic of electromagnetically induced transparency in stereometamaterials and planar metamaterials," Advances In Natural Sciences: Nanoscience and Nanotechnology **1**, 045004 (2010).
143. A. Ridolfo, R. Saija, S. Savasta, P. H. Jones, M. A. Iatì, and O. M. Maragò, "Fano-doppler laser cooling of hybrid nanostructures," ACS Nano **5**, 7354-7361 (2011).
144. D. Nardi, M. Travagliati, M. E. Siemens, Q. Li, M. M. Murnane, H. C. Kapteyn, G. Ferrini, F. Parmigiani, and F. Banfi, "Probing thermomechanics at the nanoscale: Impulsively excited pseudosurface acoustic waves in hypersonic phononic crystals," Nano Letters **11**, 4126-4133 (2011).
145. P. Offermans, M. C. Schaafsma, S. R. K. Rodriguez, Y. Zhang, M. Crego-Calama, S. H. Brongersma, and J. Gómez Rivas, "Universal scaling of the figure of merit of plasmonic sensors," ACS Nano **5**, 5151-5157 (2011).
146. B. Fazio, C. D'Andrea, F. Bonaccorso, A. Irrera, G. Calogero, C. Vasi, P. G. Gucciardi, M. Allegrini, A. Toma, D. Chiappe, C. Martella, and F. Buatier De Mongeot, "Re-radiation enhancement in polarized surface-enhanced resonant raman scattering of randomly oriented molecules on self-organized gold nanowires," ACS Nano **5**, 5945-5956 (2011).
147. H. Chen, L. Shao, T. Ming, K. C. Woo, Y. C. Man, J. Wang, and H. Q. Lin, "Observation of the Fano resonance in Gold Nanorods supported on high-dielectric-constant substrates," ACS Nano **5**, 6754-6763 (2011).

148. W. Ahn, S. V. Boriskina, Y. Hong, and B. M. Reinhard, "Electromagnetic Field Enhancement and Spectrum Shaping through Plasmonically Integrated Optical Vortices," ACS Nano **6**, 951-960 (2012).
149. P. Spinelli, V. E. Ferry, J. V. D. Groep, M. V. Lare, M. A. Verschuuren, R. E. I. Schropp, H. A. Atwater, and A. Polman, "Plasmonic light trapping in thin-film Si solar cells," Journal of Optics **14**, 11 (2012).
150. S. Toroghi, and P. G. Kik, "Cascaded plasmonic metamaterials for phase-controlled enhancement of nonlinear absorption and refraction," Physical Review B **85**, 045432 (2012).
151. Y. W. Huang, Y. T. Chen, P. C. Wu, V. Fedotov, V. Savinov, Y. Z. Ho, Y. F. Chau, N. I. Zheludev, D. P. Tsai, and "Design of plasmonic toroidal metamaterials at optical frequencies," Optics Express **20**, 9 (2012).
152. C. T. Li, H. F. Chen, L. W. Un, H. C. Lee, T. J. Yen, and "Study of optical phase transduction on localized surface plasmon resonance for ultrasensitive detection," Optics Express **20**, 3250-3260 (2012).
153. L. Zhu, F. Y. Meng, J. H. Fu, Q. Wu, J. Hua, and "Multi-band slow light metamaterial," Optics Express **20**, 4494-4502 (2012).
154. S. H. Mousavi, A. B. Khanikaev, and S. G., "Optical properties of Fano-resonant metallic metasurfaces on a substrate," arXiv:1201.3146v1 (2012).
155. L. Niu, J. B. Zhang, Y. H. Fu, S. Kulkarni, and B. Lukyánchuk, "Fano resonance in dual-disk ring plasmonic nanostructures," Optics Express **19**, 22974-22981 (2011).
156. M. R. Disfani, M. S. Abrishamian, and P. Berini, "Teardrop-shaped surface-plasmon resonators," Optics Express **20**, 6472-6477 (2012).
157. V. I. Belotelov, A. N. Kalish, A. K. Zvezdin, A. V. Gopal, and A. S. Vengurlekar, "Fabry-Perot plasmonic structures for nanophotonics," Journal of the Optical Society of America B: Optical Physics **29**, 294-299 (2012).
158. W.-S. Chang, J.B. Lassiter, P. Swanglap, H. Sobhani, S. Khatua, P. Nordlander, N.J. Halas, and S. Link, "A Plasmonic Fano switch," Nano Letters **12**, 4977- 4982 (2012).
159. Y. Xu, and A. E. Miroshnichenko, "Nonlinear Mach-Zehnder-Fano interferometer," Europhysics Letters **97**, 44007 (2012).
160. F. López-Tejeira, R. Paniagua-Domínguez, R. Rodríguez-Oliveros, and J. A. Sánchez-Gil, "Fano-like interference of plasmon resonances at a single rod-shaped nanoantenna," New Journal of Physics **14**, 23035-23050(2012).
161. C. S. Lim, M. H. Hong, Z. C. Chen, N. R. Han, B. Luk'yanchuk, and T. C. Chong, "Hybrid metamaterial design and fabrication for terahertz resonance response enhancement," Optics Express 18, 12421-12429 (2010).
162. Y. H. Fu, J. B. Zhang, Y. F. Yu, and B. Luk‘yanchuk," Generating and manipulating higher order Fano resonances in dual-disk ring plasmonic nanostructures," ACS Nano **6**, 2130–2137 (2012).
163. Y. H. Fu, A. Q. Liu, W. M. Zhu, X. M. Zhang, D. P. Tsai, J. B. Zhang, T. Mei, J. F. Tao, H. C. Guo, X. H. Zhang, J. H. Teng, N. I. Zheludev, G. Q. Lo, and D. L. Kwong, "A

micromachined reconfigurable metamaterial via reconfiguration of asymmetric split-ring resonators," Advanced Functional Materials **21**, 3589-3594 (2011).

164. Y. Sonnefraud, N. Verellen, H. Sobhani, G. A. E. Vandenbosch, V. V. Moshchalkov, P. Van Dorpe, P. Nordlander, and S. A. Maier, "Experimental realization of subradiant, superradiant, and fano resonances in ring/disk plasmonic nanocavities," ACS Nano **4**, 1664-1670 (2010).
165. N. Papasimakis, Y. H. Fu, V. A. Fedotov, S. L. Prosvirnin, D. P. Tsai, and N. I. Zheludev, "Metamaterial with polarization and direction insensitive resonant transmission response mimicking electromagnetically induced transparency," Applied Physics Letters **94**, 211902 (2009).
166. N. Papasimakis, V. A. Fedotov, Y. H. Fu, D. P. Tsai, and N. I. Zheludev, "Coherent and incoherent metamaterials and order-disorder transitions," Physical Review B **80**, 014509 (2009).
167. N. Verellen, P. Van Dorpe, C. Huang, K. Lodewijks, G. A. E. Vandenbosch, L. Lagae, and V. V. Moshchalkov, "Plasmon line shaping using nanocrosses for high sensitivity localized surface plasmon resonance sensing," Nano Letters **11**, 391-397 (2011).
168. L. Lin, and A. Roberts, "Light transmission through nanostructured metallic films: Coupling between surface waves and localized resonances," Optics Express **19**, 2626-2633 (2011).
169. H. Liu, N. Wang, Y. Liu, Y. Zhao, and X. Wu, "Light transmission properties of double-overlapped annular apertures," Optics Letters **36**, 385-387 (2011).
170. G. X. Li, Z. L. Wang, S. M. Chen, and K. W. Cheah, "Narrowband plasmonic excitation on gold hole-array nanostructures observed using spectroscopic ellipsometer," Optics Express **19**, 6348-6353 (2011).
171. P. Lovera, D. Jones, and A. O'Riordan, "Elliptical nanohole array in thin gold film as micrometer sized optical filter set for fluorescent-labelled assays," Journal of Physics: Conference Series **307**, 012206 (2011).
172. J. Zhang, J. Y. Ou, N. Papasimakis, Y. Chen, K. F. MacDonald, and N. Zheludev, "Controlling the Colour of Metals: Intaglio and Bas-Relief Metamaterials," Optics Express 19, 623279–23285 (2011).
173. A. Artar, A. A. Yanik, and H. Altug, "Multispectral plasmon induced transparency in coupled meta-atoms," Nano Letters **11**, 1685-1689 (2011).
174. M. Liu, Y. Song, Y. Zhang, X. Wang, and C. Jin, "Mode Evolution and Transmission Suppression in a Perforated Ultrathin Metallic Film with a Triangular Array of Holes," Plasmonics DOI: 10.1007/s11468-011-9321-5 (2012).
175. D. Wu, S. Jiang, and X. Liu, "Tunable Fano resonances in three-layered bimetallic Au and Ag nanoshell," Journal of Physical Chemistry C **115**, 23797-23801 (2011).
176. M. Wang, M. Cao, X. Chen, and N. Gu, "Subradiant plasmon modes in multilayer metal-dielectric nanoshells," Journal of Physical Chemistry C **115**, 20920-20925 (2011).

177. N. T. Fofang, N. K. Grady, Z. Fan, A. O. Govorov, and N. J. Halas, "Plexciton dynamics: Exciton-plasmon coupling in a J-aggregate-Au nanoshell complex provides a mechanism for nonlinearity," Nano Letters **11**, 1556-1560 (2011).
178. S. Mühlig, A. Cunningham, S. Scheeler, C. Pacholski, T. Bürgi, C. Rockstuhl, and F. Lederer, "Self-assembled plasmonic core-shell clusters with an isotropic magnetic dipole response in the visible range," ACS Nano **5**, 6586-6592 (2011).
179. S. Mühlig, C. Rockstuhl, V. Yannopapas, T. Bürgi, N. Shalkevich, and F. Lederer, "Optical properties of a fabricated self-assembled bottom-up bulk metamaterial," Optics Express **19**, 9607-9616 (2011).
180. A. I. Kuznetsov, A. B. Evlyukhin, M. R. Goṇalves, C. Reinhardt, A. Koroleva, M. L. Arnedillo, R. Kiyan, O. Marti, and B. N. Chichkov, "Laser fabrication of large-scale nanoparticle arrays for sensing applications," ACS Nano **5**, 4843-4849 (2011).
181. J. F. Ho, B. Luk'yanchuk, and J. B. Zhang, "Tunable Fano resonances in silver-silica-silver multilayer nanoshells," Applied Physics A **107**, 133-137 (2012).
182. H. Wang, Y. Wu, B. Lassiter, C. L. Nehl, J. H. Hafner, P. Nordlander, and M. J. Halas, "Symmetry breaking in individual plasmonic nanoparticles," Proceedings of the National Academy of Sciences of the United States of America **103**, 10856-10860 (2006).
183. S. Aksu, M. Huang, A. Artar, A. A. Yanik, S. Selvarasah, M. R. Dokmeci, and H. Altug, "Flexible plasmonics on unconventional and nonplanar substrates," Advanced Materials **23**, 4422-4430 (2011).
184. R. A. Farrell, N. Kehagias, M. T. Shaw, V. Reboud, M. Zelsmann, J. D. Holmes, C. M. Sotomayor Torres, and M. A. Morris, "Surface-directed dewetting of a block copolymer for fabricating highly uniform nanostructured microdroplets and concentric nanorings," ACS Nano **5**, 1073-1085 (2011).
185. S. Darwich, K. Mougin, L. Vidal, E. Gnecco, and H. Haidara, "Nanobubble and nanodroplet template growth of particle nanorings versus nanoholes in drying nanofluids and polymer films," Nanoscale **3**, 1211-1217 (2011).
186. N. Vogel, J. Fischer, R. Mohammadi, M. Retsch, H. J. Butt, K. Landfester, C. K. Weiss, and M. Kreiter, "Plasmon hybridization in stacked double crescents arrays fabricated by colloidal lithography," Nano Letters **11**, 446-454 (2011).
187. S. Yang, F. Xu, S. Ostendorp, G. Wilde, H. Zhao, and Y. Lei, "Template-confined dewetting process to surface nanopatterns: Fabrication, structural tunability, and structure-related properties," Advanced Functional Materials **21**, 2446-2455 (2011).
188. S. Yang, J. Xu, Z. Wang, H. Zeng, and Y. Lei, "Janus particle arrays with multiple structural controlling abilities synthesized by seed-directed deposition," Journal of Materials Chemistry **21**, 11930-11935 (2011).
189. J. Xiao, and L. Qi, "Surfactant-assisted, shape-controlled synthesis of gold nanocrystals," Nanoscale **3**, 1383-1396 (2011).

190. H. Yabu, T. Jinno, K. Koike, T. Higuchi, and M. Shimomura, "Three-dimensional assembly of gold nanoparticles in spherically confined microphase-separation structures of block copolymers," Macromolecules **44**, 5868-5873 (2011).
191. Y. Lin, M. H. Hong, T. C. Chong, C. S. Lim, G. X. Chen, L. S. Tan, Z. B. Wang, and L. P. Shi, "Ultrafast-laser-induced parallel phase-change nanolithography," Applied Physics Letters **89**, 041108 (2006).
192. C. S. Lim, M. H. Hong, Y. Lin, Q. Xie, B. S. Luk'yanchuk, A. Senthil Kumar, and M. Rahman, "Microlens array fabrication by laser interference lithography for super-resolution surface nanopatterning," Applied Physics Letters **89**, 191125 (2006).
193. Z. C. Chen, M. H. Hong, H. Dong, Y. D. Gong, C. S. Lim, L. P. Shi, and T. C. Chong, "Parallel laser microfabrication of terahertz metamaterials and its polarization-dependent transmission property," Applied Physics A **101**, 33-36 (2010).
194. M. C. Gwinner, E. Koroknay, F. Liwei, P. Patoka, W. Kandulski, M. Giersig, and H. Giessen, "Periodic large-area metallic split-ring resonator metamaterial fabrication based on shadow nanosphere lithography," Small **5**, 400-406 (2009).
195. J. B. Lassiter, H. Sobhani, M. W. Knight, W. S. Mielczarek, P. Nordlander, and N. J. Halas, "Designing and Deconstructing the Fano Lineshape in Plasmonic Nanoclusters," Nano Letters **12**, 1058-1062 (2011).
196. M. Aeschlimann, M. Bauer, D. Bayer, T. Brixner, F. J. García De Abajo, W. Pfeiffer, M. Rohmer, C. Spindler, and F. Steeb, "Adaptive subwavelength control of nano-optical fields," Nature 446, 301-304 (2007).
197. W. Srituravanich, N. Fang, C. Sun ,Q. Luo, and X. Zhang, " Plasmonic nanolithography, " *Nano Letters* **4**, 1085–1088 (2004).
198. C. A. Pan, and T. P. Ma, "High-quality transparent conductive indium oxide films prepared by thermal evaporation," Applied Physics Letters **37**, 163-165 (1980).
199. D. Finlayson, "Vacuum vapour deposition as a high rate coating process for sheet steel," Vacuum **21**, 35-39 (1971).
200. Y. Q. Fu, N. Kok, and A. Bryan, "Microfabrication of microlens array by focused ion beam technology," Microelectronic Engineering **54**, 211-221 (2000).
201. J. R. Reddan, and N. J. Unakar, "Electron microscopy of cultured mammalian lenses. II. Changes preceding and accompanying insulin induced mitosis," Investigative Ophthalmology **15**, 411-417 (1976).
202. G. Bogdanovic, A. Meurk, and M. W. Rutland, "Tip friction - Torsional spring constant determination," Colloids and Surfaces B: Biointerfaces **19**, 397-405 (2000).
203. P. Martin, "Microspectrophotometers take a closer look," Laser Focus World **47**, 79-85 (2011).
204. P. B. Johnson, and R. W. Christy, "Optical constants of the noble metals," Physical Review B **6**, 4370-4379 (1972).
205. W. L. Barnes, A. Dereux, and T. W. Ebbesen, "Surface plasmon subwavelength optics," Nature **424**, 824-830 (2003).

206. P. K. Jain, X. Huang, I. H. El-Sayed, and M. A. El-Sayed, "Noble metals on the nanoscale: Optical and photothermal properties and some applications in imaging, sensing, biology, and medicine," Accounts of Chemical Research **41**, 1578-1586 (2008).
207. B. S. Luk'yanchuk, M. I. Tribelsky, V. Ternovsky, Z. B. Wang, M. H. Hong, L. P. Shi, and T. C. Chong, "Peculiarities of light scattering by nanoparticles and nanowires near plasmon resonance frequencies in weakly dissipating materials," Journal of Optics A: Pure and Applied Optics **9**, S294-S300 (2007).
208. B. S. Luk'yanchuk, M. I. Tribelsky, Z. B. Wang, Y. Zhou, M. H. Hong, L. P. Shi, and T. C. Chong, "Extraordinary scattering diagram for nanoparticles near plasmon resonance frequencies," Applied Physics A **89**, 259-264 (2007).
209. M. I. Tribelsky, S. Flach, A. E. Miroshnichenko, A. V. Gorbach, and Y. S. Kivshar, "Light scattering by a finite obstacle and fano resonances," Physical Review Letters **100**, 043903 (2008).
210. H. Haken, and H. C. Wolf, *Molecular physics and elements of quantum chemistry* (Springer, Berlin, 2003).
211. H. Wang, D. W. Brandl, P. Nordlander, and N. J. Halas, "Plasmonic nanostructures: Artificial molecules," Accounts of Chemical Research **40**, 53-62 (2007).
212. N. Liu, S. Mukherjee, K. Bao, L. V. Brown, J. Dorfmüller, P. Nordlander, and N. J. Halas, "Magnetic Plasmon Formation and Propagation in Artificial Aromatic Molecules," Nano Letters **12**, 364-369 (2011).
213. V. Klimov, and G. Y. Guo, "Bright and dark plasmon modes in three nanocylinder cluster," Journal of Physical Chemistry C **114**, 22398-22405 (2010).
214. P. Nordlander, C. Oubre, E. Prodan, K. Li, and M. I. Stockman, "Plasmon hybridization in nanoparticle dimers," Nano Letters **4**, 899-903 (2004).
215. G. Margheri, T. Del Rosso, S. Sottini, S. Trigari, and Egiorgetti, "All optical switches based on the coupling of surface plasmon polaritons," Optics Express **16**, 9869-9883 (2008).
216. L. T. Reed M A, *Molecular Nanoelectronics* (American Scientific Publishers, New York, 2003).